General Disclaimer

One or more of the Following Statements may affect this Document

- This document has been reproduced from the best copy furnished by the organizational source. It is being released in the interest of making available as much information as possible.

- This document may contain data, which exceeds the sheet parameters. It was furnished in this condition by the organizational source and is the best copy available.

- This document may contain tone-on-tone or color graphs, charts and/or pictures, which have been reproduced in black and white.

- This document is paginated as submitted by the original source.

- Portions of this document are not fully legible due to the historical nature of some of the material. However, it is the best reproduction available from the original submission.

Produced by the NASA Center for Aerospace Information (CASI)

NSTIF SQT

E85-10061
NASA-CR-174242

THE MINERALOGY OF GLOBAL MAGNETIC ANOMALIES

FINAL TECHNICAL REPORT

(E85-10061 NASA-CR-174242) THE MINERALOGY OF GLOBAL MAGNETIC ANOMALIES Final Technical Report (Massachusetts Univ.) 156 p HC A08/MF A01 CSCL 08G G3/43

N85-16272

Unclas 00061

PROJECT MAGSAT

NATIONAL AERONAUTIC AND SPACE ADMINISTRATION

GODDARD SPACE FLIGHT CENTER

GREENBELT, MARYLAND 20771

CONTRACT NUMBER: NAS5-26414

PRINCIPAL INVESTIGATOR: STEPHEN E. HAGGERTY

DEPARTMENT OF GEOLOGY/GEOGRAPHY

UNIVERSITY OF MASSACHUSETTS

AMHERST, MASSACHUSETTS 01003

JUL 1985
RECEIVED
NASA STI FACILITY
ACQ BRANCH

DECEMBER, 1984

In 1-23-85
M-007

CONTENTS

INTRODUCTION.....1

FINAL REPORT OF RESEARCH RESULTS.....2

OXIDATION PROFILING OF THE CRUST AND MANTLE.....2

SERPENTINITES AS MAGNETIC ANOMALY SOURCES.....9

MAGNETIC SPINELS AND RELATED PHASES FROM MANTLE-DERIVED KIMBERLITES.....20

MAGNETITE AND MAGNETIC SUSCEPTIBILITY RELATIONSHIPS.....21

MAGSAT VECTOR ANOMALIES RELATED TO THE WEST AFRICAN AND AMAZONIAN CRATONS.....33

NATIVE IRON AND THE OXIDATION STATE OF THE CONTINENTAL LOWER CRUST.....34

SUMMARY.....35

REFERENCES.....36

APPENDICES.....38

INTRODUCTION

The objective of this research participation in the MAGSAT program has been to provide experimental and analytical data on magnetic mineralogy as an aid to the interpretation of magnetic anomaly maps.

The approach has been an integrated program, ranging from the chemistry of materials from 100 or more km depth within the Earth, to an examination of the MAGSAT anomaly maps at about 400 km above the Earth's surface. Within this framework we have concentrated on providing a detailed picture of the pertinent mineralogical and magnetic relationships for the region of West Africa, but generalizing the information where justifiable.

Specifically, our effort has been directed toward 1) examining in detail the geochemistry, mineralogy, magnetic properties, and phase relations of magnetic oxides and metal alloys in rocks demonstrated to have originated in the lower crust or upper mantle, 2) examining in general terms the assumption that these rocks, as exposed and collected at the surface, portray the nature of their source regions, and 3) examining in detail the regional geology, tectonics, gravity field and the MAGSAT anomaly maps for West Africa.

The following six-part section outlines the results of the program.

FINAL REPORT OF RESEARCH RESULTS

1) OXIDATION PROFILING OF THE CRUST AND MANTLE

Significance

Iron in some form is commonly believed to be dominantly responsible for magnetization resident in the outer layers of the Earth, but magnetic minerals containing iron are stable only at specific levels of oxidation so that the magnetization of the Earth's lithosphere depends not only on composition, temperature and total pressure but also on the partial pressure of oxygen fugacity (fO_2). Therefore, an understanding of the oxidation state of the lithosphere is crucial to any mineralogical interpretation of the origin of magnetic anomalies measured by MAGSAT.

Results

A graphical approach to the expected ranges of oxidation as a function of temperature and pressure is taken in Fig. 1, where the enstatite + magnesite = olivine + graphite (EMOG) oxygen buffer is based on Eggler and Baker (1982). We have included in our plot the basalt-eclogite transition, the shield and oceanic geotherms, and have also calculated and projected the buffer curves fayalite = magnetite + quartz (FMQ) and wüstite - magnetite (WM) that are more commonly applicable to 1 atm. conditions (i.e. at the surface of the earth). Because all of the curves are relatively steep, the relative changes in oxidation state with depth do not change dramatically along any one buffer. However, the progressive changes that do apply are along the geothermal gradients; a substantial change in oxidation state toward a more oxidized condition of each buffer apparently takes place with increasing depth.

Fig. 2 illustrates the results of an analytical approach to the question of oxidation state at depth, where we have compiled and updated (from Haggerty, 1976) temperature and fO_2 data for basalts; these are shown to have equilibrated along or below FMQ. On comparing these data with the oxidation profiling shown in Fig. 1 we find that if the depth estimates at which basalts are considered to originate (i.e. 20-100 km) are used on Fig. 1, then the levels of oxidation that are preserved in basalts extruded at the surface are comparable to the oxidation levels calculated. This is encouraging because it suggests, for basalts at the least, that the analytical techniques employed in generating the data compiled in Fig. 2 provide reliable probes to the oxidation state

Figure 1. Calculated buffers in pressure-temperature coordinates for the reactions enstatite + magnesite = olivine + graphite (EMOG), wüstite - magnetite (WM) and fayalite = olivine + quartz (FMQ) illustrating the expected ranges of oxidation state for upper mantle conditions. Isobaric oxygen fugacities for each buffer are plotted within the figure in units of -log $\underline{f}O_2$.

ORIGINAL PAGE IS
OF POOR QUALITY

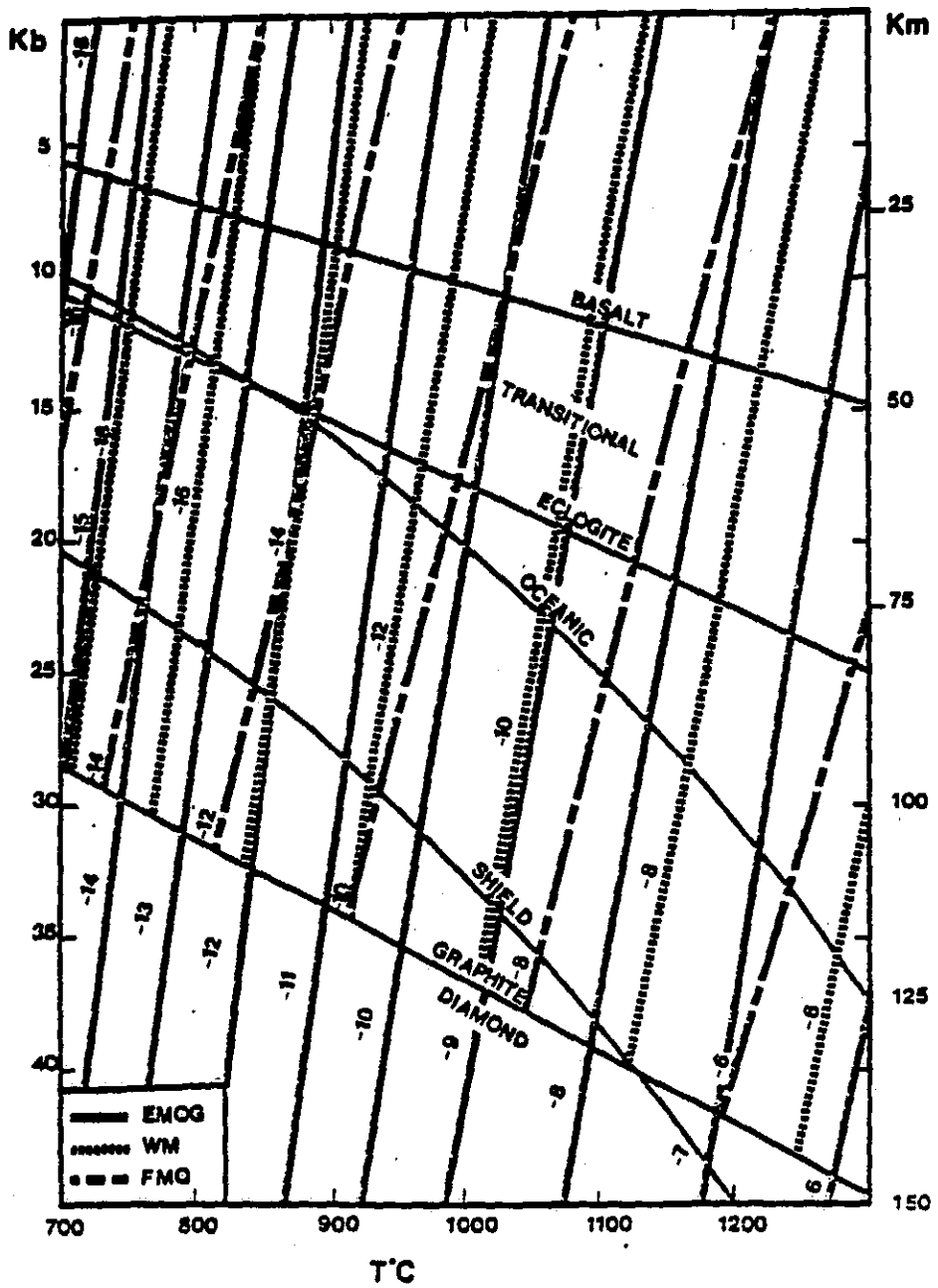

FIG. 1

Figure 2a. Summary of temperature and $\underline{f}O_2$ data for terrestrial oceanic island and ocean floor basalts. Data fall within the hachured envelope; reference buffer curves are fayalite = magnetite + quartz (FMQ) and magnetite - wüstite (MW).

ORIGINAL PAGE IS
OF POOR QUALITY

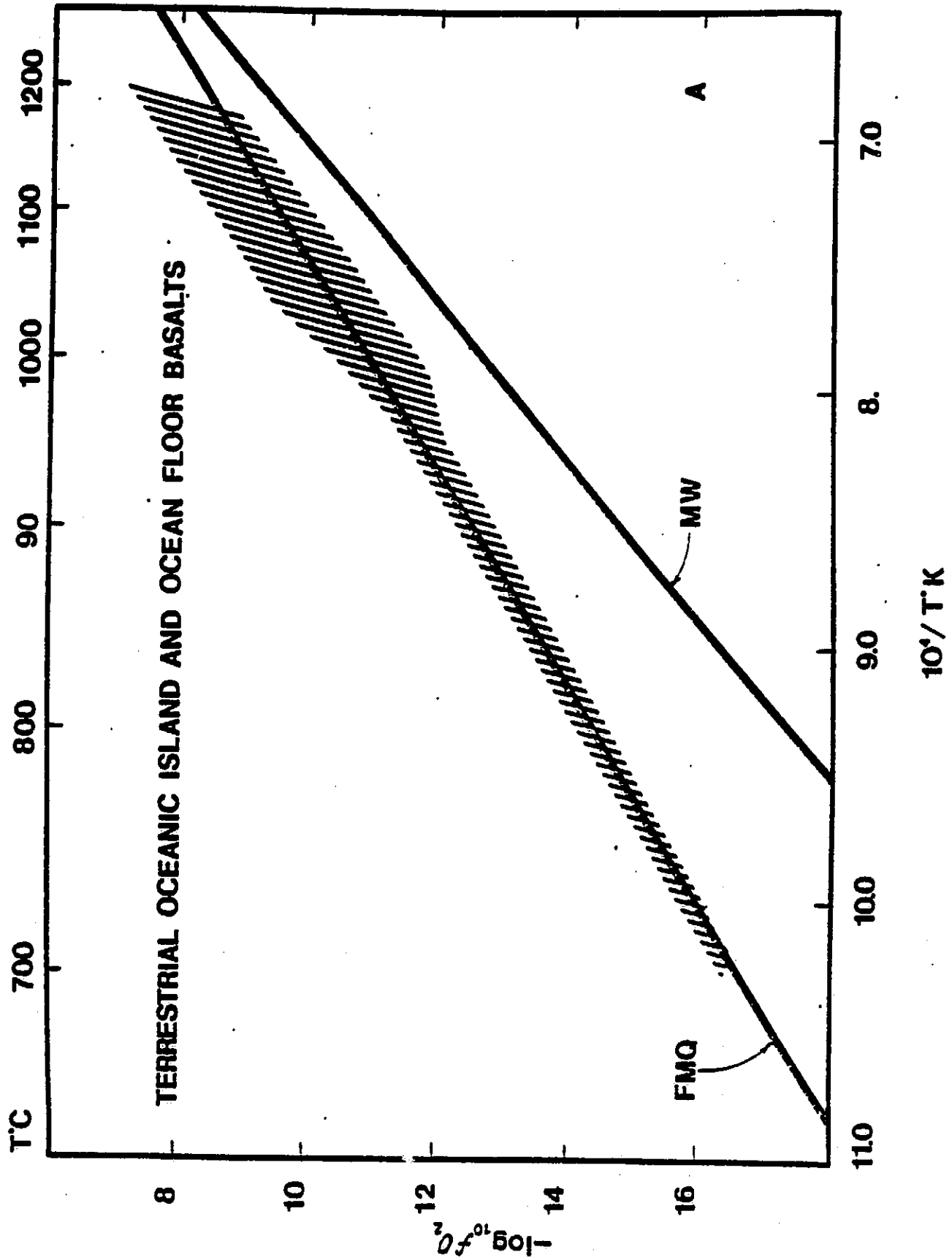

FIG. 2a

Figure 2b. Summary of temperature and fO_2 data for terrestrial continental basalts. Details as in Figure 2a.

ORIGINAL PAGE IS
OF POOR QUALITY

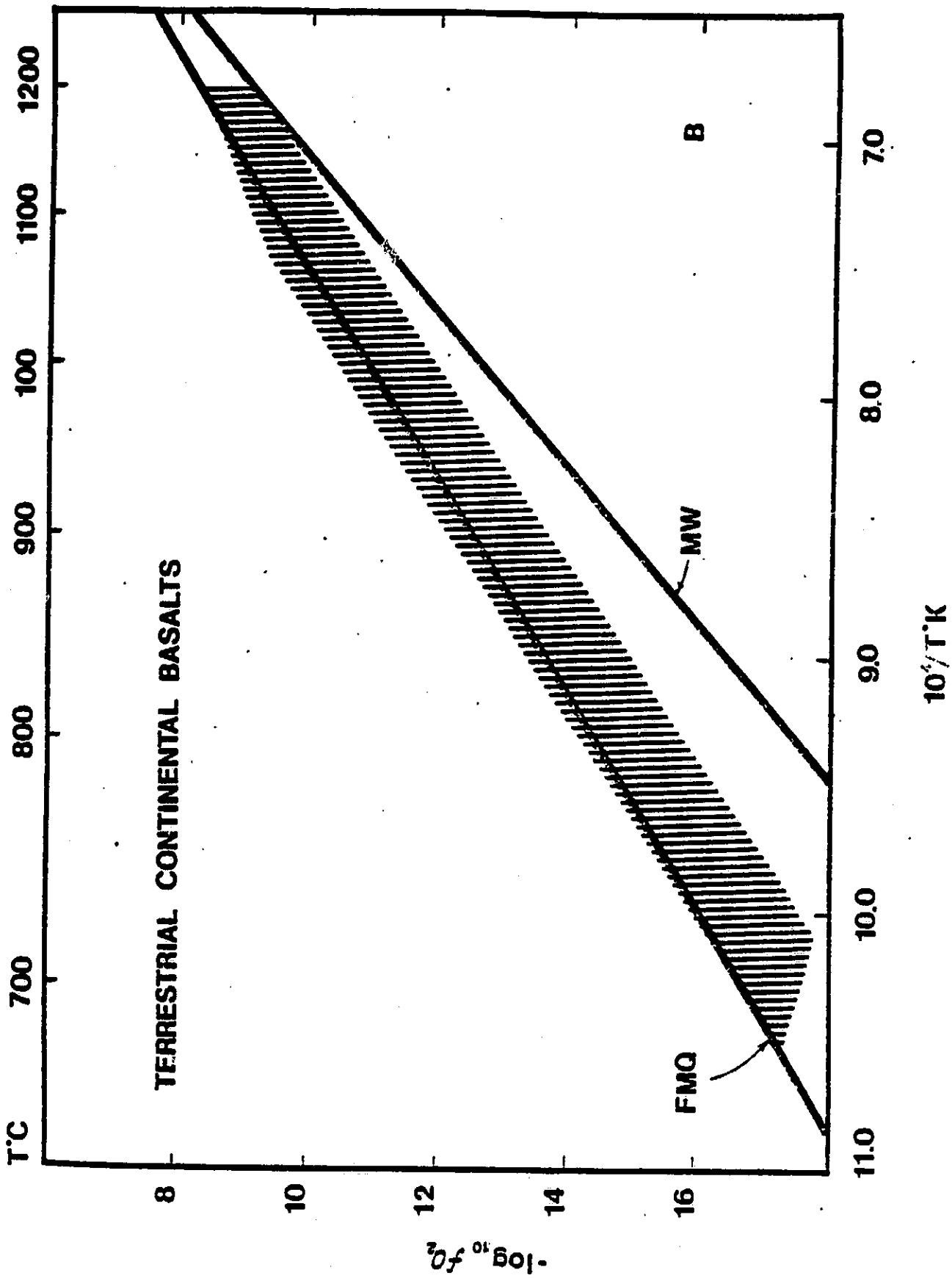

FIG. 2b

of the rocks' source regions.

In further application of the particular technique of evaluating T and $\underline{f}O_2$ by analyzing the exchange equilibria between Fe and Ti and between Fe^{2+} and Fe^{3+} in co-equilibrated ilmenite and spinel, we examined ilmenites from kimberlites in west Africa. We then compared the results to our compilation of T and $\underline{f}O_2$ data on other rocks, derived by the same and other methods. Full details of the analyses and the compilation are given by Haggerty and Tompkins (1983; Appendix 1), and the principle result of this oxidation profiling is shown in Fig. 3.

The result is a series of models presenting prevalent oxygen fugacities and rock types for typical cross-sections through the crust and mantle according to tectonic regime. The Earth appears to be stratified with respect to redox, such that the surface and near-surface are characterized by magnetite - hematite (MH) to FMQ conditions; below this is a geochemically depleted layer within the lithosphere which is of variable thickness and depth but which is at or below wüstite-magnetite (WM), and below this is a geochemically fertile asthenosphere which is relatively oxidized and characterized by FMQ to WM conditions at the shallowest depths, ranging down to wüstite-iron (WI) and to iron at the mantle-core interface.

Summary

We have shown that computed and analytical profiling of the oxidation state of the crust and mantle are compatible, and that these regions of the Earth are stratified in redox potential, the upper crust and the geochemically fertile asthenosphere being relatively oxidized and sandwiching a depleted and reduced lithosphere. The oxidation state models of Fig. 3 now permit meaningful estimates of the potential stability of iron-bearing magnetic minerals in any selected regime of the lithosphere, and therefore constrain mineralogical models of MAGSAT-measured magnetic anomalies.

2) SERPENTINITES AS MAGNETIC ANOMALY SOURCES

Significance

Whereas it is generally accepted that serpentinites are possible contributors to crustal magnetization and that pure magnetite is overwhelmingly responsible for crustal magnetization, the magnetic phase equilibria of serpentinites and the contribution of metal alloys to serpentinites' magnetization and the long-range geophysical signature of serpentinites are poorly

Figure 3. A diagrammatic cross-section through the crust and upper mantle for a variety of tectonic settings, illustrating the distribution of rock types and profiling of oxygen fugacity. The highest oxidizing conditions are represented by the magnetite - hematite (MH) buffer; with increasing reduction the buffer equilibria are NNO (Ni-NiO), FMQ (fayalite - magnetite - quartz), WM (wüstite - magnetite) and IW (iron - wüstite). From Haggerty and Tompkins (1983).

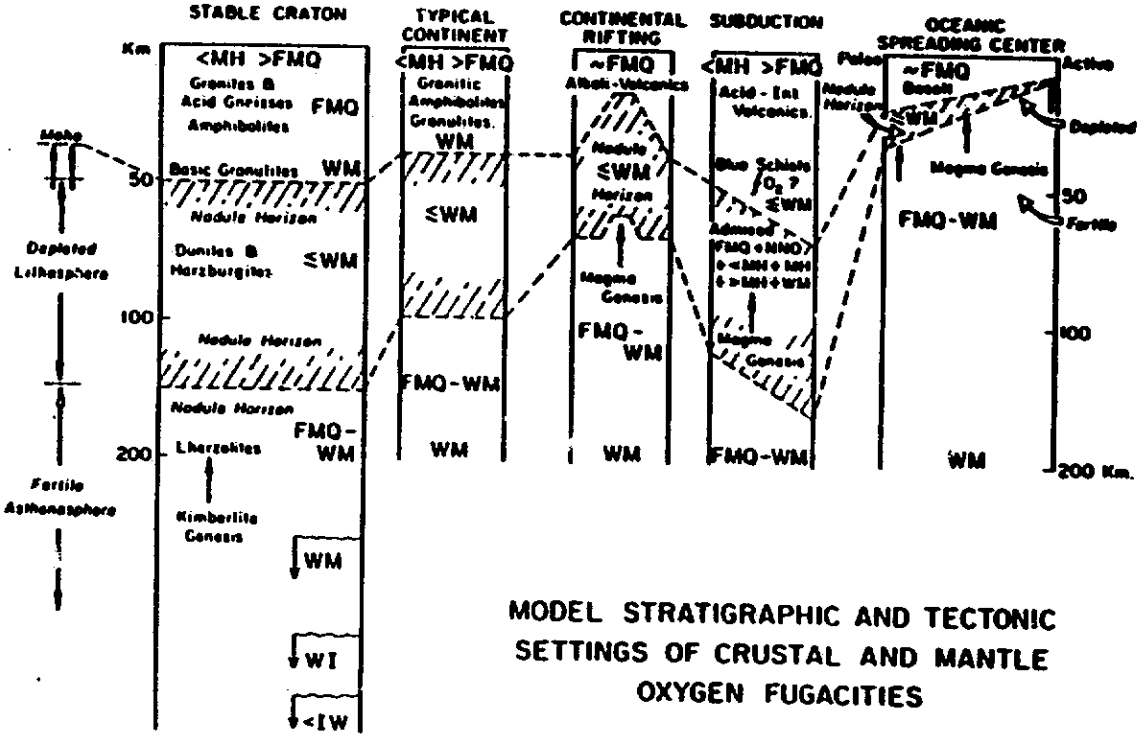

MODEL STRATIGRAPHIC AND TECTONIC SETTINGS OF CRUSTAL AND MANTLE OXYGEN FUGACITIES

FIG. 3

established, to date.

Results

We have undertaken, in a companion study, a set of experiments related to the stability of Fe-Ni metal alloys as a function of temperature and oxidation state. A summary of these data (Fig. 4) illustrates the regimes of magnetite and metal alloy stability and demonstrates that these phases are potential sources of magnetism at depth, subject to geothermal gradient. Moreover, the data are entirely consistent with those illustrated in Figs. 1-3.

We have also conducted a very detailed analytical study of serpentinized peridotites from the Josephine Creek area, Oregon, U.S.A. A catalog of electron microbeam analyses, rock descriptions, densities, and degrees of serpentinization, analytically establishing that Ni_3Fe (awaruite) and CoFe (wairauite) can coexist with magnetic oxides at oxidation levels compatible with serpentinization in the upper mantle, is presented in Progress Report 10/26/1982. Microbeam analyses of metal alloys are summarized in Fig. 5., which illustrates the dominant magnetic alloy compositions and the Curie temperatures to be expected.

The majority of the analysed awaruites from in situ Josephine Creek peridotites have Ni/Fe ratios close to 3:1, indication Curie temperatures of $580^{o}c \pm 5^{o}c$, but the average Co content is about 1.25 wt % and the Curie temperature increases by about $5^{o}c$ per wt % Co; additionally, a small but significant percentage of analyses in the range 60-70 wt % Ni indicate Curie temperatures in excess of $590^{o}c$ even disregarding the affect of Co in awaruite. The analyses of wairauites show Co/Fe ratios generally less than the ideal of 1:1, and mostly indicate Curie temperatures in the range $940-980^{o}c$; Ni contents ranging up to 3 wt % may decrease the Curie temperatures by $20-25^{o}c$.

Because remote magnetic measurements alone are equivocal as regards the source lithology we attempted to constrain more closely the expected geophysical signature of serpentinites by measuring both the magnetic susceptibility and density of the Josephine Creek serpentinites. The result is summarized in Table 1 and Fig. 6.

Fig. 6 shows the results of our analyses in the context of a graphical compilation of data from the literature outlining the relationship between magnetic susceptibility and degree of serpentinization for a variety of ultramafic rocks. From Table 1 and Fig. 6 we draw the following conclusions: 1) Magnetic susceptibility and density of Josephine Creek peridotites increase

Figure 4. Log $\underline{f}O_2$ vs temperature diagram for the Fe-Ni-O system (from MacMahon, 1984). Note especially the T-$\underline{f}O_2$ region in which magnetite (solid solution) plus Fe-Ni alloy co-exist.

ORIGINAL PAGE IS
OF POOR QUALITY

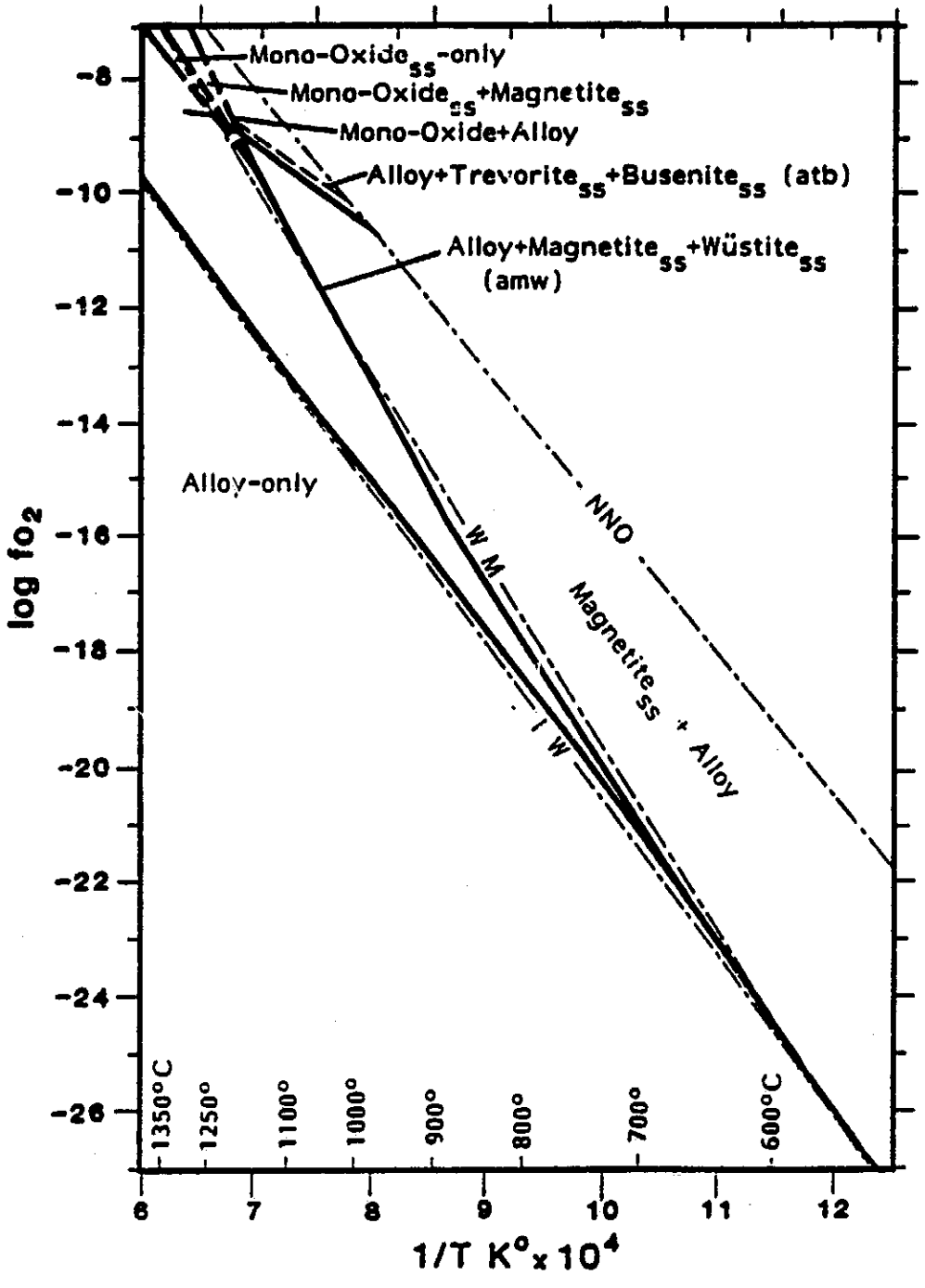

FIG. 4

Figure 5a. Frequency-composition histogram of in situ awaruites from Josephine Creek peridotites. The percentages of analyses are relative to the number of analyses per hand sample. Composition is presented as wt % Ni in Ni-Fe alloy, calculated from the analyses but assuming zero per cent impurities. Co is always present, averaging 1.25 wt % and ranging up to 2.5 wt %, increasing the effective Curie temperatures. S and Cu may also be present but are almost always less than 0.1 and 1.0 wt % respectively.

Figure 5b. Frequency-composition histogram of in situ and nugget wairauites from Josephine Creek peridotites. Calculated similarly to Figure 1a. Ni is present in the range 0.6 to 3.2 wt %, slightly decreasing the Curie temperatures, but other impurities (S and Cu) are less than 1 wt % when combined.

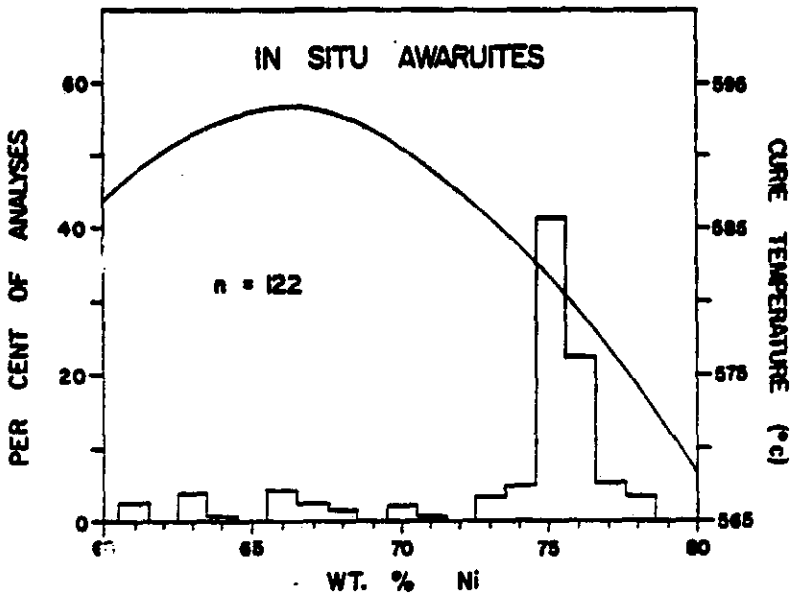
IN SITU AWARUITES
PER CENT OF ANALYSES
CURIE TEMPERATURE (°c)
n = 122
WT. % Ni
60
40
20
0
595
585
575
565
65
70
75
80

FIG. 5a

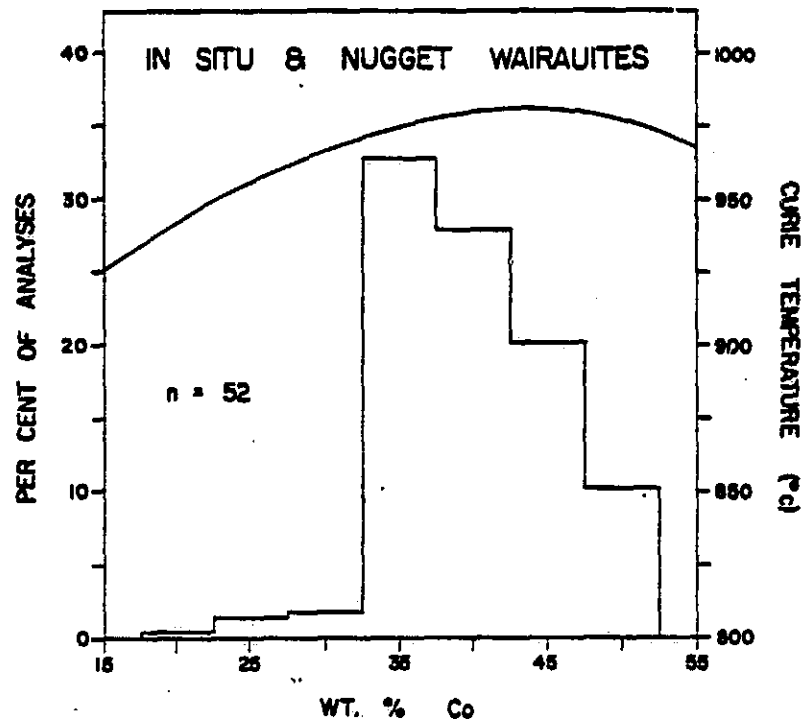
IN SITU & NUGGET WAIRAUITES
PER CENT OF ANALYSES
CURIE TEMPERATURE (°c)
n = 52
WT. % Co
40
30
20
10
0
1000
950
900
850
800
15
25
35
45
55

FIG. 5b

TABLE 1. JOSEPHINE CREEK PERIDOTITES

Sample number	% serpentinized	Density	Apparent volume magnetic susceptibility (cgs)*	Magnetic mineralogy** metal alloy	other
D-26	12	2.90	$1.90\text{-}2.70 \times 10^{-4}$	-	-
B-17	12	3.20	$1.97\text{-}2.94 \times 10^{-5}$	-	-
D-161	21	3.13	$2.63\text{-}3.57 \times 10^{-5}$	-	-
D-221	36	3.01	$1.08\text{-}1.95 \times 10^{-4}$	abundant	-
D-350	36	3.01	$0.55\text{-}1.14 \times 10^{-4}$	present	-
D-223	38	3.00	$1.52\text{-}2.99 \times 10^{-4}$	abundant	chromite
B-52	41	2.97	$2.95\text{-}5.16 \times 10^{-4}$	"	pyrrhotite
D-111	50	2.90	$5.97\text{-}8.62 \times 10^{-5}$	present	chromite
D-145	61	2.81	$0.91\text{-}1.56 \times 10^{-3}$	"	"
D-157	61	2.81	$0.99\text{-}1.85 \times 10^{-4}$	"	-
D-236	72	2.72	$1.81\text{-}3.43 \times 10^{-4}$	"	-
B-16	79	2.67	$1.31\text{-}1.87 \times 10^{-4}$	abundant	-
D-57	87	2.64	$3.80\text{-}6.04 \times 10^{-4}$	present	pyrrhotite
D-181	95	2.85	$0.68\text{-}1.22 \times 10^{-4}$	some	-
D-59	100	2.48	$1.12\text{-}1.79 \times 10^{-3}$	abundant	chromite

*The range of values for a given sample is due primarily to uncertainty in the form of the self-demagnetizing field; samples were measured on a Bison susceptibility bridge; $k_{S.I.} = 4\pi(k_{cgs})$.

**Magnetite is present in all samples

Figure 6. Serpentinization trends in susceptibility-density. Values for the Josephine Creek peridotites are in Table 1. Percentages shown on the figure are the degrees of serpentinization, with good general agreement between the data sets. The theoretical curves calculated by Henkel (1976) for the serpentinization of olivines assumed a 100 % efficiency in converting Fe released from olivine into magnetite. The curve for orthopyroxenes is calculated from molar susceptibility values given by Nagata (1961) and handbook values for densities using the relation $k_{vol;cgs}$ = (density).(molar susceptibility)/(molecular weight). The opx and ol curves effectively outline the allowed region for unserpentinized bimineralic harzburgites. The trends from Henkel (1976) and Lienert and Wasilewski, 1979) place likely upper and lower limits on magnetic susceptibility for a range of serpentinized ultramafics. The curve for Red Mountain peridotite is calculated from mathematical and graphical relationships in Saad (1969). Metal alloys begin to appear in these Josephine Creek peridotites at serpentinization values exceeding 25 %, and are notably present, along with pyrrhotite or chromite, in the samples which depart from the general concave-up trend.

ORIGINAL PAGE IS
OF POOR QUALITY

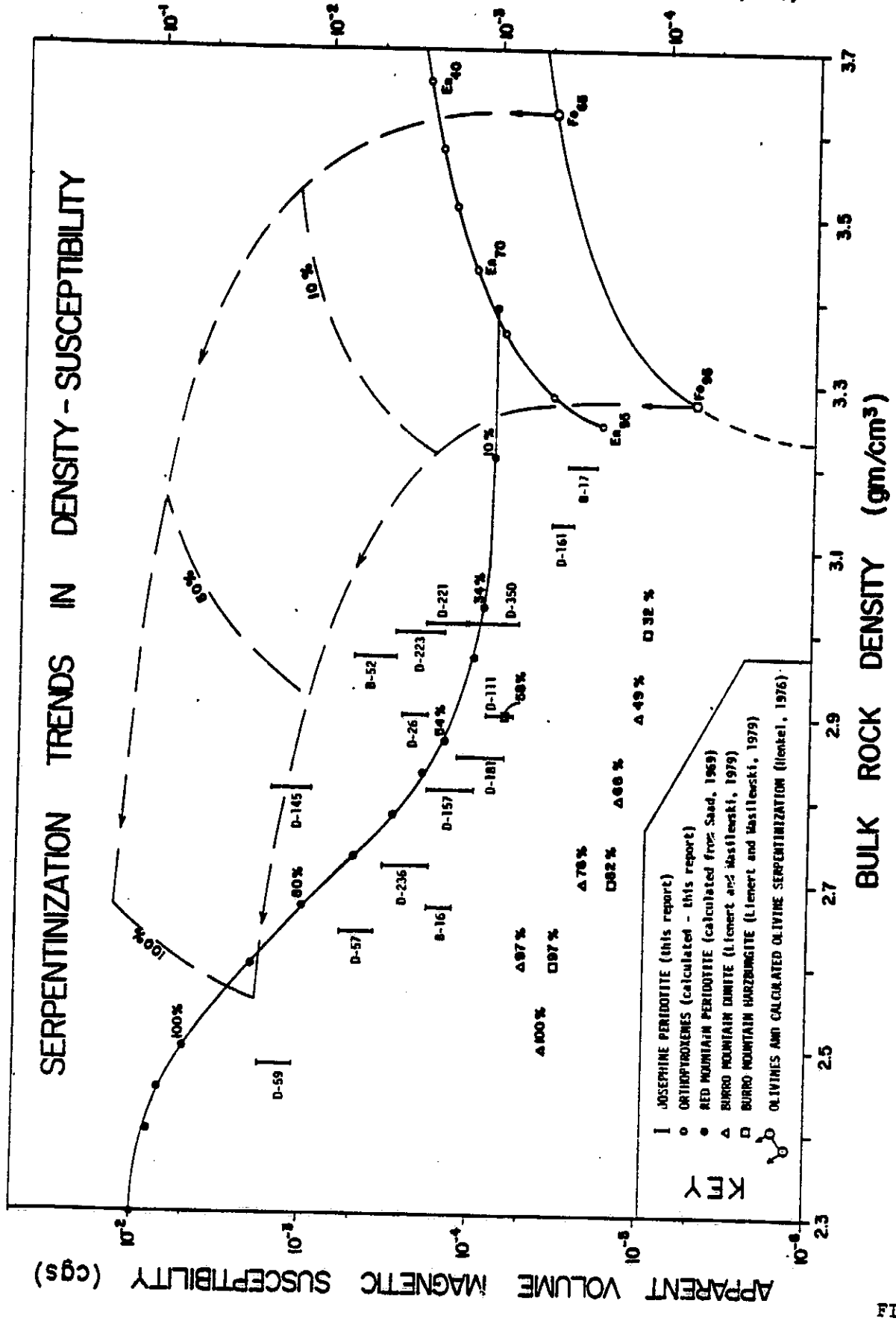

FIG. 6

and decrease respectively with the degree of sepentinization, conforming to general trends culled from the literature. 2) Susceptibilities of the serpentinized harzburgites approach or are in excess of 10^{-3} cgs (10^{-2} S.I.) at about 75 % serpentinization and a density of about 2.6 gm/cm^3. 3) Josephine Creek peridotite samples which depart from the general trend have significant amounts of other magnetic minerals, e.g. metal alloy (awaruite and wairauite), pyrrhotite or chromite.

Summary

We have illustrated the T and fO_2 stability of co-existing Fe-Ni alloy and magnetite, and find the stability field to be consistent with models presented in the previous section. We have described the prevalent metal alloy compositions present in the Josephine Creek serpentinites, and have noted Ni-Fe compositions not conforming to the awaruite stoichiometry. We have defined the susceptibility-density field for serpentinized ultra-mafic rocks, and have shown that the geophysical signature of such rocks is a strong magnetization associated with a low density.

3) MAGNETIC SPINELS AND RELATED PHASES FROM MANTLE-DERIVED KIMBERLITES

Significance

It is frequently assumed that the Earth's mantle is non-magnetic and that lithospheric magnetization resides entirely in the crust, above the seismic Moho. However, detailed examinations of mantle-derived materials specifically with a view to the presence and origin of opaque phases and their magnetic significance are few and far between.

Results

A detailed petrographic and electron microbeam study of intrusive kimberlite dike materials from the Koidu complex, Sierra Leone has revealed high concentrations of spinels and magnetite. The materials are fine grained and in the case of the dikes intrusion depths are placed at 2-3 km. From the silicate phase equilibria and the association of diamond-bearing nodules the kimberlites demonstrably originated at depths in excess of 100 km. The depths of equilibration of Fe-Ti oxides in these rocks remains to be precisely determined but must have been consistent with the MW buffer (see Fig. 5 in Appendix 1). The equilibration trends of magnesian ilmenites clearly show that ferrimagnetic phases approaching Fe_3O_4 in composition result from subsolidus reactions. The analytical data are deferred to Appendix 2 and are

summarized in Fig. 7, where the significant trend to be noted is from Cr-rich spinels at the base of the prism toward Fe_3O_4 at the apex.

In the broader context of iron-related phase equilibria and the importance of oxygen fugacity, we also report the existence of a phase which appears to be a new mineral, designated mineral "H" (Tompkins, 1983). Compositions are detailed in Appendix 2 and summarized in Fig. 8. The mineral is considered to be analogous to a Mg-Al-Ti-Cr-wüstite-type mineral. Oxygen fugacities for formation of this mineral are estimated to be low, on the order of 10^{-11} to 10^{-12} atms at 1100^{o}c, but the magnetic significance of this phase remains to be established. X-ray data are required in order to establish the crystal structure and the magnetic ordering of the phase, but small grain sizes (≈ 0.05 mm) have so far prevented extraction of discrete grains.

A further indication of the possible magnetic significance of mineral "H" is drawn from paleomagnetic experiments on cores from Dike Zone B at Koidu (Tompkins 1983). Iron-bearing phases observed in these specimens include ilmenites, spinels, pyrrhotite, mineral "H" and iron metal. On a Zijderveld plot (Fig. 9a) there are two components of magnetization, overlapping in their coercive force specta. The early removal of a soft component is attributed to iron metal and mineral "H", the latter expected to have a coercive force intermediate between that of iron metal and magnetite. The decay of magnetic intensity (Fig. 9c) of core 403 is also consistent with the early removal of a low coercivity component.

Summary

We have shown 1) that kimberlitic ilmenites are capable of breaking down to form ferrimagnetic spinels close to magnetite in composition, and that this occurs at depths between ≈100 km and the Earth's surface, and 2) that detailed petrographic, electron microbeam and paleomagnetic studies implicate highly reduced iron minerals as significant in kimberlite magnetism.

4) MAGNETITE AND MAGNETIC SUSCEPTIBILITY RELATIONSHIPS

Significance

In order to either interpret or model magnetic anomalies on a mineralogical basis and as due to induced magnetization it is necessary to quantify the relationship between mangetic mineral content and magnetic susceptibility. Furthermore, if metal alloys are to be invoked as partially responsible for magnetization, it is vital to first understand the role to be played by mag-

Figure 7. Compositional spinel trends for Koidu, summarized from Appendix 2, plotted on the oxidized spinel prism and compared with spinel trends from southern Africa and Canadian shield. Mt = magnetite; Mag.fer. = magnesio-ferrite; Her = hercynite; Sp = spinel; Chr = chromite; Pic.chr. = picro-chromite. Kimberlitic trend 1 is from Mitchell and Clarke (1967), and trends 2 and 3 are from Haggerty (1976). Note especially that the trend for Koidu spinels is from the base of the prism toward compositions close to Fe_3O_4 at the apex.

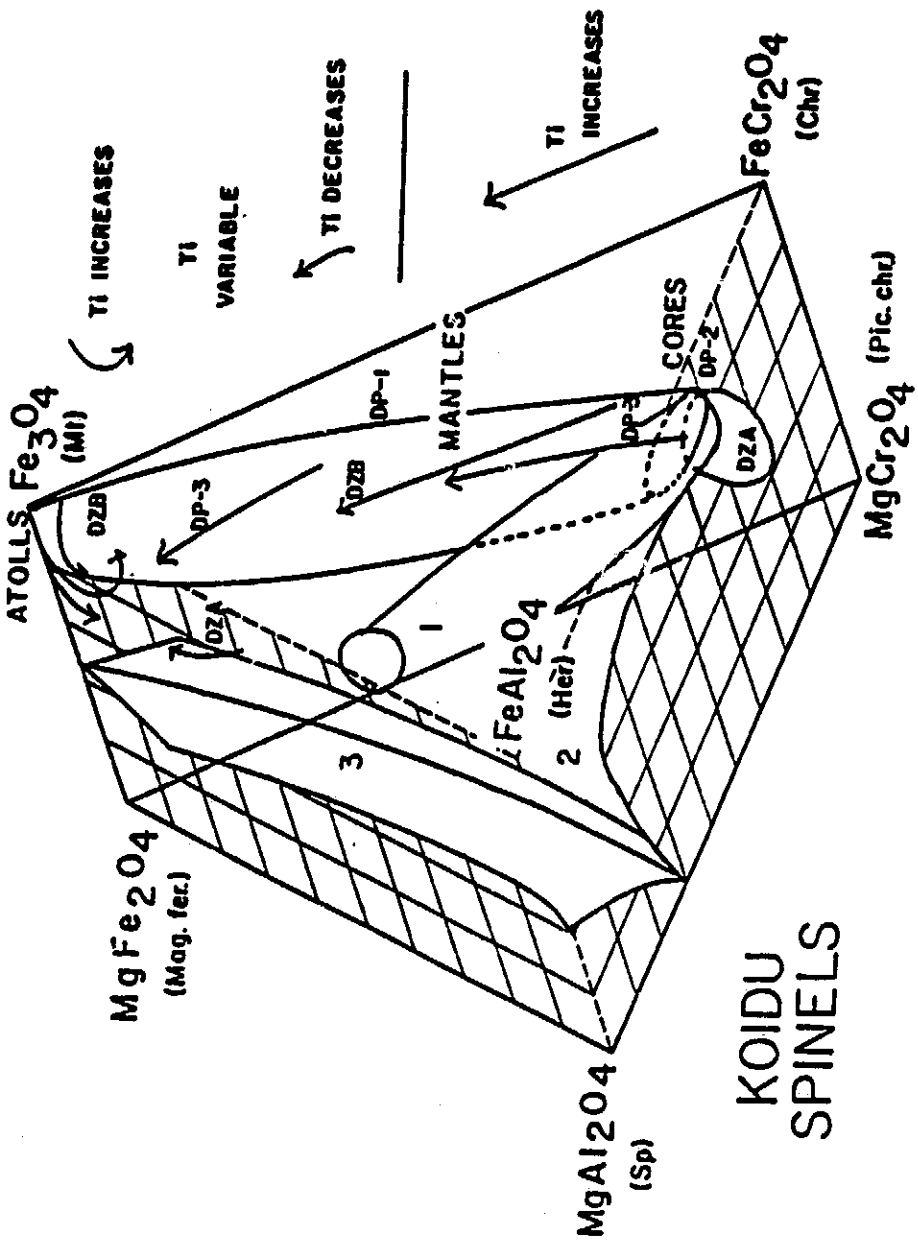
ATOLLS
Fe_3O_4 (Mt)
TI INCREASES
TI VARIABLE
TI DECREASES
TI INCREASES
MANTLES
CORES
DZB
DZA
DP-1
DP-2
DP-3
$FeCr_2O_4$ (Chr)
$MgCr_2O_4$ (Pic. chr)
$MgFe_2O_4$ (Mag. fer.)
$FeAl_2O_4$ (Her)
$MgAl_2O_4$ (Sp)
1
2
3
KOIDU SPINELS

FIG. 7

Figure 8. Mineral "H" is plotted as a function of atomic proportions in terms of Ti, R^{2+} and R^{3+}. The field of wüstite ($Fe_{1-x}O$) is outlined in the hatched area, and the spinel is drawn connecting endmember ulvöspinel ("Usp") to magnetite (Mt) or chromite (Chr). Stoichiometry of mineral "H" is represented as M_6O_7. See Appendix 2 for analyses of mineral "H".

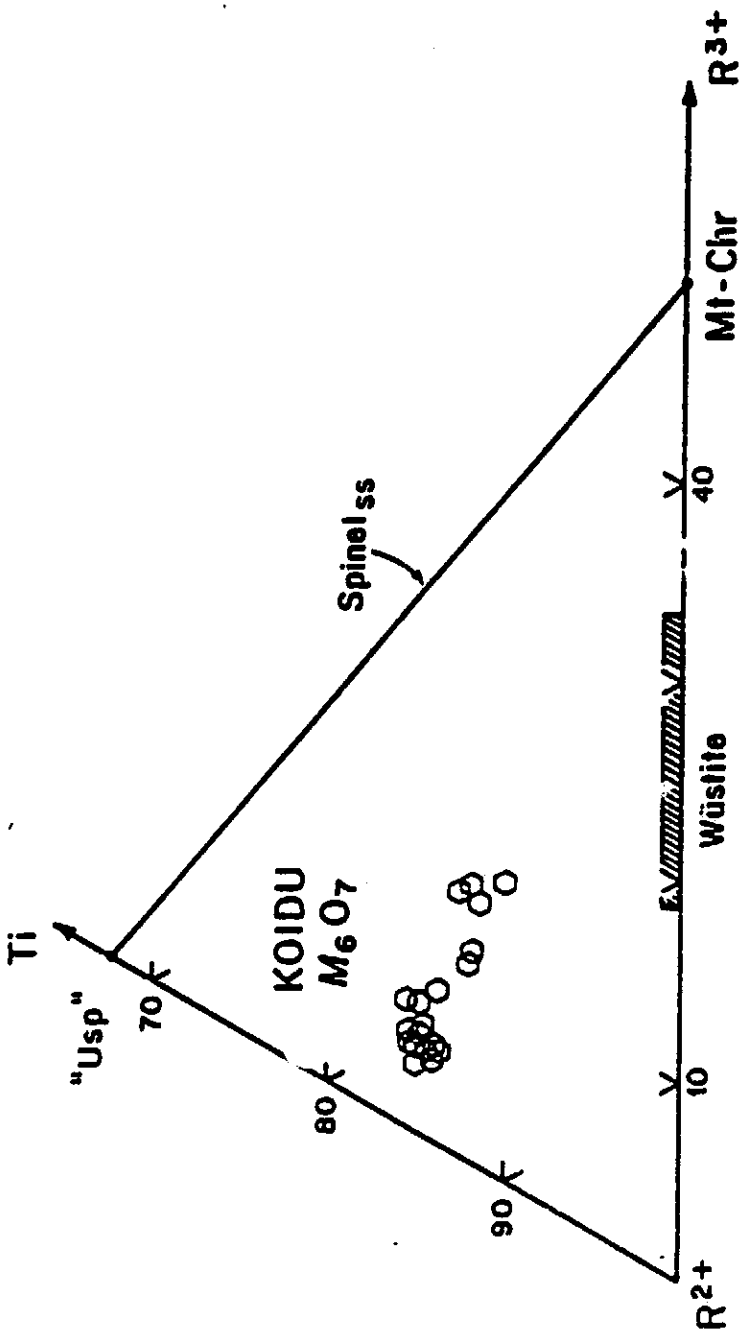

FIG. 8

Figure 9. Alternating field demagnetization data to 50 MT for Dike Zone B (samples 401, 402, 403). (A) Zijderveld plot, with the area around the origin enlarged in A. Open circles = vertical component of magnetization (E-W versus U-D); solid circles = horizontal component of magnetization (E-W versus N-S); W =west; E = east; N = north; S = south; U = up; D = down. (B) demagnetization decay curve. (C) demagnetization decay curve normalized to NRM intensity.

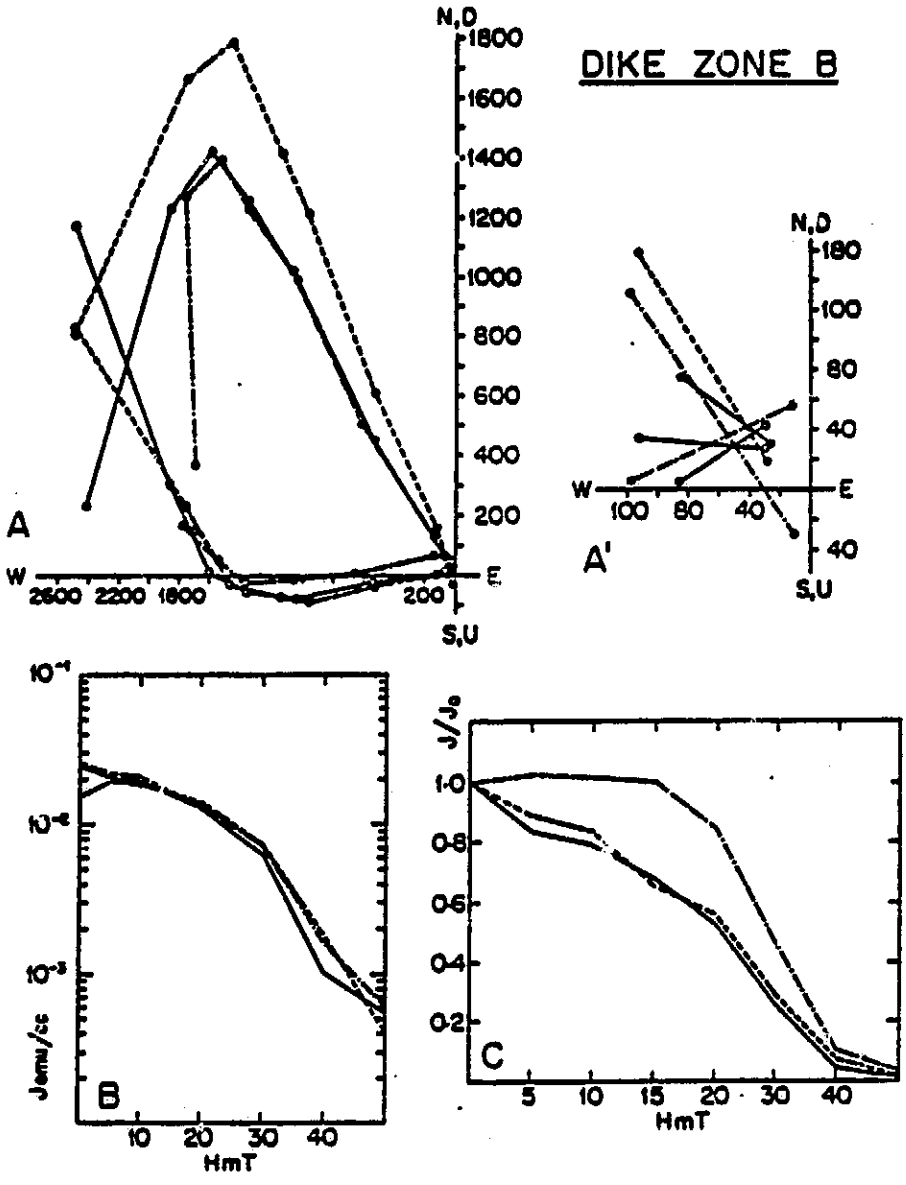
DIKE ZONE B
N,D
1800
1600
1400
1200
1000
800
600
400
200
A
W
2600 2200 1600
200
E
S,U
N,D
180
100
80
40
W
100 80 40
E
A'
40
S,U
B
HmT
10 20 30 40
C
J/Jo
1.0
0.8
0.6
0.4
0.2
5 10 15 20 30 40
HmT

FIG. 9

netite. In addition, as noted above, iron oxides and alloys are subject to redox conditions. This section evaluates the relationship between the oxidation state and amount of magnetite present in a rock and the resultant magnetic susceptibility.

Results

Fig.10 presents the results of a literature search and compilation of relationships between volume % magnetite versus room temperature susceptibility. Although there is a large degree of scatter within each data set and the relation is plotted in log-log space, the good overall agreement between different sets of natural samples and between the empirical and theoretical relations provides a guide for magnetic anomaly interpretation based on induced magnetization. On this basis, induced magnetizations in the range 1-10 A/m are generated in the Earth's field by 1-10 volume per cent magnetite, ranges normally attained only by basaltic rocks and iron-formations.

However, this apparently useful and consistent relationship is misleading in two respects, as illustrated in Fig.11 which shows in more detail the data compiled by Dunlop (1974), simplified in Fig.10 as a straight line. Fig.11 demonstrates 1) that the room temperature susceptibility of a given rock type may vary over a wide range, and 2) that for basalts, and by implication other rocks, the susceptibility depends not only on the amount of opaque oxide minerals generally identified as magnetite, but also depends critically upon the oxidation state of these minerals. This is dearly illustrated in the top right of the figure, where, for a given amount of "magnetite", the susceptibility varies according to oxidation state, such that the more highly oxidized samples have lower magnetic susceptibilities.

Summary

We have confirmed that there exists a first order correspondence between magnetite content and magnetic susceptibility and that this may be loosely correlated with lithology. Induced magnetizations of 1-10 $A.m^{-1}$ require 1-10 vol % Fe_3O_4 at room temperature. Most significantly, in view of previous discussion as to the redox state of the lithosphere, we have pointed out that oxidation state is a critical parameter affecting susceptibility, by virtue of the redox response of Fe-Ti oxides.

Figure 10. Relationships of apparent magnetic susceptibility with volume % magnetite. Empirical relationships are for rocks from the Adirondacks (Balsley and Buddington, 1958), Minnesota (Mooney and Bleifuss, 1953) and diverse locations (Dunlop, 1974), along with the theoretical relationship of Stacey and Bannerjee (1974), a two-fold thermally enhanced susceptibility (Dunlop, 1974), and typical average susceptibility ranges (Dobrin, 1976; Nagata, 1961). Named rocks are from Minnesota (Mooney and Bleifuss, 1953). Mantle xenolith specific susceptibilties (Wasilewski et al., 1979), recalculated to volume susceptibilities on the basis of average densities from Daly et al. (1966) and Robie et al. (1966), are shown with horizontal bars. The susceptibility ranges for induced magnetizations of 1 A/m and 10 A/m over the range of intensity of the Earth's magnetic field are also illustrated. Note that the left and right ordinate scales are equivalent: $k_{vol;S.I.} = 4\pi k_{vol;cgs}$.

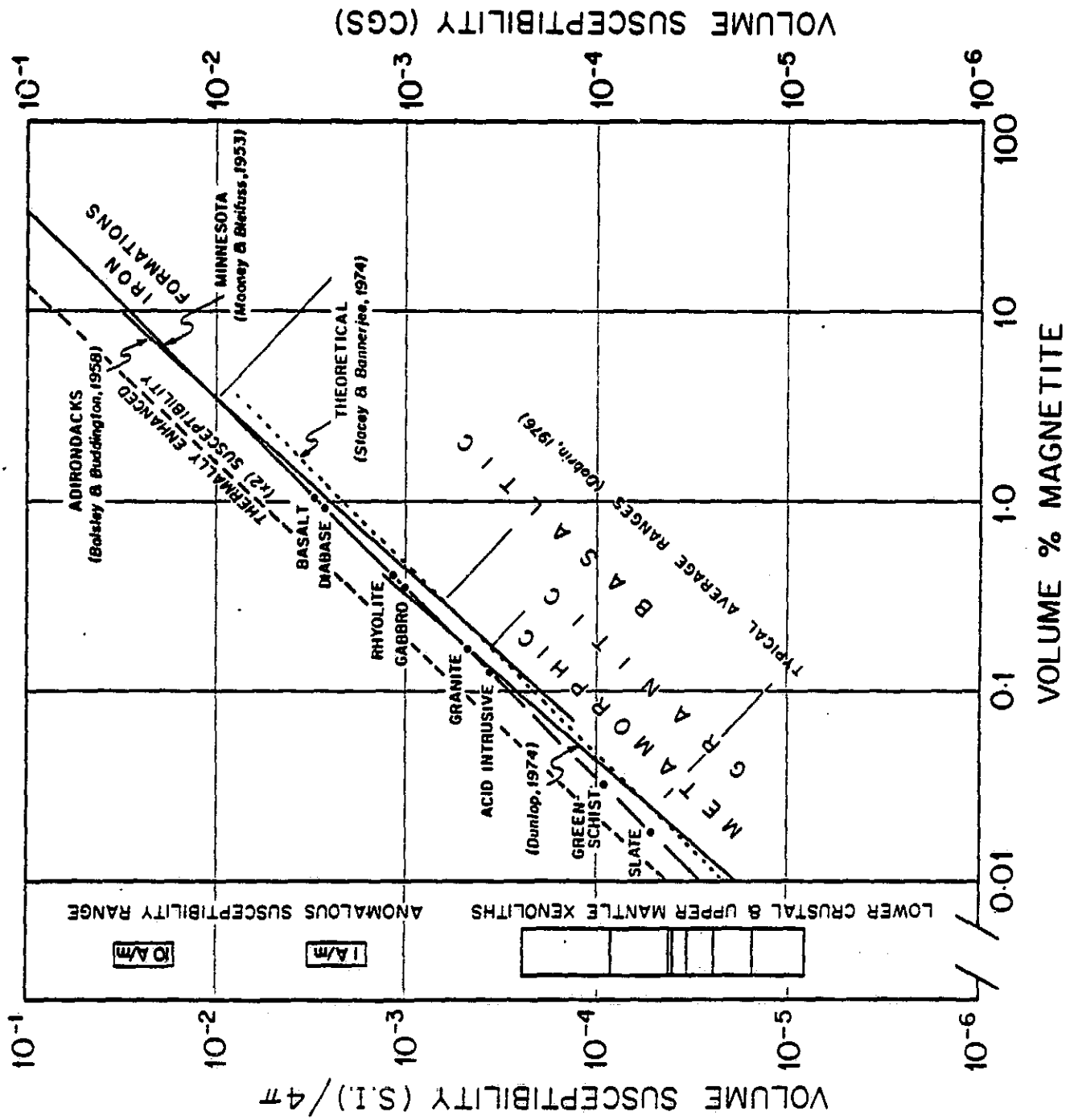
VOLUME SUSCEPTIBILITY (CGS)
VOLUME SUSCEPTIBILITY (S.I.)/4π
VOLUME % MAGNETITE
10⁻¹
10⁻²
10⁻³
10⁻⁴
10⁻⁵
10⁻⁶
100
10
1·0
0·1
0·01
IRON FORMATIONS
MINNESOTA (Mooney & Bleifuss, 1953)
THEORETICAL (Stacey & Banerjee, 1974)
ADIRONDACKS (Balsley & Buddington, 1958)
THERMALLY ENHANCED (χ2) SUSCEPTIBILITY
BASALT
DIABASE
RHYOLITE
GABBRO
GRANITE
ACID INTRUSIVE
(Dunlop, 1974)
GREEN-SCHIST
SLATE
METAMORPHIC
PLUTONIC
BASALTIC
(Doborn, 1976)
TYPICAL AVERAGE RANGES
LOWER CRUSTAL & UPPER MANTLE XENOLITHS
ANOMALOUS SUSCEPTIBILITY RANGE
1 A/m
10 A/m

FIG. 10

Figure 11. Apparent volume magnetic susceptibility versus volume % magnetite, plotted from a compilation of data by Dunlop (1974). Roman numerals attached to the basalt data points are the oxidation indices of Wilson and Watkins (1967), wherein Class I is homogenous titanomagnetite, and progressive oxidation is toward Class V pseudomorphing of titanomagnetite by pseudobrookite and hematite or by spinel and rutile and hematite.

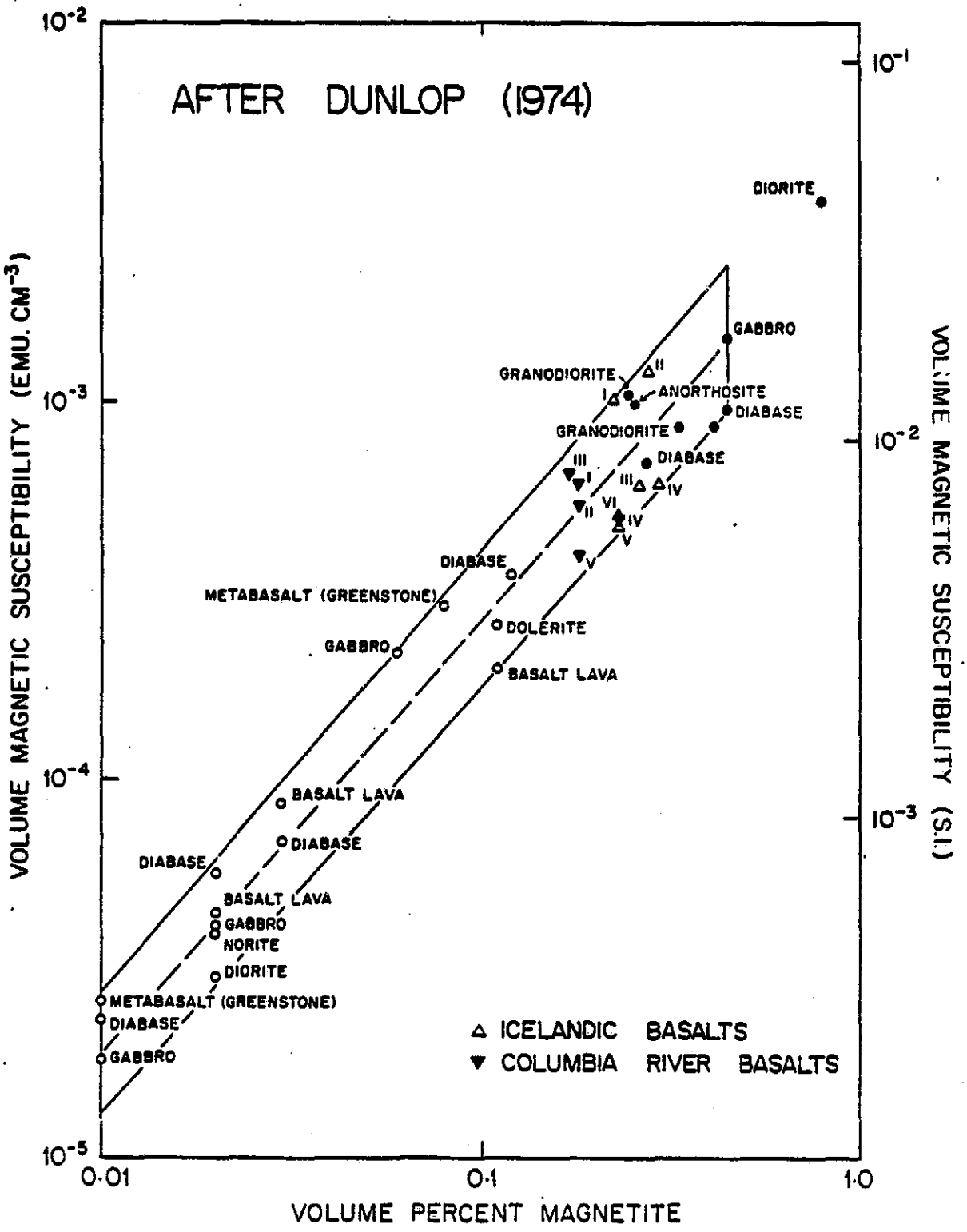
AFTER DUNLOP (1974)
VOLUME MAGNETIC SUSCEPTIBILITY (EMU.CM⁻³)
VOLUME MAGNETIC SUSCEPTIBILITY (S.I.)
VOLUME PERCENT MAGNETITE
10⁻²
10⁻³
10⁻⁴
10⁻⁵
10⁻¹
10⁻²
10⁻³
0·01
0·1
1·0
DIORITE
GABBRO
GRANODIORITE
ANORTHOSITE
DIABASE
GRANODIORITE
DIABASE
DIABASE
METABASALT (GREENSTONE)
DOLERITE
GABBRO
BASALT LAVA
BASALT LAVA
DIABASE
DIABASE
BASALT LAVA
GABBRO
NORITE
DIORITE
METABASALT (GREENSTONE)
DIABASE
GABBRO
△ ICELANDIC BASALTS
▼ COLUMBIA RIVER BASALTS

FIG. 11

5) MAGSAT VECTOR ANOMALIES RELATED TO THE WEST AFRICAN AND AMAZONIAN CRATONS

Significance

Most interpretations of the MAGSAT anomaly maps to date have employed the total field anomalies. Much of our analytical data on magnetic mineralogy and oxidation profiling stems from rocks collected within west Africa. We have examined the MAGSAT vector anomaly maps for the regions of west Africa and northern South America, alone and in relation to the regional geology and geophysics, drawing upon our field experience and our mineralogical data.

Results

The principal result is our manuscript "MAGSAT vector anomalies related to the west African and Amazonian cratons", reproduced as Appendix 3.

Summary

Following is the abstact form our manuscript:

ABSTRACT

MAGSAT (MGST 4/81) anomalies are similar over the West African and Amazonian cratons. Differences between total field (ΔB) and N-S horizontal vector (ΔX) anomalies over both cratons are largely those that would be expected for anomalies due to induced magnetization. At the present low magnetic inclinations, the negative ΔX anomalies which are spatially associated with the cratonic shields imply normally-directed positive magnetization-contrast sources. Archean nucliee of the shields appear to be more strongly magnetized than Proterozoic segments, but both stand out from adjacent basins and ford belts, Under specified conditions, the uncertainty inherent in the poorly defined MAGSAT anomaly profiles taken along opposite siedes of the continental rejoin in a pre-drift reconstruction. Synthesis model anomalies generated form lithological and gravity data roproduce reasonably well the cratonic negative MAGSAT anomalies. The dominant contribution to MAGSAT ΔX anomalies over the West African and Amazonian cratons results from magnetization contrasts within the crust. These are modulated by the effects of structural contrasts, intrusions and metamorphism within the lithosphere, and are localized by the preferred distribution of iron deposits into the more ancient crustal blocks.

6) NATIVE IRON AND THE OXIDATION STATE OF THE CONTINENTAL LOWER CRUST

Significance

Although we have developed models for the gross oxidation profile of the upper mantle, the oxidation state of the continental lower crust has not been firmly established, to-date. This knowledge has remained a vital missing link, given the dependence of magnetic mineralogy upon oxidation state. An integral part of our research related to MAGSAT has been an effort to identify materials of unquestioned lower crustal origin which could shed light on this problem. This section describes the results of this search.

Results

The principal result is our recognition of native iron in lower crustal granulites recovered from a Kimberlite pipe in west Africa; the phase equilibria and magnetic mineralogy strongly suggest that the lower crust is in a highly reduced state and that iron metal may contribute to MAGSAT anomalies. Full details of this research are in our manuscript "Native iron in the continental lower crust: petrological and geophysical implications", submitted to Science (August, 1984), see Appendix 4. The abstract follows:

Abstract. Lower crustal granulite xenoliths recovered from a kimberlite pipe in west Africa contain native iron (Fe^{o}) as a decomposition product of both garnet and ilmenite. Magnetic measurements show that less than 0.1 volume per cent of iron metal is present. Geothermometry and oxygen geobarometry indicates that the oxide and metal phases equilibrated between iron-wüstite and magnetite-wüstite buffers which may represent the oxidation state of the continental lower crust, and the depleted lithospheric upper mantle. Ferromagnetic Fe^{o} could be stable to a depth of ≈95 km, and should be considered in the interpretation of long wavelength static magnetic anomalies.

Summary

We have shown that native iron is present in some lower crustal granulites, and that the continental lower crust is probably at low oxidation levels compatible with metal and metal alloy stability fields. The implication for MAGSAT is that the interpretation of anomalies needs not, in fact should not, be constrained as due to magnetite. The magnetic outer shell of the Earth may be as thick as ≈100 km in places and iron metal, and perhaps other metal alloys, should be considered in any interpretation of MAGSAT magnetic anomalies.

SUMMARY

We have provided extensive data on magnetic minerals and their host rocks, particularly for serpentinized ultramafic rocks, lower crustal metamorphic rocks and kimberlitic suites. We have established oxidation profiles for the crust and mantle, and we have summarized the results of many hundreds of electron microbeam analyses describing the chemistry and phase relations of Fe-Ti oxides in mantle rocks, and of oxides and alloys in a collection of serpentinized peridotites and a collection of lower crustal granulites.

Overall, we conclude from our analytical and experimental data that magnetization need not be confined to the seismic crust and that magnetic oxide and alloy compositions are geochemically stable under lower crustal and mantle conditions; although it is not necessary for modelling purposes alone to invoke a mantle source for any particular MAGSAT anomaly, our data demonstrate that the hypothesis that only the crust is magnetized and that only magnetite is responsible for magnetization is simply an assumption of convenience, and one which is misleading.

We have analyzed qualitatively the MAGSAT maps over shield regions in west Africa and northern South America, and have demonstrated very similar relationships for both regions. Obvious among the results from this work is the observation that large deposits of iron ore are visible in the MAGSAT maps.

In conclusion, it is re-emphasized that magnetic anomaly interpretations is dependant upon knowledge of the mineralogy, and that the MAGSAT anomaly maps demonstrably represent the integrated effects of magnetic minerals within the mantle, within the crust, and exposed at the very surface of the Earth. The two overriding constraints in our analysis are that temperature and oxygen fugacity (and hence composition) remain the most significant model-limiting parameters in the interpretation of MAGSAT anomalies.

REFERENCES

Balsley, J.R., and A.F. Buddington, Iron-titanium oxide minerals, rocks and aeromagnetic anomalies of the Adirondack Area, New York, Econ. Geol., 53, 777-805, 1958.

Daly, R.A., G.E. Manger, and S.P. Clark, Jnr., Density of rocks, in Handbook of Physical Constants, Geol. Soc. Amer. Memo., 97, edited by S.P. Clark, Jnr., pp. 19-26, Geol. Soc. Amer., New York, 1966.

Dobrin,M., Introduction to Geophysical Prospecting, 3rd edition, 630 pp., McGraw-Hill, New York, 1976.

Dunlop, D.J., Thermal enhancement of magnetic susceptibility, J. Geophys., 40, 439-451, 1974.

Eggler, D.H., and D.R. Baker, Reduced volatiles in the system C-O-H: Implications to mantle melting, fluid formation, and diamond genesis. In S. Akimota and M.H. Manghnani, Eds., Advances in Earth and Planetary Sciences. High-Pressure Research in Geophysics, 12, 237-250, 1982.

Haggerty, S.E., Opaque mineral oxides in terrestrial igneous rocks, in Oxide Minerals, Min. Soc. Amer. short course notes, vol. 3, edited by D. Rumble, pp. Hg101-Hg300, 1976.

Henkel, H., Studies of density and magnetic properties of rocks from Northern Sweden, Pure Appl. Geophys., 114, 235-249, 1976.

Lienert, B.R., and P.J. Wasilewski, A magnetic study of the serpentinization process at Burro Mountain, California, Earth Planet. Sci. Lett., 43, 406-416, 1979.

MacMahon, B, Petrologic redox equilibria in the Benfontein kimberlite sills and in the Allende meteorite, and the T-fO_2 stability of kimberlitic ilmenite from the Monastery diatreme, unpublished Ph.D. dissertation, Univ. of Massachusetts, 1984.

Mitchell, R.H. and D.B. Clark, Oxide and sulphide mineralogy of the Peuyuk kimberlite, Somerset Island, N.W.T., Canada. Contributions to Mineralogy and Petrology, 56, 157-172, 1976.

Mooney, H.M., and R. Bleifuss, Magnetic susceptibility measurements in Minnesota, Part II, Analysis of field results, Geophysics, 18, 383-393, 1953.

Nagata, T., Rock Magnetism, 2d. Rev. ed., 350 pp., Plenum, New York, 1961.

Robie, R.A., P.M. Bethke, M.S. Toulmin, and J.L. Edwards, X-ray crystallographic data, densities, and molar volumes of minerals, in Handbook of Physical Constants, Geol. Soc. Amer. Memo., 97, edited by S.P. Clark, Jnr., pp. 27-76, Geol. Soc. Amer., New York, 1966.

Saad, A.H., Magnetic properties of ultramafic rocks taken from Red Mountain, California, Geophysics, 34, 974-987, 1969.

Stacey, F.D., and S.K. Bannerjee, The Physical Principles of Rock Magnetism, Developments in Solid Earth Geophys., vol.5, 195 pp., Elsevier, New York, 1974.

Tompkins, L.A., The Koidu kimberlite complex, Sierra Leone, west Africa, unpublished M.Sc. thesis, Univ. of Massachusetts, 1983.

Wasilewski, P.J., H.H. Thomas, and M.A. Mayhew, The Moho as a magnetic boundary, Geophys. Res. Lett., 6, 541-544, 1979.

Wilson, R.L., and N.D. Watkins, Correlation of petrology and natural remanent magnetization in Columbia Plateau basalts, Geophys. J., 12, 405-424, 1967.

APPENDICES

APPENDIX 1 Oxidation profiling of the crust and mantle

APPENDIX 2 Magnetic spinels and related phases from mantle-derived kimberlites: analytical data

APPENDIX 3 MAGSAT vector anomalies related to the west African and Amazonian cratons

APPENDIX 4 Native iron in the continental lower crust: petrological and geophysical implications

APPENDIX 1

OXIDATION PROFILING OF THE CRUST AND MANTLE

Redox state of the Earth's upper mantle from kimberlitic ilmenites

.S.E. Haggerty and L.A. Tompkins

Nature, 303, 295-300, 1983

ORIGINAL PAGE IS
OF POOR QUALITY

diamonds[10], and the sources of deep-seated magnetic anomalies[11,12]. Although the study of mantle nodules to determine the redox state of the upper mantle is in its infancy there has been considerable debate on whether it is reduced[13,14] and is equivalent to equilibrium conditions defined by iron–wüstite (IW), or on whether it is more oxidized[15–17] and, hence, is more appropriately defined by equilibria consistent with magnetite–wüstite (MW) or fayalite–magnetite–quartz (FMQ). In the extreme case at magmatic temperatures (1,200 °C), these estimates differ by approximately five orders of magnitude in oxygen fugacity (f_{O_2}). Translated, this difference is similar to the differences between the oxidation states of lunar and terrestrial basalts, a disparity that is unreasonably large. In this study we conclude that the source region is compatible with WM–FMQ and possible explanations for the diversity of redox states reported include the ages of the mantle being sampled and whether that portion of the mantle is mature and depleted, or juvenile and enriched in volatiles.

Three methods have been used to estimate the redox condition of the upper mantle, and all rely on the variations of iron: oxygen ratios in minerals and on the magnitude of Fe^{2+}/Fe^{3+} concentrations. Thermodynamic techniques rely on theoretical solution models for coexisting minerals[16,17]. In the intrinsic f_{O_2} method, furnace gas mixtures (CO or CO_2+H_2) are adjusted as a function of temperature (T) to match the redox state of the sample[13,14]. In the third technique, exchange equilibria between Fe and Ti, and between Fe^{2+} and Fe^{3+}, define unique solutions for T and f_{O_2} in co-equilibrated members of the ilmenite and spinel mineral series[18]. The present study used the last of these methods and it has also been used to estimate the redox states of planetary basalts[15]. A critical factor in this application is that the mineral pair is demonstrated to have co-equilibrated, a situation that is difficult to prove because ilmenite and spinel members are typically discrete constituents in igneous and metamorphic rocks. In the assemblages described here, however, the two components are in the grain boundary contact, and ionic exchange between ilmenite and spinel, in response to external environmental conditions, is reassured.

Samples and analytical techniques

One aspect of an extensive geochemical programme on the characterization of the West African kimberlites and their associated upper-mantle derived nodule suites[19,20], has been a detailed investigation of the oxide minerals for exploration purposes, magnetic properties and because of their sensitivity to modification in oxidizing or reducing conditions. Ilmenite occurs in great abundance in the Cretaceous kimberlite fields of Liberia, Sierra Leone and Guinea, and ilmenite is part of the discrete nodule suite typical of other kimberlite provinces, but debated in terms of their precise depths of origin[21]. That ilmenite nodules in kimberlites originate in the upper mantle is indisputable. This is borne out by diamond inclusion studies[22,23], by garnet and pyroxene intergrowths[21,23], and by high-pressure, high-temperature phase-equilibria experiments[24,25], that all include ilmenite as a component.

The ilmenites we have examined are typically 1–2.5 cm in diameter with some as large as 15 cm. Spherical or oblate spheroidal in shape, the ilmenites are free of surface weathering but occasionally show some reaction with the enclosing kimberlite, manifested by very thin veneers of late stage perovskite and associated calcite. Examined in reflected light and under oil-immersion microscopy, a large number of ilmenites are observed to contain parallel, oriented lamellae (20–100 μm in width) of spinel (titanomagnetite) that are crystallographically controlled along {0001} rhombohedral ilmenite planes. Among these samples are two contrasting types of assemblages. In some ilmenites from the Koidu Complex, Sierra Leone, exsolution of ilmenite lamellae within the host ilmenite has taken place, and this process is followed, or accompanied by subsolidus equilibration that has also formed spinel (Fig. 1*a*). Rounded

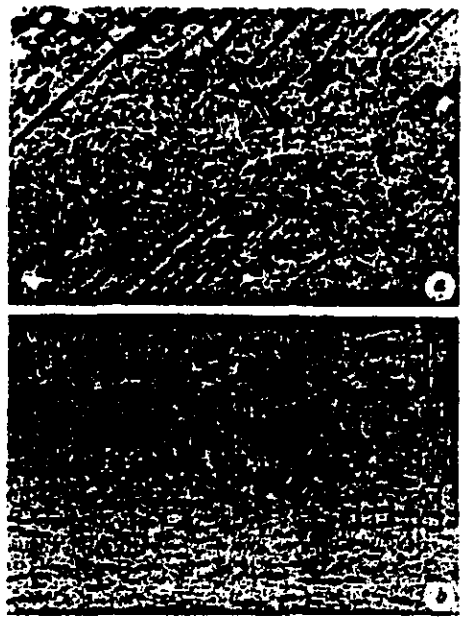

Fig. 1 Reflected light photomicrographs taken under oil-immersion objectives. The width of each plate is 0.475 mm. The field of view shown in *a* is typical of assemblages observed in ilmenite megacrysts from Koidu, Sierra Leone. The light grey, host ilmenite is the original (I_o) ilmenite that has undergone partial re-equilibration to ilmenite (I) + spinel. The bright and highly reflective areas are carbonate inclusions or minor sulphides. In *b* the dark oriented lamellae are spinel in an ilmenite host typical of megacrysts from Liberia, and the Antoschka kimberlite pipe in Guinea.

or curvilinear liquid immiscible sulphide (pyrite, pyrrhotite, pentlandite, chalcopyrite) and carbonate inclusions are present, and the spinels are interpreted to derive from subsolidus reduction. In other ilmenites from Koidu, and in all of the ilmenites from Liberia and Guinea (Antoschka pipe), the textural relations consist simply of parallel sets of spinel lenses elongated along {0001} ilmenite planes (Fig. 1*b*). These assemblages also result from reequilibration, and it is assumed, based on experimental studies[18,26], that solid state reconstitution has taken place in reducing conditions, transforming homogeneous ilmenite into a compositionally modified ilmenite + spinel. This textural and mineral relation is described as reduction exsolution. Although we cannot demonstrate that reduction took place in the source region, this appears most probable, and the process was deuteric modification with prolonged cooling. We can confidently eliminate the irruptive kimberlite event as the reduction agent, because of exsolution (*sensu stricto*) of ilmenite and the rarity of external reactions.

Compositions of coexisting spinel and ilmenites were determined by electron microbeam techniques using an ETEC Autoprobe, natural and synthetic mineral standards, and conventional correction procedures[27,28], with standard operating conditions (15 kV and 0.03 nA specimen current). Iron(II) concentrations were calculated assuming ideal analyses and mineral stoichiometry. Reliable analyses were only possible on the coarsest intergrowths, and only those data for which repeated and reproducible compositions were obtained are considered. Averages presented are a minimum of 10 analyses.

Upper-mantle derived oxides are commonly enriched in MgO, MnO, Cr_2O_3, and Al_2O_3, and in the classical application of Buddington and Lindsley's[18] Fe–Ti oxide geothermometer and oxygen geobarometer, T and f_{O_2} estimates were only possible in assemblages having negligible contents of elements other than Fe–Ti–O. A revised thermodynamic model[29], and a method of treating these other components has been proposed[30], and the T and f_{O_2} of coexisting oxides in kimberlites can now be obtained using the equations: X_{Ilm} =

After integrating equation (14) we define

$$\bar{V} = -\frac{\partial}{\partial r}(rv)/r\rho = -(l-1)\xi_n[g(r-r_1) - p(r_1)/\rho]/r^2 \quad (15)$$

The θ and ϕ components of the transverse poloidal acceleration are respectively[12] $\partial\bar{V}/\partial\theta$ and $(\partial\bar{V}/\partial\phi)/\sin\theta$. The second term in the bracket is dominant. The spherical harmonic angular dependence of ϕ' is also present in ξ_n and in $\bar{V}$. Thus the shape of the surface distortion (ξ_n) determines the transverse fluid velocity from equation (15).

Even if there were a non-zero toroidal part of the circulation current the 'whole-disk average' of the Doppler velocity would preclude observing it. The gradient and poloidal parts of the velocity can be observed, but only the poloidal transverse part of a 13-day period can be significant. Choosing the line of sight as the axis of the spherical coordinate system, only the $m = 0$ harmonics (Legendre polynomials) can be observed.

Neglecting limb darkening effects, the symmetry of the whole disk average imposes other restrictions on the results. Except for $l = 2$, spherical harmonics of even degree are unobservable in the whole disk average and $l = 2$ yields only the second harmonic of the core rotation frequency. The $l = 1$ degree cannot occur in ϕ'. The $l = 3$ spherical harmonics yield the fundamental and the third harmonic of the core rotation frequency. The $l = 3$, $m = 3$ mode (referred to the solar axis) is the strongest source of the fundamental period.

If the above interpretation of the data is correct, the $l = 3$ harmonic is probably the source of the circulation current. A detailed comparison with the 1966 observations is not useful, for the telescope was incapable of detecting odd degree spherical harmonics.

Calculating the θ component of the velocity for $l = 3$ from equation (15) and integrating over the solar disk gives

$$A = \frac{Tap(r_1)}{2\pi r^2 \rho} \quad (16)$$

for the velocity amplitude where $\xi_n = aP_3(\cos\theta)$ and T is the core rotational period. Assuming $l = 3$, $\Delta r = r - r_1 = 5 \times 10^7$ cm, $p(r_1) = 5 \times 10^5$, $\rho = 4 \times 10^{-6}$ and $a = 10^6$ cm gives 440 cm s^{-1} for A. The value of the coefficient a was chosen arbitrarily but it is reasonable.

If the above interpretation is correct there is a surprising conclusion. The above value (a) for the odd spherical harmonic distortion ($l = 3$) is fairly large, of the same order of magnitude as $l = 2$ and $l = 4$ distortions[4]. This suggests that if there is a strong magnetic field buried in the solar core, it may be quite complex in form.

The centrifugal distortion due to the rotation of the surface should also drive an Eddington–Sweet current. In this case the flow is from the Equator to the pole and the velocity varies as $\sin 2\theta$. The velocity is limited by turbulent viscosity which is not easily estimated. Also this flow may be dominated by other effects.

Durrant and Schröter[13] have suggested that the Claverie *et al.* 13-day period may be a spectroscopic artefact associated with the rotating magnetically active zones on the Sun's surface. From the plage maps for the same observational period used by Claverie *et al.*, they compute a function (here $D(t)$) which is similar in appearance to the Claverie function. Their effect should exist, but the magnitude is uncertain. I find that a simple sinusoid (Fig. 1) provides a substantially better (robust) fit to the velocity data than does the D function. Also, adding the $D(t)$ term to the sinusoidal fit does not significantly improve the fit. Also, the $D(t)$ fits better if it is phase advanced by 2 days (55°), $D \rightarrow D(t+2)$. I conclude that the Durrant–Schröter effect should exist but that it is probably weak, and perhaps negligible in the Claverie *et al.* data. Edmunds and Gough have independently considered the same artefact. From a study of line formation either side of the potassium line they conclude that the magnitude of the effect is approximately right to account for the observations[14].

This research was supported in part by the NSF.

Received 16 December 1982; accepted 22 March 1983.

1. Claverie, A. *et al. Nature* **299**, 706–707 (1982).
2. Dicke, R. H. & Goldenberg, H. M. *Astrophys. J. Suppl.* **27**, 131–182 (1974).
3. Dicke, R. H. *Solar Phys.* **47**, 475–515 (1976).
4. Dicke, R. H. *Proc. natn. Acad. Sci. U.S.A.* **78**, 1309–1312 (1981).
5. Knight, J. W., Sebastian, K. H. & Sturrock, P. A. *Astrophys. J. Lett.* **227**, L153–L156 (1979).
6. Dicke, R. H. *Proc. Informal Conf. on Status and Future of Solar Neutrino Research* Vol. 2 (ed. Friedlander, G.) 109–143 (Brookhaven National Laboratory, Upton, 1978).
7. Isaak, G. R. *Nature* **296**, 130–131 (1982).
8. Dicke, R. H. *Sol. Phys.* **78**, 3–16 (1982).
9. Hill, H. A. & Stebbins, R. T. *Astrophys. J.* **200**, 471–483 (1975).
10. Menzel, L. *Stars and Stellar Systems* Vol. 8 (eds Aller, L. H. & McLaughlin, D. B.) 465–496 (University of Chicago Press, 1965).
11. Stein, R. F. & Spiegel, E. A. *J. atmos. Sci. Am.* **42**, 866–872 (1967).
12. Dicke, R. H. *Astrophys. Space Sci.* **58**, 275–283 (1978).
13. Durrant, C. J. & Schröter, E. T. *Nature* **301**, 589–591 (1983).
14. Edmunds, M. G. & Gough, D. O. *Nature* **302**, 810–812 (1983).

Redox state of Earth's upper mantle from kimberlitic ilmenites

Stephen E. Haggerty & Linda A. Tompkins

Department of Geology, University of Massachusetts, Amherst, Massachusetts 01003, USA

Temperatures and oxygen fugacities are reported on discrete ilmenite nodules in kimberlites from West Africa which demonstrate that the source region in the upper mantle is moderately oxidized, consistent with other nodule suites in kimberlites from southern Africa and the United States. A model is presented for a variety of tectonic settings, proposing that the upper mantle is profiled in redox potential, oxidized in the fertile asthenosphere but reduced in the depleted lithosphere.

VOLATILES and the oxidation–reduction environment exerted by gas species in the system C–O–H–S are considered to have had profound effects on planetary and atmosphere formation[1] and are critical to petrogenetic models for the generation of magmas within the Earth's upper mantle[2]. The compositions of volatiles in this source region influences degrees of partial melting, the composition of the melt, mass fractionation, liquid lines of descent, valency states of elements, and elemental partitioning coefficients between liquids and solids. Gas sampling of active subaerial volcanoes[2,3] and analyses of trapped volatiles in quenched ocean floor glasses have provided a wealth of new data on volatiles being generated at present[2,4–7]. Sampling of the upper mantle through nodule suites in alkali basalts and kimberlites have received less attention, but the realization that these materials provide direct information on the volatile budget of the mantle and on the redox state of subcrustal regions is rapidly being recognized. These data have far-reaching implications ranging from mantle metallogenesis[8,9], to the origin of

0028-0836/83/210295—06$01.00

© 1983 Macmillan Journals Ltd

OF POOR QUALITY

$(Mg+0.5Al+Fe^{3+})/(0.5Fe^{3+}+Mg+0.5Al+Fe^{2+})$, and $X_{Usp} = (Ti-0.5Mn)/(Ti-0.5Mn+0.5Fe^{3+})$, where X_{Ilm} and X_{Usp} are the mole fractions of ilmenite (in ilmenite solid solution) and ulvöspinel (Fe_2TiO_4) in spinel solid solution, respectively. Uncertainties in T and f_{O_2} (excluding Cr_2O_3) by this method are approximately 40–80 °C and 0.5–1.0 log unit f_{O_2}, assuming ±1% uncertainties in spinel and ilmenite compositions[29]. We have modified the above equations, treating Cr_2O_3 in a manner similar to Al_2O_3 and although the precise effect of these oxides on T and f_{O_2} remains unknown, we estimate that the values are still within the range ~100 °C and ~1 log unit f_{O_2}. These estimates are corroborated by low $Cr_2O_3+Al_2O_3$ mineral pairs and by independent experimental data[31] in which we consider ilmenite alone in the system $FeTiO_3$(ilmenite)–$MgTiO_3$(geikielite)–Fe_2O_3(haematite) as a function of f_{O_2} at constant T (1,300 °C). The data are also consistent with the estimates obtained on kimberlitic ilmenites from southern Africa and the United States, by thermodynamic treatment[17], and using the intrinsic f_{O_2} method[32].

Results

The compositions of 17 ilmenite–spinel pairs (five from Koidu and six each from Liberia and Antoschka) are expressed as major element, combined divalent (FeO+MgO+MnO), trivalent ($Fe_2O_3+Al_2O_3+Cr_2O_3$), and tetravalent (TiO_2) oxides in Fig. 2. Spinels from Koidu lie on or very close to the join Fe_2TiO_4–R_3O_4 and all remaining spinels, with one exception, lie along joins slightly enriched in TiO_2, a reflection of their MgO concentrations. Partitioning of MgO is preferential into ilmenite; hence, all of the ilmenite data fall between $FeTiO_3$ and $MgTiO_3$. An approximate evaluation of these data, in terms of f_{O_2}, may be obtained from the inset in Fig. 2, based on the relative positions of coexisting compositions, and the slopes of tie-lines between ilmenite and spinel solid solution joins[16]. The more enriched Fe^{3+} samples (Koidu) are more oxidized (NNO), and those with higher Fe^{2+} contents (Liberia) are relatively more reduced (WM).

Absolute T and f_{O_2}s obtained from these data are illustrated in Fig. 3, and four of the standard T–f_{O_2} buffers are included for reference. These are IW, WM, FMQ, and MnO–Mn_3O_4. Nine of the 17 oxide pairs lie, within experimental limits, along the FMQ buffer; five pairs are more oxidized than FMQ; and three are more reduced than FMQ. Because the assemblages have undergone reduction–equilibration, original single phase ilmenites must have been stable at f_{O_2}s above those shown for each of the coexisting oxide pairs. Also included in Fig. 3 are data from the Precambrian Premier kimberlite[33], the Cretaceous Oka carbonatite[34], the Benfontein kimberlite–carbonatite sills[35] (also Cretaceous in age), experimental data on ilmenite from the Monastery (Cretaceous) kimberlite[26], along with data from peridotites enclosed in Tertiary alkali basalts[13]. The most striking feature of the diagram is that all data, with the exception of the peridotites, are more oxidized than MW. the peridotites bracket IW, and these data, in common with other equally reduced values on olivine in basalts[35], were made using the intrinsic f_{O_2}, Zr-electrolytic cell technique[36,37]. Kimberlitic ilmenites, however, yield values coincident with FMQ[32]. Oxygen fugacity increases with T but also increases with pressure, and in Fig. 4 the f_{O_2} buffers are corrected to $P = 30$ kbar to illustrate this effect. The extent to which the ilmenite–spinel data are modified at high P is unknown, but the sense of the correction is towards higher values of f_{O_2}. Both the oxide data and the buffer curves will be synchronously displaced with increasing P. However, maintaining the oxide data as uncorrected values, because the correction is considered to be small[18], and assuming 30 kbar, the Koidu data approach FMQ, the Oka and three of the Liberian compositions are equivalent to WM, one is more oxidized and the remainder more reduced. The Antoschka data lie ~1 log unit below WM. Because the precise pressures are not known the relative f_{O_2}s are clearly only estimates.

Kimberlitic ilmenites are dominated by solid solutions among three endmember components ($FeTiO_3$–$MgTiO_3$–Fe_2O_3) and because the oxidation state of iron in two of these endmembers is either exclusively Fe^{2+} or Fe^{3+} (that is ilmenite and haematite, respectively), the stability of any composition within the ilmenite ternary must be f_{O_2} dependent. This f_{O_2} dependency is illustrated in Fig. 5 based on experimental data[31] at 1,300 °C. The West Africa data are shown together with published data on the compositions of ilmenites from kimberlites, worldwide[23,38,39]. Most compositions lie within the range of f_{O_2} between 10^{-6} and 10^{-9} atm. The WM buffer at 1,300 °C and 30 kbar, has an $f_{O_2} = 10^{-6}$ atm. A more appropriate buffer for upper mantle conditions has been proposed by Eggler and Baker[14], which is defined as EMOG, and is the intersection of

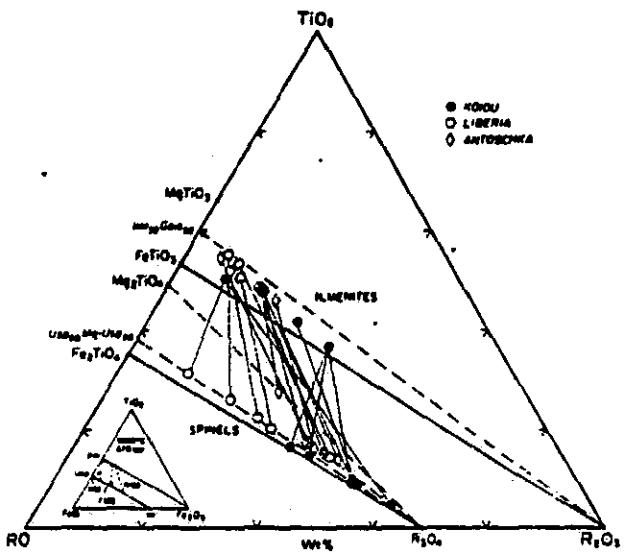

Fig. 2 Electron microbeam analyses of coexisting spinel and ilmenite compositions as a function of RO (FeO+MgO+MnO), R_2O_3 ($Fe_2O_3+Cr_2O_3+Al_2O_3$), TiO_2.

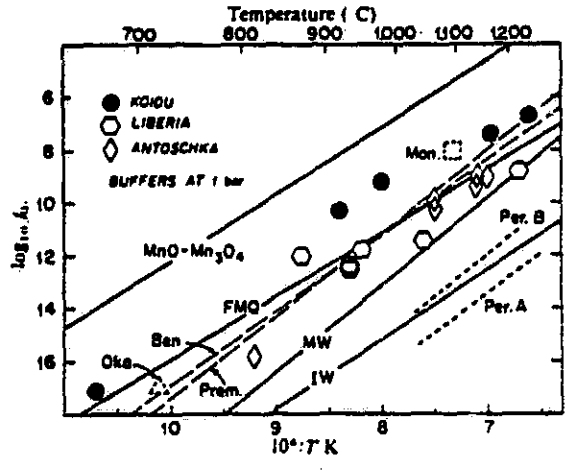

Fig. 3 Temperature–oxygen fugacity relations for coexisting ilmenite–spinel pairs from West Africa (Liberia; Antoschka–Guinea; and Koidu–Sierra Leone) determined according to the methods described in refs 18, 29, 30. Other data shown are for the Premier (Prem.) kimberlite[33], the Oka carbonatite[34], the Benfontein (Ben) kimberlite–carbonatite ills[35], the Monastery kimberlite[26], and peridotites (Per. A and Per. B) in alkali basalts[13,44]. The solid lines are experimental buffers MnO–Mn_3O_4 (*ref. 52*); FMQ (fayalite–magnetite–quartz)[53]; MW (magnetite–wüstite) and IW (iron–wüstite) are from *ref. 54*. The salient feature to be noted is that the peridotite data are considerably more reduced than those from kimberlites and carbonatites.

two univariant reactions: (1) enstatite + magnesite + carbon = forsterite + vapour; with (2) magnetite + carbon = wüstite + vapour. This intersection is at 29.6 kbar, 10^{-7} atm and 1,230 °C. At lower T, EMOG lies between WM and FMQ, but above 1,230 °C at high pressures, graphite is replaced by diamond and EMOD is ~1 log unit more reduced than WM. If the equilibrated data in Figs 3 and 4 are extrapolated to 1,300 °C, parallel to the FMQ buffer, the range in resultant f_{O_2} is $10^{-5.6}$ to 10^{-9} atm. This corresponds almost exactly to EMOG, WM, and the range of compositions in Fig. 5, noting that it is only the ilmenite component of the oxide pair that is considered in this treatment. This estimate in f_{O_2} is consistent with the thermodynamic approach for cocquilibrated oxides and silicates from a variety of upper-mantle derived nodules[17,40], and with intrinsic f_{O_2} data on kimberlitic ilmenite[32]. The estimate is also consistent with the oxygen fugacities of continental basalts in which, ≈90% of the data lie between FMQ and WM[2,38].

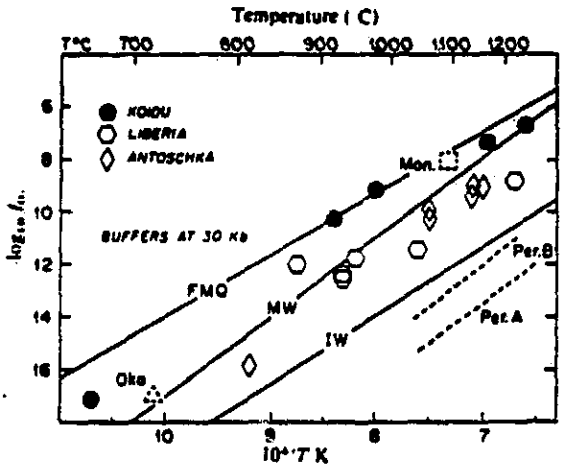

Fig. 4 Pressure corrected f_{O_2} buffers to 30 kbar, illustrating the effect of P on the relative f_{O_2} for the 1 bar data shown in Fig. 3. No correction has been applied to the mineral data.

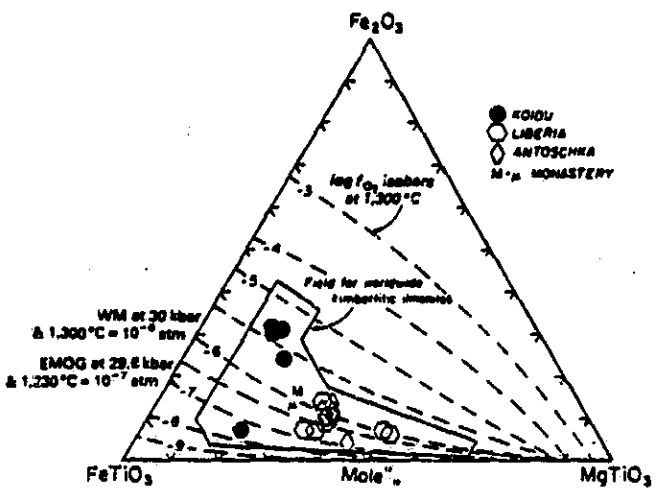

Fig. 5 Ilmenite compositions from West Africa (see legend to Fig. 2) plotted as a function of Fe_2O_3 (haematite), $FeTiO_3$ (ilmenite) and $MgTiO_3$ (geikielite). M and μ refer to an ilmenite starting composition, and to an experimentally equilibrated composition, respectively from the Monastery kimberlite[20]. The generalized field for kimberlitic ilmenites worldwide are from a compilation of data cited in refs 23, 38, 39. Oxygen fugacity isobars are from ref. 31; WM, wüstite–magnetite[34] and EMOG (see text for explanation) is from ref. 16. There is a large solvus in the ternary extending from the Fe_2O_3–$MgTiO_3$ sideline towards $FeTiO_3$ which has been omitted for clarity. It is considered that the distribution of kimberlitic ilmenite compositions is influenced by this ternary solvus and by the f_{O_2} environment of formation[20].

Discussion

It has been argued[41] that the presence of graphite or carbon polymorphs, or the occurrences of CH_4 and CO in ocean floor and upper-mantle derived nodules mandates that the mantle be reduced. We consider that these assumptions are erroneous: (1) because the abundances of reduced carbon species are negligible, amounting in most cases to concentrations of ≈0.5 wt% in media that are dominantly $CO_2 + H_2O$ (ref. 2); (2) graphite is stable over an enormous range of f_{O_2} and temperature conditions[42]; (3) graphite or diamond formation is possible by either oxidation ($CH_4 \rightleftharpoons C + 2H_2$) or reduction ($CO_2 \rightleftharpoons C + O_2$), and diamond is in equilibrium with $CO_2 + CH_4 \rightleftharpoons 2C + 2H_2O$ (ref. 10), so that extremely reducing conditions are not necessarily a prerequisite to carbon precipitation; (4) whether carbon forms from a single (such as $CO \rightleftharpoons C + \frac{1}{2}O_2$) or a multiple series of reactions (such as $CO_2 \rightleftharpoons CO + C + \frac{1}{2}O_2$), in which CO is an intermediate product, typically cannot be determined and hence the conditions of f_{O_2} are indeterminant; (5) high-pressure equilibria in the system C–H–O show that CO is never a major C-bearing species in the vapour[10]; (6) methane, however, may be present in mantle conditions[10] although evidence to the contrary suggests that the equilibria are more appropriately defined by CO–CO_2 (refs 16, 17). In a broader context we note that carbon + magnetite are typical of chondritic meteorites and some classes of metamorphic rocks, and that these are relatively oxidized.

Degassing of the upper mantle has taken place with time and an inevitable consequence of degassing is that the redox state of the mantle must also have changed with the continuous loss of volatiles. The question is whether the mantle has become more reduced or more oxidized, or whether the condition is steady state. The latter assumption is that volatile loss through volcanism is offset by ocean floor subduction of hydrous materials. Present-day basaltic volcanism and the Cretaceous kimberlite and carbonatitic suites collectively imply mantle redox conditions between FMQ and WM. However, we offer two tantalizing and perhaps crucial pieces of data on the redox state of the early mantle. These are that Ni-poor metallic Fe has been identified as an inclusion in diamond[43] and that the ages of diamonds, regardless of the time of kimberlite intrusion are Archaean[44]. Considerably more data are required but we propose that the early mantle may well have been reduced (for example, ≤WM) and that some nodule suites brought to the surface in kimberlites and alkali basalts reflect this primitive condition: even though the bulk content of volatiles would have been much greater, the relative proportions of reduced gas species would also have been greater. With time, however, the mantle has become progressively oxidized, resulting perhaps largely from the preferred loss of hydrogen and carbon. Another important factor is that if the upper mantle is geochemically layered, that is with an upper depleted zone overlying a more fertile region[45], it is likely that the redox condition of each component will differ. Depleted zones result from extensive volcanism, so that the regional, stratigraphical and age of the mantle zone being sampled in nodules must be considered. In mature mantles underlying cratonic regions of the Earth, a mixed sampling of oxidized and reduced components such as those present in kimberlites will differ from more fertile mantles actively undergoing depletion. Thus, depleted and refractory upper portions of mature mantle are likely to be relatively reduced. Similarly high level but juvenile and fertile regions of the mantle, such as those underlying the ocean floors, are relatively enriched in volatile constituents and are, therefore, more oxidized. The plausible ranges of f_{O_2} are WM and FMQ, respectively.

The mantle (and crustal) f_{O_2} model that we propose is illustrated in Fig. 6. Five typical tectonic cross-sections are outlined

ORIGINAL
OF POOR QUALITY

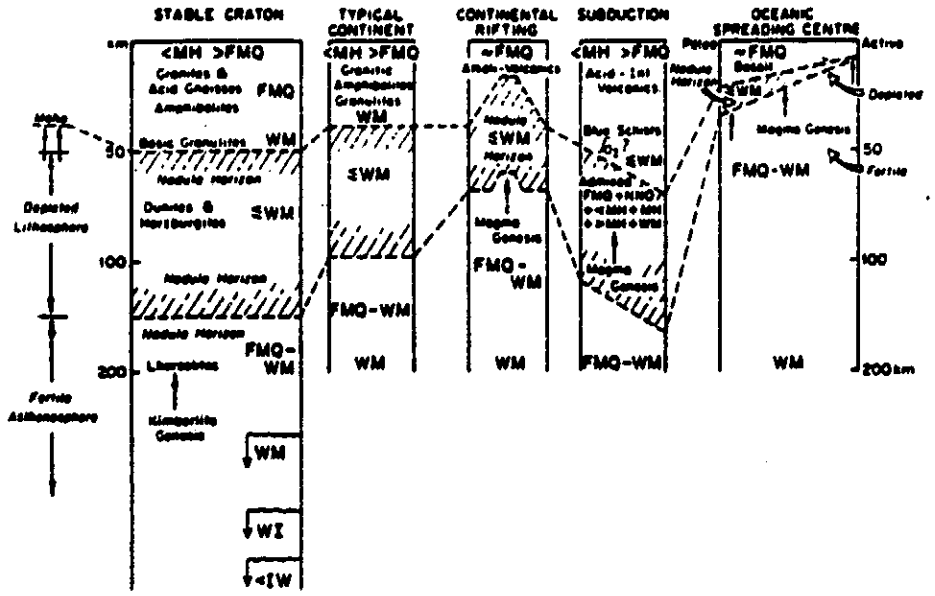

Fig. 6 Selected but typical cross-sections through the crust and upper mantle illustrating the distribution of rock types and profiles of oxygen fugacities. The highest f_{O_2} is represented by conditions less than magnetite–haematite (MH) equilibria. With increasing reduction the equilibria are NNO (Ni–NiO), FMQ (fayalite–magnetite–quartz), WM (wüstite–magnetite), and IW (iron–wüstite). The perched and depleted lithospheric layer results from sustained volcanism and varies in thickness as a function of mantle maturity and tectonic setting. Nodules from the depleted layer arise from craton, rift, and palaeo-spreading environments. Nodules from the fertile asthenosphere are most common in kimberlites but are also present in smaller concentrations in continental rift settings, and are only rarely encountered in palaeo-spreading terrains. This distribution is related to the depth of magma generation which is illustrated. In the text we conclude that the reduced state of the mantle that is inferred by some[13,14,46] results from selective sampling of depleted lithospheres. The lower portion of the upper mantle, in the fertile asthenospheres is oxidized and conditions are at FMQ ranging down to WM, to WI, and to iron at the lower mantle–outer core interface.

and the oxygen fugacities we have designated are from data presented here and cited earlier[2,15–17,26,32–35,40]. For the uppermost regions of each cross-section, oxygen fugacities range from below magnetite–haematite (MH) to FMQ, and representative examples are cratonic crust to ocean floor basalts, respectively. Oxygen fugacities decrease within the crust and we propose that a redox discontinuity is present at the Moho, transforming from FMQ to WM. Lower crustal granulites are most typically feldspathic, with almandine-rich garnet and Na–Fe^{3+}-bearing clinopyroxene; hydrous minerals, such as mica and amphibole may also be present. Hence these rocks are more oxidized than the underlying and depleted dunites and harzburgites. Although we suggest that the depleted lithosphere is at WM, it could conceivably be lower than WM but not much less, because spinels in these rocks are iron(III)-bearing[36]. The fertile asthenosphere, below the depleted lithosphere, signals a return to more oxidizing conditions (between FMQ and WM), represented by lherzolites and the genesis of highly volatile kimberlites and carbonatites. With increasing depth the redox state is WM, followed by WI and in the lower mantle–outer core boundary by iron. This model is applicable to four of the five cross-sections (Fig. 6), with the sub-Moho region of the subduction profile being more complex, resulting from admixtures of various redox components. Volcanism arising from these zones are mafic but also acid-intermediate in composition and are more highly oxidized than basalts at spreading axes or undersaturated volcanics in continental rift systems. We draw attention to two final points: (1) the depleted lithosphere varies enormously in thickness; and (2) only three tectonic settings give rise to mantle nodule suites: cratonic, continental rifts, and palaeo-spreading centres. The common factor is that sustained basaltic volcanism has produced a depleted lithospheric mantle horizon. Magma genesis in cratonic settings is usually at depths >150 km, and hence both fertile lherzolites and depleted dunites and harzburgites are entrained on eruption. On the other hand, in alkali-rift environments, magmas are generated at much higher levels and the opportunity for sampling fertile lherzolites is diminished. Hence, these volcanics most commonly contain a depleted and refractory nodule suite. Melting takes place in the redox zone of WM–FMQ and the resulting volcanics are FMQ (Fig. 6), similar to those of kimberlites and carbonatites (Fig. 3). Oxygen fugacity assessments, therefore, which are based on mantle-derived suites will depend on whether the nodules arise from depleted lithospheric mantle or from the fertile asthenosphere. Herein may lie the source of the disparity reported in mantle redox conditions.

Arculus and Delano[46] have presented comprehensive and convincing arguments for the oxygen fugacity for the early Earth that includes core formation and the origin of the atmosphere. We are in general agreement with most aspects of their model but we differ in interpretation. They conclude that the mantle is buffered by IW and that the observed state of effusive volcanism at FMQ results from oxidation during upward migration of magma. The premise for IW is based on data derived exclusively from the electrolytic cell technique, and an explanation to reconcile these low f_{O_2} values is auto-reduction from particulate graphite[47], fluid inclusions comprising reduced carbon species (for example, CH_4 or CO), or some property related to thermal relaxation of high-pressure minerals when heated to elevated temperatures at 1 atm. However, the most probable reason is that the data are not an artefact of the method used but rather that the peridotites they measured (Fig. 3) are all highly depleted continental rift nodules. Their model is, therefore, based only on the sandwiched and depleted lithosphere layer between the Moho and the fertile asthenosphere. They have not considered the latter.

Iron(III) and (II) equilibria in natural silicate liquids[48], and the pressure dependency of oxygen fugacity in magmas, show that f_{O_2} increases with increasing P (as in Fig. 4) and decreasing silica activity[49], which implies that the f_{O_2} of magmas (specifically mafic) at depth is greater than that at the surface, assuming isochemical ascent. The situation is clearly not this simple based on the speciation of iron (Fe^{2+}/Fe^{3+}), and iron–oxygen coordination in silicate melts as functions of P, T, f_{O_2} and bulk composition[50,51]. In alkali-rich systems (such as $NaAlSi_2O_6$–$NaFe^{3+}Si_2O_6$, or Na_2O–$Fe^{2+}O$–SiO_2), the ratio of Fe^{3+}/total iron decreases systematically from 1 to 10 kbar, plateaus between 10 and 20 kbar, and increases again from 20 to 30 kbar. Taken in a broader context, and recognizing that the experimental compositions are not directly applicable, it is nonetheless noteworthy, that the parabolic behaviour of Fe^{3+} as a function of P is consistent with the reduced state at low pressures determined by Arculus and Delano[46], and supports the data we present at higher pressures in kimberlites. The interval between 10 and 20 kbar is relatively reduced and corresponds approximately to that horizon within the litho-

sphere that we propose is similarly depleted in volatiles (Fig. 6), and hence, is more reduced.

Conclusions

Upper-mantle derived ilmenite nodule suites from kimberlites in West Africa are moderately oxidized and lie within redox states consistent with the determinations obtained on other nodule suites in kimberlites by thermodynamic and intrinsic f_{O_2} methods. These data contrast with lower pressure nodule suites in peridotites from alkali basalts which yield highly reduced values. A single all-encompassing redox state for the mantle cannot be uniquely inferred. Oxidation and reduction of the Earth's upper mantle has evolved with time, and an expression of this evolution is provided by the relative thicknesses of redox layers ranging from those in cratonic regimes to those at active oceanic spreading centres (Fig. 6). Crustal setting and tectonic style, along with nodules and volcanism provide the important clues to mantle redox conditions. Mantle source regions for all but subduction-related volcanism is WM–FMQ. Subducted terrains are more oxidized and lie between NNO (Ni–NiO) and MH. A knowledge of the stratigraphical position that these samples represent is fundamental to resolving the redox state of the upper mantle. The issue of mantle fugacities will not be settled until more precise data are available permitting specific sample horizons to be definitively located. Cretaceous kimberlites and carbonatites were unquestionably generated in an oxidized upper mantle below a depleted lithosphere. However, whether extreme depletion of such a zone could have led to IW[46] remains uncertain and problematic. A perched reduced zone appears probable in our model but an IW condition for the entire upper mantle appears unlikely.

This research was supported by the NSF grants EAR78-02539 and EAR78-02541 and in part by NASA contract NAS-5-26414. We thank BP Minerals—Sierra Leone Selection Trust—and the Ministries of Mines in Guinea and Liberia for support and access to the diamond fields. The manuscript was constructively reviewed by R. Arculus who with others, and independently, has reached a similar conclusion to the model we propose in this article.

Received 17 December 1982; accepted 3 March 1983.

1. Ringwood, A. E. *The Origin of the Earth and Moon* (Springer, New York, 1979).
2. Basaltic Volcanism Study Project *Basaltic Volcanism on the Terrestrial Planets* (Pergamon, New York, 1981).
3. Anderson, A. T. *Rev. Geophys. Space Phys.* **13**, 37–55 (1975).
4. Naughton, J. J., Heald, E. F. & Barnes, I. L. *J. geophys. Res.* **68**, 539–544 (1963).
5. Delaney, J. R., Muenow, D. W. & Graham, D. G. *Geochim. cosmochim. Acta* **42**, 581–594 (1978).
6. Moore, J. G. & Schilling, J. G. *Contr. Miner. Petrol.* **41**, 105–118 (1973).
7. Muenow, D. W., Liu, N. W. K., Garcia, M. O. & Saunders, A. D. *Earth planet. Sci. Lett.* **47**, 272–278 (1980).
8. Naldrett, A. J. & Duke, J. M. *Science* **208**, 1417–1424 (1980).
9. Haggerty, S. E. & Tompkins, L. A. *EOS* **63**, 463 (1982).
10. Deines, P. *Geochim. cosmochim. Acta* **44**, 943–961 (1980).
11. Haggerty, S. E. *Geophys. Res. Lett.* **5**, 105–108 (1978).
12. Wasilewski, P. J., Thomas, H. H. & Mayhew, M. A. *Geophys. Res. Lett.* **6**, 541–544 (1979).
13. Arculus, R. J. & Delano, J. W. *Geochim. cosmochim. Acta* **45**, 899–913 (1981).
14. Sato, M. *Geophys. Res. Lett.* **5**, 447–449 (1978).
15. Haggerty, S. E. *Geophys. Res. Lett.* **5**, 443–446 (1978).
16. Eggler, D. H. & Baker, D. R. *High Press. Res. Appl. Geophys.* 12, 237–250 (1982).
17. Eggler, D. H. *EOS* **63**, 450 (1982).
18. Boddington, A. F. & Lindsley, D. H. *J. Petrol.* **5**, 310–357 (1964).
19. Tompkins, L. A. & Haggerty, S. E. *Terra Cognita* **2**, 210–211 (1982).
20. Haggerty, S. E. & Tompkins, L. A. *Terra Cognita* **2**, 218–219 (1982).
21. Dawson, J. B. *Kimberlites and their Xenoliths* (Springer, New York, 1980).
22. Meyer, H. O. A. & Svisero, D. P. *Phys. Chem. Earth* **9**, 785–796 (1975).
23. Sobolev, N. V. *Deep-seated Inclusions in Kimberlites and The Problems of the Composition of The Upper Mantle* (American Geophysical Union, Washington DC, 1977).
24. Green, D. H. & Sobolev, N. V. *Contr. Miner. Petrol.* **50**, 217–229 (1975).
25. Wyatt, B. A. *Contr. Miner. Petrol.* **66**, 1–9 (1977).
26. Haggerty, S. E., Hardie, R. B. & McMahon, B. M. *The Mantle Sample: Inclusions in Kimberlites and Other Volcanics* (American Geophysical Union, Washington DC, 1979).
27. Bence, A. E. & Albee, A. L. *J. Geol.* **76**, 382–403 (1968).
28. Albee, A. L. & Ray, L. *Analyt. Chem.* **42**, 1408–1414 (1970).
29. Spencer, K. L. & Lindsley, D. H. *Am. Miner.* **66**, 1189–1201 (1981).
30. Lindsley, D. H. & Spencer, K. *J. EOS* **63**, 471 (1982).
31. Woermann, E., Hirschberg, A. & Lamprecht, A. *Fortschr. Miner.* **47**, 79–80 (1969).
32. Arculus, R. J., Dawson, J. B., Mitchell, R. H. & Gust, D. A. *Terra Cognita* **2**, 228 (1982).
33. Ulmer, G. C., Rosenhauer, M., Woermann, E., Ginder, J. & Drory-Wolff, A. *Am. Miner.* **61**, 653–660 (1976).
34. Friel, J. J. & Ulmer, G. C. *Am. Miner.* **59**, 314–318 (1974).
35. McMahon, B. M., Haggerty, S. E. & Bence, R. B. *Kimberlite. Symp. II* (Cambridge University Press, 1979).
36. Sato, M. *Geol. Soc. Am. Mem.* **135**, 289–307 (1972).
37. Sato, M. *Am. Miner.* **55**, 1424–1437 (1970).
38. Haggerty, S. E. *Reviews in Mineralogy: Oxide Minerals* (Mineralogical Society of America, Washington DC, 1976).
39. Mitchell, R. H. *J. Geol.* **81**, 301–311 (1973).
40. O'Neill, H. St. C., Ortez, N., Arculus, R. J., Wall, V. J. & Green, D. H. *Terra Cognita* **2**, 228 (1982).
41. Mathez, E. A. & Delaney, J. R. *Earth planet. Sci. Lett.* **56**, 217–232 (1981).
42. Deines, P., Nafziger, R. H., Ulmer, G. C. & Woermann, E. *Temperature-Oxygen Fugacity Tables for Selected Gas Mixtures in the System C–H–O at One Atmosphere Total Pressure* (Pennsylvania State University, 1974).
43. Sobolev, N. V., Efimova, E. S. & Pospelova, L. N. *Dokl. Akad. Nauk SSR* **12**, 25–29 (1981).
44. Kramers, J. D. *Earth planet. Sci. Lett.* **42**, 58–70 (1979).
45. Nixon, P. H., Rogers, N. W., Gibson, I. L. & Grey, A. *A. Rev. Earth planet. Sci.* **9**, 285–309 (1981).
46. Arculus, R. J. & Delano, J. W. *Nature* **288**, 72–74 (1980).
47. Sato, M. & Valenza, M. *Am. J. Sci.* **280A**, 134–158 (1980).
48. Sack, R. O., Carmichael, I. S. E., Rivers, M. & Ghiorso, M. S. *Contr. Miner. Petrol.* **75**, 369–376 (1980).
49. Mo, X., Carmichael, I. S. E., Rivers, M. & Stebbins, *J. Miner. Mag.* **45**, 237–245 (1982).
50. Mysen, B. O. & Virgo, D. *Am. J. Sci.* **278**, 1307–1322 (1978).
51. Mysen, B. O., Danckwerth, P. & Virgo, D. *A. Rep. Geophys. Lab., Carnegie Inst. Yb.* **81**, 357–360 (1982).
52. Huebner, J. S. & Sato, M. *Am. Miner.* **55**, 934–952 (1970).
53. Chou, I-M. *Am. Miner.* **63**, 690–703 (1978).
54. Eugster, H. P. & Wones, D. R. *J. Petrol.* **3**, 82–125 (1962).

Structure of mouse kallikrein gene family suggests a role in specific processing of biologically active peptides

Anthony J. Mason*, Bronwyn A. Evans*, David R. Cox†, John Shine* & Robert I. Richards*

* Centre for Recombinant DNA Research and Genetics Department, Research School of Biological Sciences, Australian National University, PO Box 475, Canberra 2601, Australia

† Department of Pediatrics, University of California, San Francisco, California 94143, USA

The glandular kallikrein gene family comprises 25–30 highly homologous genes that encode specific proteases involved in the processing of biologically active peptides. In the mouse all the members of this family are closely linked on chromosome 7. The 9.5-kilobase nucleotide sequence of a mouse genomic clone contains one complete kallikrein gene (mGK-1), which is expressed in the male mouse submaxillary gland, and the 3′ end of another (mGK-2). Differences in the coding potential of these genes and the amino acid sequences of other known kallikreins seem to be functionally related to the substrate specificity of the different enzymes.

APPENDIX 2

MAGNETIC SPINELS AND RELATED PHASES FROM MANTLE-DERIVED KIMBERLITES: ANALYTICAL DATA

Table 1 KIMBERLITIC GROUNDMASS OXIDES

KD-80-17-DZA-B

	1	2	3	4	5	6
SiO_2	0.00	0.00	0.00	0.00	0.00	0.00
TiO_2	0.12	7.18	1.93	25.46	21.84	21.51
CaO	0.05	0.20	0.12	0.50	0.57	0.13
Al_2O_3	9.38	3.73	7.95	4.81	3.23	0.68
Cr_2O_3	58.32	42.62	53.58	1.47	0.38	4.18
Fe_2O_3	5.18	12.73	8.62	18.23	24.68	22.46
FeO	12.09	21.37	15.43	33.94	39.57	48.50
MgO	13.48	10.66	12.37	12.81	6.46	0.00
MnO	0.44	0.50	0.53	0.52	0.92	2.98
Nb_2O_3	0.01	0.00	0.00	0.03	0.10	0.32
ZrO	0.00	0.00	0.00	0.00	0.00	0.00
NiO	0.11	0.28	0.15	0.17	0.28	0.17
Total	99.18	99.27	100.68	97.94	98.03	100.93

CATIONS TO 32 OXYGENS

Si	0.000	0.000	0.000	0.000	0.000	0.000
Ti	0.024	1.477	0.380	5.201	4.721	4.812
Ca	0.015	0.059	0.033	0.145	0.175	0.040
Al	2.887	1.203	2.454	1.542	1.094	0.238
Cr	12.043	9.222	11.087	0.317	0.086	0.983
Fe^{3+}	1.019	2.621	1.698	3.728	5.340	5.028
Fe^{2+}	2.641	4.891	3.377	7.715	9.516	12.066
Mg	5.249	4.350	4.824	5.190	2.767	0.000
Mn	0.097	0.116	0.116	0.121	0.223	0.750
Nb	0.001	0.000	0.000	0.004	0.013	0.043
Zr	0.000	0.000	0.000	0.000	0.000	0.000
Ni	0.024	0.062	0.031	0.038	0.065	0.040
Total	24.000	24.001	24.000	24.001	24.000	24.000

Table 2 Koidu kimberlitic ilmenites.

	KD-81-DP-1A						
	Groundmass ilmenites						
TiO_2	47.54	49.13	49.86	51.33	53.54	52.31	50.48
ZrO_2	0.25	0.25	0.11	0.10	0.11	0.15	0.61
Al_2O_3	0.00	0.00	0.00	0.00	0.04	0.09	0.00
Cr_2O_3	0.33	0.23	0.13	0.32	0.23	0.19	0.24
Fe_2O_3	6.65	5.08	5.50	5.41	3.14	4.12	3.71
FeO	33.43	34.67	33.25	33.00	28.16	29.27	34.33
MgO	0.24	0.60	1.33	4.44	9.17	7.14	4.11
MnO	9.72	9.03	9.46	5.64	3.87	4.98	5.61
NiO	0.01	0.01	0.01	0.02	0.07	0.07	0.00
Nb_2O_5	0.77	0.55	0.30	0.41	0.26	0.00	1.48
Total	98.94	99.55	99.95	100.67	98.59	98.32	100.57
	CATIONS TO 3 OXYGENS						
Ti	0.916	0.937	0.940	0.939	0.963	0.957	0.932
Zr	0.003	0.003	0.001	0.001	0.001	0.002	0.007
Al	0.000	0.000	0.000	0.000	0.001	0.002	0.000
Cr	0.007	0.005	0.003	0.006	0.004	0.004	0.005
Fe^{3+}	0.128	0.097	0.104	0.099	0.057	0.075	0.069
Fe^{2+}	0.717	0.735	0.697	0.672	0.564	0.596	0.705
Mg	0.009	0.023	0.050	0.161	0.327	0.259	0.150
Mn	0.211	0.194	0.201	0.116	0.078	0.103	0.117
Ni	0.000	0.000	0.000	0.000	0.001	0.001	0.000
Nb	0.009	0.006	0.003	0.005	0.003	0.000	0.016
Total	2.000	2.000	1.999	1.999	1.999	1.999	2.001
Mole%							
Hem	6.39	4.85	5.20	4.96	2.86	3.77	3.43
Ilm	71.63	73.46	69.70	67.30	56.54	59.87	70.04
Geik	0.90	2.30	5.00	16.12	32.78	26.02	14.90
Pyroph	21.08	19.39	20.10	11.62	7.82	10.35	11.62

Each column represents a single analysis.
Hem=hematite; Ilm=ilmenite; Geik=geikielite; Pyroph=pyrophanite.

Table 2 Koidu kimberlitic oxides.

	KD-81-DP-1A						
	Groundmass ilmenites		Groundmass spinels				
			Core	Core	Mantle	Atoll	Core
TiO_2	49.24	50.39	5.59	5.86	14.49	1.43	5.17
ZrO_2	0.15	0.14	0.06	0.11	0.05	0.35	0.07
Al_2O_3	0.00	0.00	6.78	6.48	3.12	0.01	8.38
Cr_2O_3	0.12	0.20	46.44	46.98	16.88	0.27	45.55
Fe_2O_3	4.21	3.70	8.92	9.53	22.05	65.62	9.19
FeO	34.14	35.55	20.20	20.04	33.89	31.28	18.78
MgO	0.05	0.51	11.10	11.66	5.80	0.57	12.01
MnO	10.99	9.45	0.61	0.66	1.76	0.35	0.48
NiO	0.02	0.02	0.29	0.26	0.20	0.04	0.29
Nb_2O_5	0.94	0.62	0.00	0.00	0.00	0.03	0.00
Total	99.90	100.58	99.99	101.58	98.24	99.95	99.92
	CATIONS TO 3 OXGYENS		CATIONS TO 32 OXYGENS				
Ti	0.940	0.951	1.124	1.158	3.144	0.329	1.025
Zr	0.002	0.002	0.008	0.014	0.007	0.052	0.009
Al	0.000	0.000	2.135	2.008	1.060	0.004	2.606
Cr	0.002	0.004	9.808	9.761	3.851	0.065	9.502
Fe^{3+}	0.080	0.070	1.794	1.886	4.788	15.154	1.824
Fe^{2+}	0.725	0.746	4.512	4.405	8.179	8.028	4.144
Mg	0.002	0.019	4.418	4.565	2.495	0.262	4.722
Mn	0.236	0.201	0.138	0.146	0.430	0.090	0.107
Ni	0.000	0.000	0.063	0.055	0.047	0.010	0.061
Nb	0.011	0.007	0.000	0.000	0.000	0.005	0.000
Total	1.998	2.000	24.000	23.998	24.001	23.999	24.000
Mole%							
Hem	3.99	3.50					
Ilm	72.28	74.53					
Geik	0.20	1.90					
Pyroph	23.53	20.08					

Each column represents a single analysis.
Hem=hematite; Ilm=ilmenite; Geik=geikielite; Pyroph=pyrophanite.

Table 2 Koidu kimberlitic spinels.

KD-61-DP-1A

	Groundmass spinels						
	Center	Edge	Atoll	Center -	2.5μ -	2.5μ-	2.5μ
TiO_2	5.36	5.97	2.24	5.59	5.37	5.97	7.26
ZrO_2	0.00	0.03	0.16	0.00	0.00	0.05	0.03
Al_2O_3	6.33	4.41	0.01	6.79	5.48	4.10	3.68
Cr_2O_3	48.83	48.49	0.60	46.48	48.04	46.68	41.77
Fe_2O_3	7.98	9.23	64.45	8.25	8.34	10.20	13.31
FeO	20.23	21.42	31.58	20.15	20.44	21.84	22.48
MgO	11.17	10.53	0.78	11.09	10.57	9.94	10.17
MnO	0.52	0.62	0.46	0.44	0.59	0.67	0.75
NiO	0.10	0.12	0.17	0.16	0.09	0.11	0.05
Nb_2O_5	0.00	0.00	0.05	0.00	0.00	0.00	0.00
Total	100.52	100.82	100.50	98.95	98.92	99.56	99.50
	CATIONS TO 32 OXYGENS						
Ti	1.071	1.207	0.513	1.132	1.098	1.229	1.497
Zr	0.000	0.003	0.023	0.000	0.001	0.007	0.003
Al	1.987	1.398	0.004	2.157	1.759	1.322	1.191
Cr	10.273	10.313	0.144	9.906	10.336	10.103	9.060
Fe^{3+}	1.598	1.869	14.757	1.673	1.708	2.101	2.748
Fe^{2+}	4.503	4.820	8.036	4.543	353	5.001	5.157
Mg	4.430	4.222	0.355	4.454	4.289	4.057	4.158
Mn	0.117	0.142	0.119	0.101	0.136	0.155	0.175
Ni	0.021	0.026	0.040	0.035	0.020	0.023	0.012
Nb	0.000	0.000	0.007	0.000	0.000	0.000	0.000
Total	24.000	24.000	23.998	24.001	24.000	23.998	24.001

Each column represents a single analysis.

Table 2 Koidu kimberlitic spinels

	KD-81-DP-1A						
	Groundmass spinels						
	2.5μ -	2.5μ -	2.5μ -	2.5μ -	Edge	Center -	2.5μ
TiO_2	13.58	1.73	3.09	2.96	1.12	5.25	5.41
ZrO_2	0.20	0.18	0.05	0.19	0.04	0.00	0.03
Al_2O_3	2.86	0.09	0.02	0.01	0.06	8.32	8.40
Cr_2O_3	18.01	1.07	0.39	0.36	0.29	45.67	45.48
Fe_2O_3	25.84	65.06	64.40	64.58	66.85	8.58	8.13
FeO	27.62	31.17	27.57	27.80	30.66	19.47	19.85
MgO	10.26	0.76	3.00	2.86	0.71	11.59	11.44
MnO	0.74	0.51	1.73	1.72	0.36	0.46	0.39
NiO	0.15	0.12	0.14	0.14	0.13	0.16	0.19
Nb_2O_5	0.00	0.00	0.00	0.00	0.06	0.00	0.00
Total	99.26	100.69	100.39	100.62	100.28	99.50	99.32
	CATIONS TO 32 OXYGENS						
Ti	2.833	0.395	0.695	0.664	0.257	1.048	1.082
Zr	0.027	0.026	0.008	0.028	0.006	0.000	0.003
Al	0.935	0.032	0.006	0.005	0.021	2.604	2.634
Cr	3.950	0.257	0.093	0.086	0.071	9.587	9.569
Fe^{3+}	5.396	14.869	14.496	14.525	15.359	1.714	1.627
Fe^{2+}	6.410	7.917	6.896	6.950	7.829	4.324	4.418
Mg	4.242	0.344	1.336	1.273	0.324	4.586	4.539
Mn	0.174	0.130	0.437	0.437	0.094	0.104	0.088
Ni	0.035	0.029	0.034	0.033	0.032	0.034	0.040
Nb	0.000	0.000	0.000	0.000	0.008	0.000	0.000
Total	24.002	23.999	24.001	24.001	24.001	24.001	24.000

Each column represents a single analysis.

Table 2 Koidu kimberlitic spinels

KD-81-DP-1A							
Groundmass spinels							
	2.5 - Edge		Center	Mantle1	Mantle2	Mantle2	Atoll
TiO_2	5.21	6.15	7.13	7.68	16.92	12.68	3.08
ZrO_2	0.08	0.07	0.00	0.09	0.15	0.17	0.08
Al_2O_3	7.77	3.93	3.68	3.84	2.70	3.11	0.13
Cr_2O_3	45.48	46.10	45.45	43.41	9.76	19.62	0.78
Fe_2O_3	8.58	10.11	11.21	12.46	29.13	25.50	63.06
FeO	19.23	21.34	21.95	22.14	30.69	28.16	29.32
MgO	11.43	10.17	10.74	11.06	10.44	9.33	2.28
MnO	0.50	0.72	0.72	0.73	0.81	1.03	0.88
NiO	0.20	0.04	0.12	0.18	0.10	0.11	0.19
Nb_2O_5	0.00	0.00	0.00	0.01	0.00	0.00	0.00
Total	98.48	98.63	101.00	101.60	100.70	99.71	99.80
CATIONS TO 32 OXYGENS							
Ti	1.054	1.275	1.444	1.542	3.484	2.648	0.699
Zr	0.011	0.009	0.000	0.012	0.020	0.023	0.012
Al	2.462	1.277	1.167	1.209	0.873	1.018	0.045
Cr	9.671	10.056	9.674	9.172	2.113	4.309	0.186
Fe^{3+}	1.737	2.099	2.272	2.507	6.005	5.331	14.347
Fe^{2+}	4.326	4.925	4.941	4.948	7.031	6.543	7.412
Mg	4.582	4.183	4.311	4.406	4.263	3.861	1.030
Mn	0.113	0.168	0.165	0.165	0.189	0.243	0.224
Ni	0.044	0.008	0.026	0.038	0.021	0.024	0.045
Nb	0.000	0.000	0.000	0.001	0.000	0.000	0.000
Total	24.000	24.000	24.000	24.000	23.999	24.000	24.000

Each column represents a single analysis.

Table 3 Koidu kimberlitic groundmass ilmenites

	KD-01-DP-2B						
TiO_2	48.82	49.46	49.17	52.90	50.78	51.51	50.61
ZrO_2	0.08	0.13	0.16	0.21	0.32	0.11	0.01
Al_2O_3	0.00	0.00	0.00	0.02	0.02	0.02	0.03
Cr_2O_3	0.98	0.74	0.67	0.15	0.19	0.93	0.89
Fe_2O_3	3.29	5.24	2.78	3.44	1.79	0.78	2.23
FeO	40.74	39.50	40.31	28.90	40.59	39.43	41.01
MgO	1.57	2.39	2.16	8.71	2.76	3.64	2.13
MnO	1.72	1.20	1.53	3.66	1.35	1.58	1.12
NiO	0.00	0.11	0.04	0.07	0.09	0.08	0.08
Nb_2O_5	1.24	0.50	1.35	0.47	1.05	1.13	0.49
Total	98.44	99.27	98.17	98.53	98.94	99.21	98.60
	CATIONS TO 3 OXYGENS						
Ti	0.936	0.933	0.941	0.957	0.959	0.963	0.961
Zr	0.001	0.002	0.002	0.002	0.004	0.001	0.000
Al	0.000	0.000	0.000	0.000	0.000	0.001	0.001
Cr	0.020	0.015	0.013	0.003	0.004	0.018	0.018
Fe^{3+}	0.063	0.099	0.053	0.062	0.034	0.015	0.042
Fe^{2+}	0.869	0.829	0.859	0.582	0.853	0.820	0.866
Mg	0.060	0.089	0.082	0.312	0.103	0.135	0.080
Mn	0.037	0.025	0.033	0.075	0.029	0.033	0.024
Ni	0.000	0.002	0.001	0.001	0.002	0.002	0.002
Nb	0.014	0.006	0.016	0.005	0.012	0.013	0.006
Total	2.000	2.000	2.000	1.999	2.000	2.001	2.000
Mole%							
Hem	3.16	4.99	2.65	3.10	1.70	0.75	2.12
Ilm	87.12	83.53	85.86	58.20	85.13	82.37	87.39
Geik	6.02	8.97	8.20	31.20	10.28	13.56	8.07
Pyroph	3.71	2.52	3.30	7.50	2.89	3.31	2.42

Each column represents a single analysis.
Hem=hematite; Ilm=ilmenite; Geik=geikielite; Pyroph=pyrophanite.

Table 3 Koidu kimberlitic groundmass ilmenites.

	KD-81-DP-2B						
	Edge	Center	Edge	Edge	Center	Edge	Center
TiO_2	49.89	50.59	50.44	50.30	49.86	50.56	52.18
ZrO_2	0.11	0.11	0.08	0.19	0.15	0.13	0.00
Al_2O_3	0.00	0.00	0.00	0.00	0.00	0.00	0.02
Cr_2O_3	0.58	1.09	0.78	0.35	0.36	0.83	0.64
Fe_2O_3	1.92	2.09	3.02	1.10	1.77	2.91	1.41
FeO	40.93	40.74	41.42	41.96	41.69	41.13	41.64
MgO	1.82	2.54	1.96	1.94	2.04	2.02	2.40
MnO	1.65	1.13	1.06	1.54	1.42	1.09	1.03
NiO	0.23	0.07	0.05	0.10	0.07	0.03	0.07
Nb_2O_3	1.07	0.87	0.60	1.60	1.77	0.31	0.11
Total	98.20	99.23	99.41	99.08	99.13	99.01	99.50
	CATIONS TO 3 OXYGENS						
Ti	0.956	0.953	0.952	0.956	0.947	0.957	0.978
Zr	0.001	0.001	0.001	0.002	0.002	0.002	0.000
Al	0.000	0.000	0.000	0.000	0.000	0.000	0.001
Cr	0.012	0.022	0.016	0.007	0.007	0.016	0.013
Fe^{3+}	0.037	0.039	0.057	0.021	0.034	0.055	0.026
Fe^{2+}	0.872	0.854	0.870	0.887	0.881	0.866	0.869
Mg	0.069	0.095	0.074	0.073	0.077	0.076	0.089
Mn	0.036	0.024	0.022	0.033	0.030	0.023	0.022
Ni	0.005	0.001	0.001	0.002	0.001	0.001	0.001
Nb	0.012	0.010	0.007	0.018	0.020	0.003	0.001
Total	2.000	1.999	2.000	1.999	1.999	1.999	2.000
Mole%							
Hem	1.86	1.96	2.87	1.05	1.69	2.77	1.31
Ilm	87.59	86.05	87.48	88.39	87.66	87.25	87.51
Geik	6.93	9.57	7.44	7.27	7.66	7.66	8.96
Pyroph	3.62	2.42	2.21	3.29	2.99	2.32	2.22

Each column represents a single analysis.
Hem=hematite; Ilm=ilmenite; Geik=geikielite; Pyroph=pyrophanite.

Table 3 . Koidu kimberlitic groundmass ilmenites

	KD-81-DP-2B						
	Very Edge	Edge	Center	Edge	Very Edge	Center	Center
TiO_2	50.95	51.29	50.52	50.95	50.28	49.92	49.94
ZrO_2	0.04	0.03	0.18	0.19	0.11	0.09	0.08
Al_2O_3	0.00	0.00	0.00	0.00	0.00	0.00	0.00
Cr_2O_3	1.00	0.35	0.47	0.51	1.10	0.55	0.88
Fe_2O_3	3.15	2.55	1.47	2.69	3.21	2.50	2.62
FeO	41.12	39.93	40.31	40.98	41.39	41.14	40.52
MgO	2.28	3.25	3.15	2.58	1.95	2.04	2.24
MnO	1.15	1.24	1.14	1.04	0.97	1.16	1.12
NiO	0.08	0.09	0.09	0.07	0.10	0.06	0.07
Nb_2O_5	0.55	0.86	1.53	0.72	0.63	0.99	0.71
Total	100.32	99.59	98.86	99.73	99.74	98.45	98.18
	CATIONS TO 3 OXYGENS						
Ti	0.951	0.958	0.953	0.955	0.947	0.952	0.953
Zr	0.001	0.000	0.002	0.002	0.001	0.001	0.001
Al	0.000	0.000	0.000	0.000	0.000	0.000	0.000
Cr	0.020	0.007	0.009	0.010	0.022	0.011	0.018
Fe^{3+}	0.059	0.048	0.028	0.051	0.061	0.048	0.050
Fe^{2+}	0.854	0.830	0.846	0.855	0.867	0.873	0.860
Mg	0.084	0.120	0.118	0.096	0.073	0.077	0.085
Mn	0.024	0.026	0.024	0.022	0.021	0.025	0.024
Ni	0.002	0.002	0.002	0.001	0.002	0.001	0.001
Nb	0.006	0.010	0.017	0.008	0.007	0.011	0.008
Total	2.001	2.001	1.999	2.000	2.001	1.999	2.000
Mole%							
Hem	2.98	2.40	1.40	2.55	3.08	2.40	2.52
Ilm	86.13	83.00	84.43	85.63	87.44	87.39	86.52
Geik	8.47	12.00	11.78	9.61	7.36	7.71	8.55
Pyroph	2.42	2.60	2.40	2.20	2.12	2.50	2.41

Each column represents a single analysis.
Hem=hematite; Ilm=ilmenite; Geik=geikielite; Pyroph=pyrophanite.

Table 3 .Ke ..u kimberlitic groundmass oxides

	KD-81-DP-2B							
	Ilmenites				Spinels			
				Xen	Center	Edge	Center	Center
TiO_2	51.43	51.55	51.68	49.19	4.87	5.14	4.91	5.02
ZrO_2	0.02	0.11	0.20	0.24	0.11	0.10	0.21	0.13
Al_2O_3	0.09	0.02	0.02	0.45	8.61	7.56	5.38	8.82
Cr_2O_3	0.74	0.59	0.88	0.18	45.69	47.47	49.60	45.29
Fe_2O_3	1.70	0.78	1.42	13.26	8.42	8.34	8.95	8.96
FeO	41.52	42.76	42.05	27.69	18.97	19.03	19.21	18.86
MgO	2.20	2.09	2.32	9.33	11.69	11.94	11.48	11.96
MnO	1.48	1.17	1.17	0.23	0.46	0.52	0.66	0.59
NiO	0.08	0.01	0.00	0.02	0.20	0.13	0.16	0.27
Nb_2O_5	0.71	1.18	0.73	0.19	0.06	0.04	0.08	0.11
Total	99.97	100.26	100.47	100.78	99.08	100.27	100.64	100.01
	CATIONS TO 3 OXYGENS				CATIONS TO 32 OXYGENS			
Ti	0.963	0.965	0.963	0.869	0.974	1.020	0.985	0.994
Zr	0.000	0.001	0.002	0.003	0.014	0.013	0.027	0.017
Al	0.003	0.000	0.000	0.012	2.700	2.353	1.691	2.736
Cr	0.015	0.012	0.017	0.003	9.614	9.909	10.459	9.429
Fe^{3+}	0.032	0.015	0.026	0.234	1.686	1.657	1.796	1.775
Fe^{2+}	0.865	0.891	0.872	0.544	4.221	4.202	4.284	4.153
Mg	0.082	0.078	0.086	0.327	4.637	4.697	4.564	4.694
Mn	0.031	0.025	0.025	0.005	0.103	0.116	0.150	0.132
Ni	0.002	0.000	0.000	0.000	0.043	0.028	0.034	0.058
Nb	0.008	0.013	0.008	0.002	0.008	0.005	0.010	0.013
Total	2.001	2.000	1.999	1.999	24.000	24.000	24.000	24.001
Mole%								
Hem	1.61	0.75	1.31	11.78				
Ilm	87.02	88.97	87.55	54.78				
Geik	8.25	7.79	8.63	32.93				
Pyroph	3.12	2.50	2.51	0.50				

Each column represents a single analysis except for Xen. ilmenite. Xen=xenocrystic ilmenite (average of 4 analysis); Hem=hematite; Ilm=ilmenite; Geik=geikielite; Pyroph=pyrophanite.

Table 3 Koidu kimberlitic groundmass spinels

	KD-81-DP-2B						
	1	2	3	4	5	6	Mt.
TiO_2	4.81	5.28	4.93	5.11	5.41	4.95	0.09
ZrO_2	0.10	0.14	0.06	0.13	0.33	0.10	0.09
Al_2O_3	8.82	8.18	8.74	8.74	5.95	8.05	0.00
Cr_2O_3	46.76	46.57	46.36	45.83	47.56	47.18	0.05
Fe_2O_3	8.89	8.51	8.88	8.63	9.69	8.68	67.89
FeO	18.58	19.53	18.97	19.85	18.83	18.67	29.71
MgO	12.30	11.82	11.95	12.03	12.17	12.22	0.31
MnO	0.42	0.60	0.53	0.68	0.81	0.51	0.01
NiO	0.24	0.17	0.24	0.23	0.06	0.17	0.67
Nb_2O_5	0.04	0.06	0.02	0.08	0.13	0.11	0.05
Total	100.96	100.86	100.68	100.31	100.94	100.64	98.87
	CATIONS TO 32 OXYGENS						
Ti	0.941	1.040	0.969	1.009	1.075	0.976	0.020
Zr	0.013	0.018	0.008	0.016	0.042	0.013	0.013
Al	2.708	2.529	2.697	2.705	1.853	2.488	0.000
Cr	9.628	9.655	9.593	9.511	9.939	9.780	0.011
Fe^{3+}	1.743	1.680	1.749	1.705	1.927	1.713	15.901
Fe^{2+}	4.048	4.283	4.151	4.138	4.162	4.093	7.734
Mg	4.774	4.619	4.663	4.707	4.793	4.775	0.144
Mn	0.092	0.134	0.117	0.151	0.181	0.113	0.002
Ni	0.050	0.036	0.051	0.048	0.012	0.035	0.167
Nb	0.005	0.007	0.003	0.010	0.016	0.014	0.007
Total	24.002	24.001	24.001	24.000	24.000	24.000	23.999

Each column represents a single analysis, except Mt.
Mt=magnetite in serpentinized olivine (average of 3 analysis).

Table 4 Koidu kimberlitic groundmass ilmenites.

	KD-81-DP-3B					
	1	2	3	4	5	6
TiO_2	49.19	49.89	48.99	49.52	49.38	49.70
ZrO_2	0.14	0.10	0.09	0.06	0.06	0.07
Al_2O_3	0.01	0.02	0.00	0.00	0.00	0.00
Cr_2O_3	0.50	0.66	0.47	0.74	0.21	0.54
Fe_2O_3	3.06	3.07	4.70	3.13	2.27	3.16
FeO	40.14	40.57	39.72	40.78	40.04	39.82
MgO	2.25	1.89	2.62	1.99	0.32	2.47
MnO	1.69	1.61	0.94	1.39	5.19	1.98
NiO	0.08	0.10	0.07	0.07	0.03	0.07
Nb_2O_5	1.52	0.69	1.22	1.15	1.36	1.46
Total	98.58	98.60	98.82	98.83	98.86	99.27
	CATIONS TO 3 OXYGENS					
Ti	0.938	0.951	0.929	0.942	0.952	0.939
Zr	0.002	0.001	0.001	0.001	0.001	0.001
Al	0.000	0.001	0.000	0.000	0.000	0.000
Cr	0.010	0.013	0.009	0.015	0.004	0.011
Fe^{3+}	0.058	0.059	0.089	0.060	0.044	0.060
Fe^{2+}	0.851	0.860	0.838	0.863	0.858	0.837
Mg	0.085	0.071	0.099	0.075	0.012	0.093
Mn	0.036	0.034	0.020	0.030	0.113	0.042
Ni	0.002	0.002	0.001	0.001	0.001	0.001
Nb	0.017	0.008	0.014	0.013	0.016	0.017
Total	1.999	2.000	2.000	2.000	2.001	2.001
mole%						
Hem	5.63	5.76	8.51	5.84	4.28	5.81
Ilm	82.62	83.98	80.11	83.95	83.54	81.10
Geik	8.25	6.93	9.46	7.30	1.17	9.01
Pyroph	3.50	3.32	1.91	2.92	11.00	4.07

Each column represents a single analysis.
Hem=hematite; Ilm=ilmenite; Geik=geikielite; Pyroh=pyrophanite.

Table 4 Koidu kimberlitic xenocrystic ilmenites.

	KD-81-DP-3B						
	1	2	3	4	Center(5)	Edge(5)	Very Edge(5)
TiO_2	50.38	51.41	52.10	50.30	49.02	48.11	49.01
ZrO_2	0.17	0.17	0.14	0.23	0.10	0.01	0.12
Al_2O_3	0.32	0.23	0.17	0.24	0.39	0.31	0.23
Cr_2O_3	3.07	3.90	3.07	3.97	1.91	3.66	2.07
Fe_2O_3	10.53	9.37	9.88	13.18	14.74	16.82	16.45
FeO	18.58	19.80	17.67	16.78	18.91	16.62	16.31
MgO	14.77	14.56	16.02	15.62	14.03	14.61	15.30
MnO	0.60	0.65	0.82	0.68	0.61	0.56	0.68
NiO	0.05	0.15	0.05	0.11	0.07	0.16	0.04
Nb_2O_5	0.16	0.21	0.18	0.07	0.43	0.12	0.17
Total	98.63	100.45	100.10	101.18	100.21	100.98	100.38
	CATIONS TO 3 OXYGENS						
Ti	0.872	0.877	0.882	0.847	0.843	0.818	0.834
Zr	0.002	0.002	0.002	0.002	0.001	0.000	0.001
Al	0.009	0.006	0.004	0.006	0.010	0.008	0.006
Cr	0.056	0.070	0.055	0.070	0.035	0.066	0.037
Fe^{3+}	0.182	0.160	0.167	0.222	0.254	0.286	0.280
Fe^{2+}	0.358	0.376	0.333	0.314	0.362	0.314	0.309
Mg	0.507	0.492	0.538	0.522	0.478	0.493	0.516
Mn	0.012	0.012	0.016	0.013	0.012	0.011	0.013
Ni	0.001	0.003	0.001	0.002	0.001	0.003	0.001
Nb	0.002	0.002	0.002	0.001	0.004	0.001	0.002
Total	2.001	2.000	2.000	1.999	2.000	2.000	1.999
Mole%							
Hem	17.19	15.38	15.84	20.73	22.97	25.91	25.04
Ilm	33.81	36.15	31.59	29.32	32.73	28.44	27.64
Geik	47.88	47.31	51.04	48.74	43.22	44.66	46.15
Proph	1.13	1.15	1.52	1.21	1.08	1.00	1.16

Each column represents a single analysis.
Hem=hematite; Ilm=ilmenite; Geik=geikielite; Pyroph=pyrophanite.

Table 4. Koidu kimberlitic spinels.

	KD-81-DP-3B					
	Spinel Mantling ilm #5				Groundmass Spinel	
					Center	Edge
TiO_2	19.79	27.23	18.47	18.07	14.78	10.46
ZrO_2	0.05	0.17	0.11	0.03	0.00	0.31
Al_2O_3	3.26	1.56	3.06	3.27	3.32	7.13
Cr_2O_3	3.56	3.18	5.97	3.81	14.15	2.14
Fe_2O_3	31.78	16.13	28.61	29.05	27.57	42.54
FeO	28.51	42.31	30.65	39.80	29.43	29.58
MgO	13.60	8.52	10.95	4.78	9.82	7.87
MnO	1.04	1.28	0.92	1.25	0.91	0.55
NiO	0.13	0.22	0.10	0.12	0.15	0.20
Nb_2O_5	0.00	0.00	0.00	0.00	0.00	0.00
Total	101.72	100.60	98.84	100.18	100.13	100.78
	CATIONS TO 32 OXYGENS					
Ti	3.943	5.687	3.849	3.886	3.061	2.164
Zr	0.007	0.023	0.014	0.005	0.000	0.042
Al	1.017	0.509	1.000	1.103	1.078	2.313
Cr	0.746	0.698	1.309	0.861	3.082	0.466
Fe^{3+}	6.337	3.373	5.966	6.254	5.717	8.808
Fe^{2+}	6.319	9.831	7.102	9.521	6.784	6.808
Mg	5.372	3.528	4.523	2.039	4.033	3.228
Mn	0.232	0.301	0.215	0.304	0.212	0.128
Ni	0.027	0.050	0.023	0.027	0.032	0.043
Nb	0.000	0.000	0.000	0.000	0.000	0.000
Total	24.000	24.000	24.001	24.000	23.999	24.000

Each column represents a single analysis.

Table 4 Koidu kimberlitic spinels.

	KD-81-DP-3E				
	Groundmass spinels				
	Core	Core	Mantle	Core	Mantle
TiO_2	6.38	6.11	18.26	4.43	14.69
ZrO_2	0.13	0.15	0.15	0.16	0.11
Al_2O_3	4.23	5.82	3.10	7.62	3.73
Cr_2O_3	45.32	45.90	28.38	46.93	20.58
Fe_2O_3	10.62	10.40	8.81	8.92	22.51
FeO	20.67	20.67	28.68	19.61	27.11
MgO	10.85	11.36	12.88	11.00	11.83
MnO	0.74	0.59	0.93	0.39	0.71
NiO	0.06	0.12	0.06	0.13	0.15
Nb_2O_5	0.00	0.00	0.04	0.00	0.01
Total	99.00	101.12	101.29	99.19	101.43
	CATIONS TO 32 OXYGENS				
Ti	1.312	1.219	3.639	0.894	2.954
Zr	0.018	0.020	0.019	0.021	0.015
Al	1.363	1.819	0.968	2.411	1.177
Cr	9.795	9.628	5.946	9.958	4.352
Fe^{3+}	2.184	2.076	1.757	1.802	4.530
Fe^{2+}	4.726	4.588	6.357	4.401	6.063
Mg	4.419	4.491	5.089	4.398	4.714
Mn	0.172	0.134	0.208	0.089	0.161
Ni	0.013	0.026	0.012	0.027	0.033
Nb	0.000	0.000	0.005	0.000	0.001
Total	24.002	24.001	24.000	24.001	24.000

Each column represents a single analysis.

Table 5 Kofdu xenocrystic ilmenite

	KD-81-DZB-A2						
	1	2	3	4	5	6	Average
TiO_2	48.22	48.40	48.57	48.49	48.86	39.01	46.92
ZrO_2	0.49	0.60	0.62	0.45	0.58	0.34	0.51
Al_2O_3	0.34	0.02	0.01	0.03	0.01	0.27	0.11
Cr_2O_3	0.41	0.85	0.52	0.54	0.43	1.19	0.66
Fe_2O_3	11.61	10.55	12.56	13.13	12.59	29.58	15.06
FeO	33.36	33.70	27.52	30.01	27.47	21.49	28.89
MgO	5.81	5.75	9.21	7.56	9.58	7.77	7.63
MnO	0.20	0.25	0.41	0.33	0.34	0.39	0.32
NiO	0.00	0.04	0.00	0.05	0.00	0.00	0.01
Nb_2O_5	0.26	0.35	0.30	0.01	0.57	0.44	0.32
Total	100.70	100.51	99.72	100.60	100.43	100.48	100.43
	CATIONS TO 3 OXYGENS						
Ti	0.876	0.882	0.870	0.871	0.868	0.706	0.845
Zr	0.006	0.007	0.007	0.005	0.007	0.004	0.006
Al	0.010	0.001	0.000	0.001	0.000	0.008	0.003
Cr	0.008	0.016	0.010	0.010	0.008	0.023	0.012
Fe^{3+}	0.211	0.193	0.225	0.236	0.224	0.536	0.271
Fe^{2+}	0.674	0.683	0.549	0.600	0.543	0.433	0.579
Mg	0.209	0.208	0.327	0.269	0.337	0.279	0.272
Mn	0.004	0.005	0.008	0.007	0.007	0.008	0.006
Ni	0.000	0.001	0.000	0.001	0.000	0.000	0.000
Nb	0.003	0.004	0.003	0.000	0.006	0.005	0.003
Total	2.001	2.000	1.999	2.000	2.000	2.002	1.997
Mole%							
Hem	19.22	17.72	20.29	21.22	20.16	42.68	24.02
Ilm	61.38	62.72	49.50	53.96	48.87	34.47	51.33
Geik	19.03	19.10	29.49	24.19	30.33	22.21	24.11
Pyroph	0.36	0.46	0.72	0.63	0.63	0.64	0.53

Each column represents a single analysis except for the average.
Hem=hematite; Ilm=ilmenite; Geik=geikielite; Pyroph=pyrophanite.

Table 5 Kofdu kimberlitic spinels

KD-81-DZB-A2

Lamellae spinels in xenocrystic ilmenite.

	1	2	3	4	5	6	7
TiO_2	21.58	28.67	31.92	31.33	32.39	16.91	18.73
ZrO_2	0.24	0.28	0.34	0.31	0.41	0.21	0.18
Al_2O_3	1.04	0.78	0.69	0.75	0.67	0.95	1.00
Cr_2O_3	2.16	1.96	2.34	2.07	2.14	2.27	2.20
Fe_2O_3	25.15	12.45	4.44	6.77	4.75	33.26	30.36
FeO	46.99	52.50	54.39	54.96	54.58	41.57	42.94
MgO	2.84	3.69	4.13	3.72	4.48	3.02	3.36
MnO	0.13	0.20	0.16	0.20	0.21	0.26	0.22
NiO	0.12	0.11	0.15	0.16	0.13	0.15	0.14
Nb_2O_5	0.08	0.22	0.35	0.36	0.31	0.00	0.00
Total	100.33	100.86	98.91	100.63	100.07	98.60	99.13
			CATIONS TO 32 OXYGENS				
Ti	4.750	6.210	7.006	6.788	7.012	3.796	4.164
Zr	0.035	0.040	0.049	0.044	0.057	0.030	0.026
Al	0.359	0.266	0.239	0.256	0.226	0.336	0.347
Cr	0.500	0.447	0.539	0.471	0.487	0.536	0.515
Fe^{3+}	5.541	2.700	0.975	1.468	1.030	7.475	6.757
Fe^{2+}	11.505	12.649	13.277	13.245	13.144	10.383	10.620
Mg	1.240	1.585	1.796	1.597	1.922	1.344	1.482
Mn	0.033	0.048	0.040	0.048	0.052	0.065	0.054
Ni	0.027	0.025	0.034	0.036	0.030	0.035	0.034
Nb	0.010	0.029	0.046	0.047	0.040	0.000	0.000
Total	24.000	23.999	24.001	24.000	24.000	24.000	23.999

Each column represents a single analysis.

Table 5 Koidu kimberlitic oxides

	KD-81-DZB-A2						
	Spinel lamellae (cont'd)		Mantling ilmenites on xenocrystic ilmenite				
	8	Average	1	2	3	4	5
TiO_2	20.90	25.27	49.13	47.88	48.20	49.96	44.83
ZrO_2	0.20	0.27	0.26	0.26	0.25	0.22	0.38
Al_2O_3	1.13	0.88	0.10	0.00	0.06	0.04	0.13
Cr_2O_3	2.27	2.18	2.54	0.22	3.11	1.59	3.22
Fe_2O_3	25.85	17.96	12.94	5.02	14.66	12.16	20.78
FeO	45.97	49.20	25.14	27.70	22.94	24.36	20.07
MgO	2.81	3.52	10.48	0.31	10.82	11.32	11.13
MnO	0.19	0.20	0.53	16.75	1.23	0.54	0.70
NiO	0.20	0.14	0.01	0.09	0.12	0.02	0.02
Nb_2O_5	0.03	0.17	0.05	1.96	0.09	0.06	0.11
Total	99.55	99.79	101.18	100.19	101.48	100.27	101.37
	CATIONS TO 32 OXYGENS		CATIONS TO 3 OXYGENS				
Ti	4.634	5.551	0.858	0.913	0.839	0.875	0.781
Zr	0.028	0.039	0.003	0.003	0.003	0.003	0.004
Al	0.394	0.302	0.003	0.000	0.002	0.001	0.004
Cr	0.529	0.503	0.047	0.004	0.057	0.029	0.059
Fe^{3+}	5.738	3.949	0.226	0.096	0.255	0.213	0.362
Fe^{2+}	11.340	12.021	0.489	0.588	0.444	0.474	0.389
Mg	1.236	1.531	0.363	0.012	0.373	0.393	0.385
Mn	0.047	0.049	0.010	0.360	0.024	0.011	0.014
Ni	0.048	0.034	0.000	0.002	0.002	0.000	0.000
Nb	0.005	0.022	0.000	0.022	0.001	0.001	0.001
Total	23.999	24.001	1.999	2.000	2.000	2.000	1.999
Mole%							
Hem			20.77	9.09	23.27	19.52	31.48
Ilm			44.94	55.68	40.51	43.45	33.83
Geik			33.36	1.14	34.03	36.02	33.48
Pyroph			0.92	34.09	2.19	1.01	1.22

Each column represents a single analysis, except for the average
Hem=hematite; Ilm=ilmenite; Geik=geikielite; Pyroph=pyrophanite.

Table 5 Koidu kimberlitic ilmenites

KD-81-DZB-A2

Mantling ilmenite on xenocrystic ilmenite (cont'd)

	6	7	8	9	10	11	Average
TiO_2	49.26	49.03	52.07	47.86	48.52	49.40	48.74
ZrO_2	0.18	0.28	0.36	0.41	0.16	0.56	0.30
Al_2O_3	0.11	0.11	0.05	0.08	0.08	0.07	0.08
Cr_2O_3	2.20	2.17	0.88	1.98	2.18	1.41	1.95
Fe_2O_3	13.87	13.70	10.83	15.08	14.81	13.24	13.50
FeO	24.00	22.64	21.66	22.55	21.11	24.82	23.27
MgO	11.12	11.24	13.58	10.49	12.32	10.81	10.38
MnO	0.50	1.50	0.95	2.00	0.59	0.55	2.37
NiO	0.07	0.04	0.01	0.06	0.04	0.10	0.05
Nb_2O_5	0.00	0.00	0.00	0.06	0.00	0.00	0.21
Total	101.31	100.71	100.59	100.57	99.81	100.96	100.85
			CATIONS TO 3 OXYGENS				
Ti	0.856	0.856	0.894	0.842	0.848	0.864	0.856
Zr	0.002	0.003	0.004	0.005	0.002	0.006	0.003
Al	0.003	0.003	0.001	0.002	0.002	0.002	0.002
Cr	0.040	0.040	0.016	0.037	0.040	0.026	0.036
Fe^{3+}	0.241	0.239	0.186	0.266	0.259	0.232	0.237
Fe^{2+}	0.464	0.440	0.418	0.441	0.410	0.483	0.454
Mg	0.383	0.389	0.462	0.366	0.427	0.375	0.361
Mn	0.010	0.030	0.018	0.040	0.012	0.011	0.047
Ni	0.001	0.001	0.000	0.001	0.001	0.002	0.001
Nb	0.000	0.000	0.000	0.001	0.000	0.000	0.002
Total	2.000	2.001	1.999	2.001	2.001	2.001	1.999
Mole%							
Hem	21.95	21.77	17.16	23.90	23.38	21.07	21.57
Ilm	42.26	40.07	38.56	39.62	37.00	43.87	41.31
Geik	34.88	35.43	42.62	32.88	38.54	34.06	32.85
Pyroph	0.91	2.73	1.66	3.59	1.08	1.00	4.28

Each column represents a single analysis, except for the average.
Hem=hematite; Ilm=ilmenite; Geik=geikielite; Pyroph=pyrophanite.

Table 5 Koidu kimberlitic ilmenites

	KD-81-DZB-A2				KD-81-DZB-B	
	Groundmass ilmenites					
	1	2	3	4	5	6
TiO_2	51.27	49.01	48.80	52.48	50.39	47.42
ZrO_2	1.03	0.72	0.85	0.34	0.55	0.69
Al_2O_3	0.00	0.00	0.00	0.00	0.01	0.10
Cr_2O_3	0.15	0.14	0.27	0.25	0.04	0.48
Fe_2O_3	7.50	11.50	12.94	9.54	6.75	11.03
FeO	16.94	21.15	22.43	18.21	21.36	24.01
MgO	16.77	12.73	11.78	15.00	10.61	10.74
MnO	2.81	2.40	2.21	4.05	7.45	2.07
NiO	0.00	0.00	0.08	0.00	0.02	0.00
Nb_2O_5	2.77	1.65	1.29	1.55	2.06	2.05
Total	99.24	99.30	100.65	101.42	99.24	98.59
	CATIONS TO 3 OXYGENS					
Ti	0.880	0.863	0.854	0.890	0.900	0.853
Zr	0.011	0.008	0.010	0.004	0.006	0.008
Al	0.000	0.000	0.000	0.000	0.000	0.003
Cr	0.003	0.003	0.005	0.004	0.001	0.009
Fe^{3+}	0.129	0.203	0.227	0.162	0.121	0.199
Fe^{2+}	0.323	0.414	0.437	0.343	0.424	0.481
Mg	0.571	0.444	0.409	0.504	0.376	0.383
Mn	0.054	0.048	0.044	0.077	0.150	0.042
Ni	0.000	0.000	0.002	0.000	0.000	0.000
Nb	0.029	0.017	0.014	0.016	0.022	0.022
Total	2.000	2.000	2.002	2.000	2.000	2.000
Mole%						
Hem	11.98	18.30	20.32	14.92	11.30	18.01
Ilm	29.99	37.33	39.12	31.58	39.59	43.53
Geik	53.02	40.04	36.62	46.41	35.11	34.66
Pyroph	5.01	4.33	3.94	7.09	14.01	3.80

Each column represents a single analysis.
Hem=hematite; Ilm=ilmenite; Geik=geikielite; Pyroph=pyrophanite.

Table 5 Koidu kimberlitic oxides.

KD-81-DZE-A2							
Mineral "H"							
	8	9	10	11	12	13	14
TiO_2	17.13	16.68	11.41	16.26	17.65	13.87	16.97
ZrO_2	0.20	0.30	0.18	0.35	0.20	0.26	0.43
Al_2O_3	1.79	1.64	2.44	2.13	1.60	1.88	1.90
Cr_2O_3	3.77	2.27	13.12	1.38	2.19	8.29	1.95
FeO	64.65	66.72	60.65	68.76	65.07	63.46	66.02
MgO	11.03	10.27	9.65	9.93	10.60	10.12	10.17
MnO	0.99	1.08	0.96	0.91	0.98	0.85	0.92
NiO	0.08	0.10	0.09	0.14	0.13	0.12	0.05
Nb_2O_5	0.00	0.00	0.00	0.00	0.00	0.00	0.00
Total	99.64	99.06	98.50	99.86	98.42	98.85	98.41
CATIONS TO 7 OXYGENS							
Ti	0.859	0.852	0.582	0.828	0.899	0.707	0.869
Zr	0.007	0.010	0.006	0.012	0.007	0.009	0.014
Al	0.140	0.131	0.195	0.170	0.128	0.150	0.152
Cr	0.199	0.122	0.704	0.074	0.117	0.444	0.105
Fe^{2+}	3.605	3.790	3.441	3.894	3.686	3.599	3.760
Mg	1.096	1.040	0.976	1.002	1.070	1.023	1.032
Mn	0.056	0.062	0.055	0.052	0.056	0.049	0.053
Ni	0.004	0.005	0.005	0.008	0.007	0.007	0.003
Nb	0.000	0.000	0.000	0.000	0.000	0.000	0.000
Total	5.966	6.012	5.964	6.040	5.970	5.988	5.988

Each column represents a single analysis.

Table 5 Koidu kimberlitic oxides

KD-81-DZB-A2							
Mineral "H"							
	1	2	3	4	5	6	7
TiO_2	16.52	16.69	18.13	12.85	17.57	14.06	15.63
ZrO_2	0.55	0.30	0.16	0.35	0.26	0.26	0.13
Al_2O_3	2.10	2.04	2.02	2.49	1.83	2.10	1.87
Cr_2O_3	1.76	4.24	4.16	11.09	2.72	8.74	5.75
FeO	66.63	64.93	62.68	62.55	65.31	63.61	64.47
MgO	10.30	9.96	11.32	9.32	10.35	10.78	9.58
MnO	1.00	0.95	1.07	1.01	1.03	0.84	0.99
NiO	0.15	0.08	0.12	0.09	0.04	0.11	0.13
Nb_2O_5	0.00	0.00	0.00	0.00	0.00	0.00	0.00
Total	99.01	99.19	99.66	99.75	99.11	100.50	98.55
CATIONS TO 7 OXYGENS							
Ti	0.842	0.844	0.898	0.648	0.888	0.701	0.799
Zr	0.018	0.010	0.005	0.012	0.009	0.008	0.004
Al	0.168	0.162	0.157	0.197	0.145	0.165	0.150
Cr	0.094	0.226	0.217	0.583	0.145	0.458	0.309
Fe^{2+}	3.779	3.654	3.455	3.509	3.673	3.528	3.668
Mg	1.041	0.999	1.112	0.932	1.037	1.066	0.971
Mn	0.057	0.054	0.060	0.058	0.059	0.047	0.057
Ni	0.008	0.004	0.007	0.005	0.002	0.006	0.007
Nb	0.000	0.000	0.000	0.000	0.000	0.000	0.000
Total	6.007	5.953	5.911	5.949	5.958	5.979	5.965

Each column reprents a single analysis.

Table 5 Koidu kimberlitic oxides.

	KD-81-DP-DZB-A2						
	Mineral "H"					Spinel Cores	
	15	16	17	18	19	1	2
TiO_2	13.82	14.50	16.89	16.91	16.23	5.92	5.57
ZrO_2	0.15	0.22	0.41	0.69	0.39	0.08	0.22
Al_2O_3	2.19	2.23	2.01	1.90	1.98	3.28	3.89
Cr_2O_3	12.09	11.29	2.55	1.14	2.21	47.67	46.97
Fe_2O_3	——	——	——	——	——	11.67	12.34
FeO	60.19	59.48	67.21	67.49	66.44	21.28	20.50
MgO	11.24	11.22	10.05	9.87	10.83	10.53	10.90
MnO	0.99	0.98	0.91	0.89	0.95	0.73	0.79
NiO	0.11	0.12	0.14	0.08	0.09	0.11	0.03
Nb_2O_5	0.00	0.00	0.00	0.00	0.00	0.03	0.00
Total	100.78	100.04	100.17	98.97	99.12	101.31	101.21
	CATIONS TO 7 OXYGENS					CATIONS TO 32 OXYGENS	
Ti	0.679	0.715	0.851	0.866	0.825	1.200	1.125
Zr	0.005	0.007	0.013	0.023	0.013	0.010	0.028
Al	0.169	0.172	0.159	0.152	0.157	1.045	1.231
Cr	0.624	0.585	0.135	0.061	0.118	10.157	9.970
Fe^{3+}	——	——	——	——	——	2.367	2.494
Fe^{2+}	3.288	3.262	3.767	3.844	3.759	4.796	4.604
Mg	1.094	1.097	1.004	1.002	1.092	4.231	4.364
Mn	0.055	0.055	0.052	0.051	0.055	0.166	0.179
Ni	0.006	0.007	0.007	0.005	0.005	0.023	0.006
Nb	0.000	0.000	0.000	0.000	0.000	0.003	0.000
Total	5.900	5.900	5.988	6.004	6.024	23.998	24.001

Each column represents a single analysis.

Table 5 Koidu kimberlitic spinels

	KD-81-DZB-A1							
	Groundmass spinels							
	Center	2	3	4	Edge	Center	Middle	Edge
TiO_2	0.05	0.51	0.08	0.31	11.46	0.07	0.09	0.22
ZrO_2	0.10	0.11	0.06	0.08	0.10	0.10	0.05	0.10
Al_2O_3	0.21	0.47	0.24	0.26	2.23	0.33	0.35	0.39
Cr_2O_3	0.24	0.23	0.28	0.20	0.10	2.16	2.15	2.09
Fe_2O_3	69.29	67.81	70.00	71.01	49.48	67.46	67.88	69.46
FeO	31.48	31.90	29.56	25.91	29.78	31.23	28.35	24.75
MgO	0.07	0.01	1.27	3.67	7.91	0.23	1.83	4.37
MnO	0.04	0.01	0.14	0.32	0.60	0.12	0.24	0.29
NiO	0.00	0.05	0.05	0.10	0.14	0.10	0.18	0.20
Nb_2O_5	0.00	0.00	0.00	0.00	0.00	0.00	0.00	0.00
Total	101.48	101.10	101.68	101.86	101.80	101.80	101.12	101.87
	CATIONS TO 32 OXYGENS							
Ti	0.012	0.116	0.019	0.068	2.407	0.015	0.021	0.049
Zr	0.015	0.016	0.009	0.011	0.013	0.015	0.007	0.014
Al	0.073	0.168	0.085	0.089	0.735	0.117	0.124	0.135
Cr	0.057	0.056	0.067	0.047	0.022	0.515	0.510	0.481
Fe^{3+}	15.815	15.512	15.793	15.706	10.401	15.308	15.310	15.259
Fe^{2+}	7.985	8.111	7.411	6.368	6.956	7.874	7.105	6.042
Mg	0.032	0.006	0.567	1.606	3.292	0.102	0.817	1.902
Mn	0.010	0.003	0.037	0.080	0.141	0.030	0.062	0.071
Ni	0.000	0.012	0.013	0.025	0.031	0.024	0.044	0.047
Nb	0.000	0.000	0.000	0.000	0.000	0.000	0.000	0.000
Total	23.999	24.000	24.001	24.000	23.998	24.000	24.000	24.000

Each column represents a single analysis.

Table 5 Koidu kimberlitic spinels

KD-81-D23-A2

Spinel Cores (Cont'd)

	3	4	5	6	7	8	9
TiO_2	6.56	6.48	7.58	6.14	5.59	7.09	6.41
ZrO_2	0.35	0.11	0.08	0.12	0.16	0.13	0.13
Al_2O_3	0.41	3.40	3.59	2.47	3.17	2.06	3.08
Cr_2O_3	2.58	44.50	38.82	46.94	47.20	41.32	46.88
Fe_2O_3	54.80	13.68	14.16	12.01	12.45	15.48	11.10
FeO	28.35	21.23	23.86	20.92	20.66	21.60	21.01
MgO	4.93	10.80	9.10	10.47	10.60	10.24	10.75
MnO	1.33	0.81	0.79	0.88	0.81	0.95	0.77
NiO	0.03	0.04	0.10	0.05	0.00	0.04	0.04
Nb_2O_5	0.07	0.00	0.01	0.00	0.00	0.00	0.00
Total	99.41	101.05	98.09	100.00	100.64	98.91	100.17
			CATIONS TO 32 OXYGENS				
Ti	1.460	1.313	1.598	1.265	1.139	1.482	1.310
Zr	0.050	0.014	0.011	0.016	0.021	0.018	0.018
Al	0.144	1.080	1.185	0.798	1.014	0.677	0.987
Cr	0.605	9.490	8.607	10.165	10.123	9.084	10.085
Fe^{3+}	12.203	2.776	2.987	2.475	2.542	3.239	2.272
Fe^{2+}	7.015	4.789	5.596	4.793	4.686	5.023	4.782
Mg	2.174	4.344	3.803	4.273	4.286	4.245	4.360
Mn	0.333	0.185	0.189	0.205	0.187	0.224	0.177
Ni	0.007	0.009	0.024	0.011	0.001	0.008	0.008
Nb	0.010	0.000	0.001	0.000	0.000	0.000	0.000
Total	24.001	24.000	24.001	24.001	23.999	24.000	23.999

Each column represents a single analysis.

Table 5 Koidu kimberlitic spinels

	KD-81-DZ3-8						
	Groundmass spinels						
	Center	2	3	Edge	Center	Mantle	Mantle
TiO_2	0.12	0.11	1.23	6.64	6.07	11.08	13.01
ZrO_2	0.10	0.08	0.11	0.10	0.07	0.14	0.06
Al_2O_3	0.26	0.21	0.40	1.04	2.24	2.46	2.26
Cr_2O_3	0.15	0.13	0.13	1.91	47.90	25.11	18.33
Fe_2O_3	69.29	69.44	68.75	56.13	11.05	26.53	29.66
FeO	31.08	29.01	25.03	29.45	21.65	24.12	26.69
MgO	0.26	1.33	4.52	4.79	9.89	11.44	10.82
MnO	0.09	0.24	0.37	0.87	0.79	0.96	0.97
NiO	0.12	0.12	0.16	0.08	0.11	0.14	0.11
Nb_2O_3	0.00	0.00	0.00	0.00	0.00	0.00	0.00
Total	101.47	100.67	100.70	101.01	99.77	101.98	101.91
	CATIONS TO 32 OXYGENS						
Ti	0.027	0.025	0.273	1.451	1.259	2.239	2.648
Zr	0.014	0.012	0.016	0.015	0.009	0.018	0.008
Al	0.094	0.073	0.137	0.357	0.728	0.778	0.722
Cr	0.036	0.031	0.030	0.438	10.443	5.338	3.924
Fe^{3+}	15.789	15.821	15.256	12.274	2.293	5.369	6.042
Fe^{2+}	7.870	7.346	6.172	7.157	4.994	5.424	6.044
Mg	0.119	0.601	1.987	2.076	4.066	4.585	4.366
Mn	0.022	0.061	0.092	0.213	0.184	0.218	0.222
Ni	0.030	0.030	0.037	0.019	0.024	0.031	0.025
Nb	0.000	0.000	0.000	0.000	0.000	0.000	0.000
Total	24.001	24.000	24.000	24.000	24.000	24.000	24.001

Each column represents a single analysis.

Table 5 . Koidu kimberlitic oxides

KD-81-DZB-A1

	Area X							
	B	C	I	A	K	F	D	H
TiO_2	17.67	13.31	2.66	13.88	14.73	6.77	18.56	16.52
ZrO_2	0.11	0.08	0.15	0.25	0.15	0.09	0.22	0.27
Al_2O_3	1.96	2.13	3.49	2.17	2.11	3.42	1.78	1.99
Cr_2O_3	0.96	11.35	55.22	5.15	9.83	44.12	2.48	2.99
Fe_2O_3	——	——	8.12	39.92	——	12.61	——	——
FeO	66.80	60.55	19.11	29.63	60.57	21.66	63.20	64.57
MgO	10.21	10.21	9.72	9.25	10.58	10.53	10.91	10.71
MnO	1.03	0.98	0.67	0.96	1.01	0.76	1.02	0.90
NiO	0.01	0.01	0.06	0.10	0.04	0.03	0.10	0.05
Nb_2O_3	0.00	0.00	0.00	0.00	0.00	0.00	0.00	0.00
Total	98.75	98.62	99.20	101.31	99.02	99.99	98.37	98.00
Cations To Oxygens	7	7	32	32	7	32	7	7
Ti	0.901	0.673	0.552	2.890	0.738	1.388	0.935	0.845
Zr	0.004	0.003	0.019	0.034	0.005	0.012	0.007	0.009
Al	0.157	0.169	1.134	0.707	0.166	1.099	0.141	0.160
Cr	0.052	0.604	12.038	1.127	0.518	9.512	0.138	0.161
Fe^{3+}	——	——	1.685	8.318	——	2.588	——	——
Fe^{2+}	3.787	3.408	4.406	6.861	3.377	4.939	3.544	3.672
Mg	1.032	1.024	3.995	3.816	1.051	4.280	1.090	1.086
Mn	0.059	0.056	0.157	0.225	0.057	0.175	0.058	0.052
Ni	0.000	0.000	0.013	0.022	0.002	0.006	0.006	0.003
Nb	0.000	0.000	0.000	0.000	0.000	0.000	0.000	0.000
Total	5.992	5.937	23.999	24.000	5.914	23.999	5.919	5.988

Each column represents a single analysis.

Table 5 Koidu kimberlitic spinels

	KD-81-DZB-B				KD-81-DZB-A1		
	Center	Mantle	Center	Mantle#2	Center	Middle	Mantle
TiO_2	5.91	15.76	5.77	50.70	2.80	5.66	14.89
ZrO_2	0.13	0.16	0.02	0.30	0.01	0.07	0.24
Al_2O_3	3.03	1.97	3.07	0.00	3.81	3.35	2.30
Cr_2O_3	47.32	1.94	46.80	0.22	55.90	46.29	1.54
Fe_2O_3	11.37	39.37	11.35	8.48	7.45	12.77	——
FeO	21.12	30.48	21.69	23.27	18.67	20.67	69.92
MgO	10.26	9.50	9.69	12.46	10.17	10.45	9.93
MnO	0.84	0.95	0.70	2.18	0.64	0.79	0.83
NiO	0.14	0.17	0.13	0.00	0.06	0.15	0.10
Nb_2O_5	0.00	0.00	0.00	1.79	0.00	0.00	0.00
Total	100.12	100.30	99.22	99.40	99.51	100.20	99.75
Cations To Oxygens	32	32	32	3	32	32	7
Ti	1.214	3.307	1.200	0.892	0.575	1.159	0.948
Zr	0.017	0.022	0.003	0.003	0.002	0.009	0.007
Al	0.975	0.648	1.002	0.000	1.229	1.075	0.173
Cr	10.225	0.428	10.232	0.004	12.085	9.970	0.078
Fe^{3+}	2.338	8.267	2.362	0.149	1.532	2.618	———
Fe^{2+}	4.827	7.112	5.016	0.455	4.270	4.710	3.722
Mg	4.179	3.953	3.994	0.434	4.144	4.243	0.942
Mn	0.195	0.224	0.165	0.043	0.149	0.183	0.045
Ni	0.030	0.039	0.028	0.000	0.013	0.032	0.005
Nb	0.000	0.000	0.000	0.019	0.000	0.000	0.000
Total	24.000	24.000	24.002	1.999	23.999	23.999	5.920
Mole%							
Hem				13.78			
Ilm				42.09			
Geik				40.15			
Pyroph				3.98			

Each column represents a single analysis.
Hem=hematite; Ilm=ilmenite; Geik=geikielite; Pyroph=pyrophanite.

MAGSAT vector anomalies related to the West African and Amazonian cratons

Paul B. Toft and Stephen E. Haggerty

Department of Geology, University of Massachusetts

Amherst, Massachusetts 01003

ABSTRACT

MAGSAT (MGST 4/81) anomalies are similar over the West African and Amazonian cratons. Differences between total field (ΔB) and N-S horizontal vector (ΔX) anomalies over both cratons are largely those that would be expected for anomalies due to induced magnetization. At the present low magnetic inclinations, the negative ΔX anomalies which are spatially associated with the cratonic shields imply normally-directed positive magnetization-contrast sources. Archean nucleii of the shields appear to be more strongly magnetized than Proterozoic segments, but both stand out from adjacent basins and fold belts. Under specified conditions, the uncertainty inherent in the poorly defined MAGSAT anomaly zero level may possibly be able to be reduced by co-analysis of anomaly profiles taken along opposite sides of the continental rejoin in a pre-drift reconstruction. Synthesis model anomalies generated from lithological and gravity data reproduce reasonably well the cratonic negative MAGSAT anomalies. The dominant contribution to MAGSAT ΔX anomalies over the West African and Amazonian cratons results from magnetization contrasts within the crust. These are modulated by the effects of structural contrasts, intrusions and metamorphism within the lithosphere, and are localized by the preferred distribution of iron deposits into the more ancient crustal blocks.

INTRODUCTION

Since the introduction of satellite-measured global-scale total field magnetic anomaly (ΔB) maps from POGO (Regan et al., 1975) and MAGSAT (Langel et al., 1982b) a variety of techniques have been employed in interpretation of the anomalies, including: 1) visual comparison of anomalies to large scale tectonic features of the Earth (e.g., Frey, 1982), 2) comparison of anomalies to upward-continued aeromagnetic anomalies (e.g., Langel et al., 1980a; Taylor et al., 1981; von Frese et al., 1982b; Won and Son, 1982), 3) comparison of magnetization anomalies calculated by equivalent source inversion techniques (Mayhew, 1979) to heat flow (Mayhew, 1982b), to crustal thickness (Schnetzler and Allenby, 1983), and to the geological characteristics of continental crustal blocks (e.g., Mayhew et al., 1980; Mayhew, 1982a; Mayhew and Galliher, 1982; Langel and Thorning, 1982), and 4) comparison of magnetic anomalies to gravity anomalies (e.g., von Frese et al., 1981a; 1981b; 1982a; Taylor et al., 1981). Although Haggerty (1978; 1979) has suggested a possible contribution from high Curie temperature metal alloys, most analyses have employed the simplyfying assumption, due to Wasilewski et al. (1979), that the mantle is non-magnetic, and, as summarized by Taylor et al. (1983) and by Harrison (1983), have concluded that the anomalies may be the combined result of surface geological features, lateral contrasts in intracrustal magnetization, and variations in thickness of a magnetized layer due either to magnetite Curie isotherm (580°c) topography or to crustal thickness.

There are still some outstanding problems, however. Relatively high magnetization intensities (1 - 10 $A.m.^{-1}$) have been inferred from several lines of evidence (e.g., Regan and Marsh, 1982;

Wasilewski and Mayhew, 1982; McLeod, 1983; Schnetzler and Allenby, 1983). The MAGSAT anomalies are relative to an arbitrary and varying base level (Langel et al., 1982b; 1982c). Little use has been made to date of the MAGSAT vector anomaly maps produced by Langel et al. (1982c), except for the work by Galliher and Mayhew (1982). And, although on a global scale continental regions tend to appear as the most strongly magnetized regions (Regan et al., 1975; Frey, 1982), most of the quantitative analyses have been made within a single continent.

In this paper we apply simple geological criteria in a qualitative evaluation of the initial (MGST 4/81) MAGSAT maps (Langel et al., 1982b; 1982c) over West Africa and northern South America; more recent global anomaly maps confirm the reality of most of the features of the MGST 4/81 maps (Cain et al., 1984; Langel and Frey, 1982).

Our strongest interest is in the Man shield of the West African craton and in its contrasts and relationships to the surrounding areas as portrayed by MAGSAT. The shield contains abundant kimberlites, whose distribution and included megacrysts and xenoliths provide information on regional structural trends and petrology, geochemistry and mineralogy (e.g., Haggerty, 1982; Haggerty, 1983; Haggerty and Tompkins, 1983; Haggerty and Toft, 1984) of significance to geophysical models of the local lithosphere.

Our regional framework for analysis of the MAGSAT maps incorporates aspects of lithology, gravity anomalies, and the Earth's main magnetic field. This is not an evaluation of the MAGSAT maps solely in relation to continental drift. Rather, it is an attempt to address some outstanding problems related to the interpretation of satellite magnetic data, and is particularly an effort to analyze portions of the MAGSAT vector anomaly maps from the perspective of a synthesis of geological and geophysical data.

REGIONAL GEOLOGY

We examine first the regional geology as ground truth data. The West African and Amazonian cratons, which were stabilized before 1500 m.y. ago (Clifford, 1970; de Almeida et al., 1981), are shown in Figure 1 which outlines the areas enlarged in subsequent Figures where data are compiled on the Bullard et al. (1965, fig. 5) 500 fathom (≈ 1000 m) physiographic reconstruction of the pre-drift fit of Africa and South America. The fit has survived well (Smith and Hallam, 1970; Sclater et al., 1977; Rabinowitz and LaBreque, 1979; Martin et al., 1981), and for hand compilation and visual examination of geological and geophysical features away from the continental margins has the advantage that it shows latitude and longitude for both continents in a roughly equal-angle, equal-area configuration.

The generalized regional geology of West Africa and northern South America is shown in Figure 2 and locations are referred to Figure 3. Marginal to the cratons are fold belts composed of rocks with much younger radiometric age dates, in the range 1100 - 350 m.y. ago (Hurley et al., 1967). Within both cratons the shield areas, uplifted regions of exposed metamorphic and igneous rocks, are primarily of two whole-rock age groups - an Archean group (≥ 2500 m.y. old) and a Lower Proterozoic group (2200 - 1800 m.y. old) (Hurley and Rand, 1973). Basin or platform deposits partially obscure the craton and fold belt structures, but contribute to the lithological details of the reconstruction, the principal points of which were enumerated by de Almeida and Black (1972) and most recently reviewed by Torquato and Cordani (1981).

Shield areas

Both cratons display a large scale basin and swell structure, with the Guiana and Guaporé shields north and south respectively of the Amazon basin and the Reguibat and Man shields north and south of the Taoudeni basin in West Africa (Figures 2 and 3).

Archean exposures are more vast in West Africa than in South America; both are characterized as migmatized granitic and amphibole-pyroxene-garnet banded gneisses, granites, amphibolites, charnockites and ferruginous quartzites; granite intrusion and the most recent regional metamorphism, to amphibolite or granulite facies, occurred about 2800 - 2500 m.y. ago. The Archean and Proterozoic zones in the Man and Guiana shields are separated by major mylonitized fault zones. Rocks of the Proterozoic age group are also characterized as gneisses, migmatites and syn- and post-tectonic granites but also include amphibolites, phyllites, schists, and quartzites which are only occasionally ferruginous; these rocks were most recently regionally metamorphosed, up to greenschist or amphibolite facies, and intruded by synkinematic granites, at about 2200 - 1800 m.y. ago in a major orogenic event termed the Eburnean in southern West Africa and the Trans-Amazonian in South America (for West Africa : Louis, 1970; Dillon and Sougy, 1974; Bessoles, 1977; Black, 1980; Choubert et al., 1971; for South America: de Almeida et al., 1973; Choubert, 1974; de Almeida et al., 1981 ; Gibbs and Barron, 1983; correlative: Hurley et al., 1967; Choubert, 1969; de Almeida and Black, 1972; Gruss, 1973; Hurley and Rand, 1973; Torquato and Cordani, 1981).

A third, relatively minor, uplift in the West African craton exposes a small area of Proterozoic rocks to the north of the Tindouf basin (Dillon and Soughy, 1974). Uplift in the Ahaggar region east of the craton has exposed

2700 and 2000 m.y. old rocks (Hurley et al., 1967), broadly similar in lithology to those in the West African craton (Black and Girod, 1970). Other African shield regions decrease in age along the coast of Africa to 1300 - 800 m.y. old in the Namaqualand shield of the Kalahari craton (Clifford, 1970; Hurley and Rand, 1973).

In the Guiana shield of the Amazonian craton the Archean age of the rocks south of the Roraima sediments (Figures 2 and 3) is still open to question (Bosma et al., 1983), and rock and mineral ages younger than 1800 m.y. old are common in the west and south of the shield (Kroonenberg, 1982; Priem et al., 1982); most of the Guaporé shield is not older than Trans-Amazonian. Elsewhere in northern South America the São Fransisco craton was extensively rejuvenated during the interval 1500 - 1100 m.y. ago and subsequently at about 500 m.y. ago (de Almeida et al., 1973; 1981; Wernick, 1981). Finally, the São Luis craton in northern Brazil lithologically (de Almeida et al., 1981) and radiochronologically (Hurley et al., 1967) closely resembles the Eburnean segment of the Man shield and lies adjacent to it in the Bullard reconstruction (Torquato and Cordani, 1981).

Fold belts

The fold belts in Figure 2 delineate regions of Precambrian or Paleozoic deformation subsequent to the Eburnean - Trans-Amazonian orogeny, and include unmetamorphosed sediments and wide ranges of metamorphic and igneous rock types; Pan-African - Brasiliano cycle deformation dated as about 450 ± 250 m.y. old (Hurley, 1973) is generally restricted to the metasedimentary margins of the fold belts adjacent to craton regions, whereas the gneissic and granitic infrastructures of the fold belts frequently display Lower Proterozoic and

and Archean ages (de Almeida et al., 1973; Grant, 1973; Machens, 1973; Bessoles, 1977; 1980; de Almeida et al., 1981; Choubert and Faure-Muret, 1971). Suture belts in Figure 4, from Frey (1979) and Burke et al. (1977) are shown without respect to age, and do not exactly correspond to the fold belts in Figure 2.

The tectonic origin of these fold belts is not, necessarily, an open and shut case, but the conflicting hypotheses of an ensialic in-situ origin (Hurley, 1973; Kröner, 1977; McElhinny and McWilliams, 1977; McWilliams and Kröner, 1981) and a Wilson-cycle tectonics origin (Burke et al., 1977; Black et al., 1979) may be generally reconciled by assuming the opening and closing of marginal, narrow seas. Exposed ophiolitic assemblages are relatively rare, but see, for example, Leblanc (1976), de Almeida et al. (1981), Fountain and Salisbury (1981) and Berbert et al. (1981). In either case, the fold belts are important in the regional tectonic control of the locus of Mesozoic southern South Atlantic rifting, generally parallel to the fold belt structural trends in both continents (de Almeida et al., 1973; Nairn and Stehli, 1973; Torquato and Cordani, 1981).

Basins and continental rifting

The major basins in Figure 2 are characterized by depth to basement isopachs (Bronner et al., 1980; de Almeida et al., 1981) indicating the areas of greatest subsidence. The intracratonic basin is older in West Africa than in northern South America: deposition within the Taoudeni basin was strongly developed between 1100 - 650 m.y. ago, primarily toward a trough in the north (see Figure 2) but 4 - 8 km of sediment are also associated with the Gourma aulacogen in the south (Dillon and Sougy, 1974; Black et al., 1979;

Bronner et al., 1980; Lesquer and Moussine-Pouchkine, 1980), whereas the sedimentary record in the Amazon basin begins in the Silurian with subsequent deposition being directed toward three subsidiary basins separated by the Iquitos and Purus arches at about 70°W and 60°W respectively (Bigarella, 1973; de Almeida et al., 1981). A much earlier cycle of sedimentary deposition is also recorded, in the Roraima Formation on the Guiana shield and the Tarkwaian deposits on the eastern Man shield, prior to 1700 m.y. ago (Hurley and Rand, 1973). The major part of the northern South American sedimentary record and the graben surrounding the Atlantic Ocean (see Figure 4) developed in response to stress associated with Mesozoic continental rifting (Burke and Whiteman, 1973; Nairn and Stehli, 1973; Burke, 1976; Burke et al., 1977;).

Volcanic features

Injections of basaltic dikes and sills and eruptions of flood basalts were also intimately associated with the separation of the continents (e.g., Bigarella, 1973; Basaltic Volcanism Study Project, 1981, pp. 33 - 35), as was the slightly later kimberlite volcanism evident in the ≈ 120 m.y. old dike-swarms and pipes of Liberia and Sierra Leone (Haggerty, 1982); kimberlites, from Dawson (1980) and Bardet (1973), are shown in Figure 4 as a guide to potential lower crustal and upper mantle sampling sites in relation to large scale magnetic anomalies. Carbonatitic intrusions post-date the kimberlites at about 60 m.y. old (Marsh, 1973; Moore, 1976; Herz, 1977), and volcanic sites active within the last 1 m.y. (Trombka and Lowman, 1979) are included in Figure 4 as a primitive guide to high heat flow regions.

Nature and distribution of iron ore deposits

In the analysis of any magnetic anomaly maps it should be natural first to ask whether there are any known highly magnetic bodies in the region in question. Iron ore deposits in West Africa and northern South America shown in Figure 4 are the total resources (i.e., both known reserves and potential ores, United Nations (1970)) as of 1970, from Marelle and Abdullah (1970) and Alvarado (1970) slightly updated for South America (Dorr, 1973a; 1973b; Tolbert et al., 1973).

Within the major cratons the largest resources are magnetite- and hematite-rich oxide and oxide-silicate facies bedded iron-formations of the Lake Superior type (Gross, 1965, 1970). Many of these deposits are referred to as itabirites, i.e., laminated metamorphic rocks dominantly or entirely composed of granular quartz and iron oxides (Dorr, 1952), corresponding in general terms to the ferruginous quartzites which are most prominently developed in the 2700 m.y. old and, to a lesser extent, the 2000 m.y. old shield rocks (Marelle and Abdullah, 1970; Alvarado, 1970; Goodwin, 1973; Gruss, 1973). They were probably originally chemical sediments deposited without a strong volcanogenic association in shallow sea or continental shelf type of environments (Gross, 1970; 1973), and have been subsequently metamorphically deformed and super- and hypogene enriched into substantial iron ore deposits.

The massive variety of iron deposit (Gross, 1970) is well developed in the Atlas Mountains (Marelle and Abdullah, 1970) and in Peru and Chile (Alvarado, 1970), originating either from iron carbonate sediments, or magmatic activity, for example the El Laco magnetite lava flow in Chile (Park, 1961). Residual deposits, the third and last major variety of iron deposit (Gross, 1965; 1970), are common as lateritic crusts on basic intrusive rocks throughout the areas of wet tropical climate (Alvarado, 1970; Marelle and Abdullah, 1970).

GRAVITY ANOMALIES

Relating magnetic anomalies to gravity anomalies is a common approach to analysing magnetic anomaly data. At a cratonic or continental scale the available gravity data sets are maps of free air and geoid values and Bouguer anomaly maps.

The most recent global free air gravity anomaly maps (not shown) which have been published in a graphic or map form are GEM 8 (Wagner et al., 1977) and GEM 10 (Marsh, 1979). Values were derived from ground-based and satellite-measured data, and the high degree and order ($n > 12$) maps show features of half-wavelength $\approx 10^{\circ}$ with amplitudes of a few mgals. Above the West African and Amazonian cratons both maps are dominated by negative anomalies of peak amplitude -20 mgal, which overlie the centrally located intra-cratonic basins. Positive anomalies to the north and south slightly overlap the basin regions and are less closely spatially related to the shield regions than the positives are to the basins. However, the Guiana shield and particularly the Man shield areas both correspond to relatively weak ($\leq +12$ mgal) but persistent positive anomalies.

In the NASA GSFC global gravity geoid shown by Taylor et al. (1983), which is based on a combination of GEM 10B and $1^{\circ} \times 1^{\circ}$ surface gravity data, the Amazonian craton is swamped by a gradient field from the Andes to the Atlantic coast, whereas in West Africa the general area of the Man shield is a prominent positive geoid feature but other features are poorly resolved.

Bouguer gravity anomalies (Figure 5) for West Africa (Slettene et al., 1973) and South America (Wilcox, 1977) are partially from ground-based observations, but are supplemented by statistically, topographically and geophysically predicted values in the unsurveyed areas (Breville et al., 1973; Brown et al., 1980; see also Orlin, 1966). Only selected contours are shown in Figure 5; contours were selected by visual examination and were chosen, with constant contour intervals as far as possible, so as to emphasize features with wavelengths ≥200 km, the expected spatial resolution of MAGSAT (see following section). West African craton values range between +20 and -40 mgal, compared to Amazonian craton values ranging between about +40 and -80 mgal.

Some of the Bouguer anomalies are a strong function of topography, in part because of the prediction methods. An example is the strongly negative Andean mountains. East of the Andes are several positive anomalies overlying basins and plains; the Amazon basin, for example, is characterized by a series of short wavelength mostly positive anomalies. The ≤-40 mgal anomalies over the Amazonian craton shield areas have trends which align with superimposed sedimentary deposits (Wilcox, 1977), such as over the Roraima sediments of the Guiana shield, and over the volcano-sedimentary deposits overlying the central region of the Guaporé shield.

Within the West African craton are two prominent relatively positive (≥ -20 mgal) Bouguer anomalies over the Taoudeni basin, both of which are related to the Gourma aulacogen (Lesquer and Moussine-Pouchkine, 1980). The western boundary of the craton is marked by a shift to positive values associated with the Mauritanide fold belt (Chiron, 1974), whereas the craton is bounded in the east by a series of short wavelength positive anomalies (Louis, 1970) roughly

apparent in Figure 5 as the trend of the -40 mgal contour. The western Archean zones of the shield regions have generally negative ($\leq$ -40 mgal) Bouguer values and appear to be undercompensated (Louis, 1970; Behrendt and Wotorson, 1974), but the coastal gradient is clearly compromising the Man shield Bouguer anomaly. The eastern segment of the Man shield shows no pronounced features in Figure 5, but is, in detail, a region of short wavelength highs and lows corresponding to small grabens and uplifts (Hastings, 1983), whereas the central region of the Reguibat shield is relatively positive and the eastern section is swamped by a large negative anomaly extending over both shield and basin regions.

MAGSAT ANOMALIES

The assembly and the expected spatial resolution of the MAGSAT anomaly maps are critical to their geological interpretation. Scalar, or total field, anomalies (ΔB) and north-south horizontal vector anomalies (ΔX) from MAGSAT (4/81) maps by Langel et al. (1982b; 1982c) are transposed onto the Bullard reconstruction in Figures 6 and 7; magnetic inclinations (1980) are interpolated from Langel et al. (1982b) and Dobrin (1976, fig. 14.8). The anomaly maps were derived from 550 - 350 km altitude orbital profiles by subtracting from screened magnetically "quiet" data : 1) spherical harmonic model main field values, 2) potential function estimates of external fields, and 3) linear ramps of a few tens of degrees in latitude; statistically outlying values were then discarded and the residual profiles were compiled and contoured (Langel et al., 1982b; 1982c).

The resultant "crustal" anomaly maps show features with half-wavelengths on the order of 1^0 - 10^0 and of magnitude $\lesssim |15|$ nT, but considering 1) that the

maps are compromised by a poorly defined zero level, were contoured on the basis of $2^{\circ} \times 2^{\circ}$ block averages at unequalized altitudes, and, at equatorial latitudes, include ΔB and ΔX noise levels of about 1 nT (Langel et al., 1982b; 1982c), 2) that there are unresolved problems in the spherical harmonic separation of core, crustal and ionospheric sources (Langel and Estes, 1982; Carle and Harrison, 1982; Klumpar and Greer, 1982; Alldredge, 1983a), 3) that the north-south orbit and along-track data processing emphasize east-west striking anomalies (Langel et al., 1982b), particularly in ΔB at low latitudes, and 4) considering the results of spectral analyses in the spatial (Sailor et al., 1982; Alldredge, 1983b) and time (Alldredge, 1983c) domains, it is clear that only persistent anomalies exceeding about 2 nT in magnitude may be plausibly related to lithospheric rocks, and then only to geological units exceeding about 200 km diameter.

Anomalies over the cratons

Over both the West African and Amazonian cratons, which are presently situated within 40° magnetic inclination of the geomagnetic equator (0° inclination) are negative MAGSAT ΔB anomalies where the main field is close to horizontal over the southern shield exposures, positive anomalies over the central parts of the cratons at about 15° north inclination, and negative anomalies at or just above 30° inclination (Figures 2 and 6). These same general features are also evident in the POGO data, becoming more clearly resolved as the data continued to be processed from Regan et al. (1975) through Frey et al. (1979) and Langel et al. (1982b).

According to general principles, and as described by Langel et al. (1982c),

induced Δ B and Δ X anomalies generated over bodies of high relative magnetic susceptibility at or close to the geomagnetic equator should be negative and very similar in form and location, as are the anomalies over the north and south of both cratons (Figures 6 and 7). The amplitudes of the Δ B and Δ X anomalies are closely equivalent at the geomagnetic equator, and diverge with increasing magnetic inclination. If induced, the negative Δ X anomalies should have negative Δ Z (vertical component) and positive Δ Z anomalies to the north and south respectively, as in fact, they do (compare Figure 7 to the Δ Z map by Langel et al. (1982c)). Relationships with Δ Y (horizontal east-west) are equally clear in theory, but are less obvious in practice, possibly because of the poorer overall quality (Langel et al., 1982c) of the Δ Y map.

But although these cratonic anomalies are persistent and behave as if they are induced, they are not well isolated from adjacent features, and where the main field is very close to horizontal an induced negative Δ B or Δ X anomaly is centered over its source, but has smaller positive cusps to the north and south. This can lead to a superimposition of anomalies, as described in Central Africa by Hastings (1982), so that, for example, the positive Δ X anomaly over the Taoudeni basin may in part be due to the strongly magnetic regions to the south and north.

Induced magnetic anomalies are, furthermore, a function of magnetic inclination, complicating any spatial relationships to other data. However, where the main field is close to horizontal, as in these cratonic regions, Δ X is less sensitive to inclination than is Δ B; reduced-to-the-pole (RTP) anomalies, although the standard techniques are non-ideal at low inclinations (Langel and Frey, 1983), have maximum and positive values directly over their sources. Ignoring possible overlap, at low magnetic inclinations

the most significant difference between the RTP ΔB map of South America by Hinze et al. (1982), the unreduced ΔB map (Figure 6), and the ΔX map (Figure 7), should be in the geographic latitude location of a given anomaly peak as a function of magnetic inclination.

This is tested in Figure 8 where the arcuate line of profile is selected in order to intersect as nearly as possible the peak values of the profiled anomalies in all three maps, and to be roughly perpendicular to magnetic inclination contours. Relative to the RTP anomalies the majority of the profiled anomaly peak shifts can reasonably be attributed to the effects of magnetic inclination: the peak displacements are greater for Δ B than Δ X, are symmetric about the geomagnetic equator, and increase in magnitude poleward. This relationship is also evident over the rest of South America and the surrounding oceanic areas, is further support for an induced origin of the anomalies, and is subsequently employed in geographically relating the Figure 7 Δ X anomalies to geology and gravity.

Anomalies related to the shield areas

In both cratons it is the shield areas which spatially correspond to negative ΔX anomalies indicating regions of positive relative magnetization. Over the Amazonian craton the Guiana shield negative (≤-2 nT), which shifts progressively slightly equatorward from ΔB to ΔX to RTP, corresponds to the veneer of Roraima sediments, to a Bouguer low and topographic high, to the Archean iron-rich exposures north of the Roraima, and it closes at the edge of the continental shelf. The Guaporé shield negative anomaly, at about

0° inclination, corresponds to (Phanerozoic) cover, low Bouguer values, exposed Proterozoic shield, and is interrupted along 50° west longitude where the craton is bounded by a marginal fold belt.

For West Africa, Hastings (1982) visually associated the Archean segments of both West African shields with stronger negative ΔB values than occur over the younger shield segments, and Figures 2 and 5 suggest a similar relationship to Bouguer anomalies. In respect of the South American inclination relationships (Figure 8), the ΔX anomaly (Figure 7) in the north of the West African craton at about 30° - 35° north inclination is a saddle with two ≤ -4 nT peaks, seemingly corresponding to the Archean and Proterozoic structure of the Reguibat shield. In contrast, the Man shield ΔX anomaly peaks (≤-4 nT) at the geomagnetic equator over an area including Archean shield and fold belt features, and decays eastward over the Eburnean Proterozoic shield segment falling to the 'zero level' by the craton boundary. Toward the west, both the Man and Reguibat shield anomalies have closures reflecting the shape of the continental shelf.

In geographic comparison to the distribution of iron deposits shown in Figure 4, the negative ΔX anomalies over the West African craton have peaks which rather closely correspond to the bedded iron-formation deposits of the Archean shield segments, particularly bearing in mind the expected latitudinal peak shift of the Reguibat shield anomalies. The Guiana shield negative ΔX anomaly may be similarly related to bedded iron formation, but the Guaporé shield is not known, to date,

to have such substantial deposits. Most generally, however, it is simply the shield areas of both cratons which are associated with negative ΔX MAGSAT anomalies.

Given that the West African and Amazonian cratonic shield areas are all four characterized by similar negative MAGSAT ΔX signatures, how general a result is this ? The São Luis craton (Figure 1) is radiometrically, lithologically and structurally closely related to these two cratons, particularly to the Eburnean segment of the the Man shield. From the West African - Amazonian craton shield-MAGSAT relationship the expected signature of the São Luis craton would be a weak negative MAGSAT ΔX anomaly, and where the craton meets the coastline (Figure 2) is a small (≈200 km) relatively (<0 nT) negative ΔX peak at 2.5°S 43°W (Figure 7).

Even if poorly resolved at the limit of resolution of MAGSAT, the anomaly appears to be well related to the São Luis craton, thus lending support to the combined West African and Amazonian craton interpretive model of MAGSAT anomalies. However, the model cannot be immediately and succesfully applied to the adjacent São Fransisco or Zaire cratons, and it is not suggested as a global model but rather as particular to the presently widely separated West African, São Luis and Amazonian cratons.

Anomalies along the continental rejoin

Our primary interest in the shields is presented here in the framework of a pre-drift reconstruction, and in placing POGO and MAGSAT maps of Africa and

South America adjacent to each other Frey et al. (1983) and Galdéano (1981; 1983) have previously noted a general correspondence across the continental rejoin of Δ B anomalies, mostly the positive ones. The rather low degree of correspondence in detail, however, can be judged from Figure 6, and it is appropriate, therefore, briefly to examine anomalies along the continental rejoin.

Profiles of MAGSAT Δ X values for the African and South American sides of the continental rejoin are presented in Figure 9, which was constructed from the Δ X map with interpolated values at other than the even integer contour values. Between African latitude 30°S and the point where the longitude line 10°W intersects the African coast, the line of the profile bisects the overlap or underlap (mismatch) of the 500 fathom (≈ 1000 m) isobath; west of 10°W for approximately 500 km the 110 m.y. old oceanic magnetic lineaments, from Sclater et al. (1981), are the lines of the profiles, which are thus located, for the most part, a few tens of kilometers seaward of the 500 fathom isobath. Vectors at about 300 km station intervals indicate the (1980) apparent magnetic inclinations in the curvilinear planes of the profiles and are proportional in length to the (1980) MAGSAT main field model values of Langel et al. (1980b; 1980c).

These profiles should not be overinterpreted, either in relation to each other or as to spatial coincidences with known structures, because 1) the zero nT base level varies in an unknown manner over the global MAGSAT maps (Langel et al., 1982b; 1982c), 2) the profiles are derived and interpolated from already smoothed 2° averages, and 3) are subject to different and rather wide ranges in main field inclination and intensity.

Nevertheless, the profiles give an immediate impression similar to that of slightly out-of-phase sine waves relative to

different base levels. Some earlier studies have suggested that certain POGO and MAGSAT anomalies in this area arise from structures pre-dating Mesozoic continental drift (Galdéano, 1981; Hastings, 1982; Hinze et al., 1982; Frey et al., 1983; Galdéano, 1983). The combined West African - Amazonian craton interpretive model certainly supports this idea in detail.

Very detailed intercontinental comparisons are compromised, however, by the poorly defined nature of the MAGSAT base level, or MAGSAT anomaly zero level. It seems possible that, in the future, the zero level ambiguity might be able to be reduced by forcing profiles like those in Figure 9 to agree with each other. Assuming similar characteristics of source volumes and magnetizations, geographically opposed RTP anomalies could be co-normalized in amplitude across a continental rejoin, allowing one of the apparent zero levels to float. Anomalies from two continents possibly could then be analyzed with respect to a similar base level. The wide range of magnetic inclinations precludes such a use of the Figure 9 profiles. Even with co-normalized RTP profiles the absolute base level still would be unknown, but the general method may be a useful approach to the zero level problem.

DISCUSSION

The previous sections have examined rather separately the geology and the gravity and MAGSAT anomalies over West Africa

and northern South America. The following discussion attempts to synthesize these observations and to pinpoint possible origins for the MAGSAT anomalies over the cratons, particularly with respect to the Man shield of the West African craton.

Surficial distribution of iron

A striking but surficial MAGSAT-geological correlation emerging from the West African - Amazonian craton interpretive model is the association of iron ore deposits with regions which are implied from the MAGSAT anomalies to be strongly magnetic. The relationship applies only to certain of the Precambrian bedded iron-formations within the two cratons, however, and is not suggested as a global or general relationship. Exposed iron-formations, including non-economic iron-enriched sequences, do not have the volume to be solely responsible for a MAGSAT anomaly, and the Liberian (West Africa) itabirites, for example, are drastically attenuated by minimal filtering applied to conventional aero-magnetic data (Behrendt and Wotorson, 1974).

But in relation to the ultimate objectives of the MAGSAT project (Langel et al., 1982a) the correlation may be significant for resource exploration because, although there certainly are exceptions, even a cursory examination shows that the correlation occaisionally is apparent outside of the West African and Amazonian cratons.

The area of the Bangui anomaly, for example ($\leq$ -12 nT at 5°N 18°W in Figure 7), includes only minor amounts of iron-formation, but for an induced crustal origin the anomaly requires a body

about 3 x 10^5 km^3 of susceptibility contrast at least 0.125 S.I., (Regan and Marsh, 1982), which approaches that of an iron-formation susceptibility contrast to surrounding non-magnetic rocks. A second example is the Kursk positive anomaly (MAGSAT $\Delta B > +15$ nT at 50°N 18°E); at the local magnetic inclination this intense anomaly implies a large positive magnetization-contrast source. The feature is dominant in early POGO maps (e.g., Regan et al., 1975, fig. 1) and has been frequently but only briefly mentioned in the satellite magnetic literature (e.g., Coles et al., 1982; Frey, 1982; Frey et al., 1983; Meyer et al., 1983; Olivier et al., 1983). Corresponding to the anomaly is an extremely iron-rich region, containing in 1970 almost 12% of the world's known iron-ore resources (Sokolov, 1970; United Nations, 1970, p.5), the protores of which are bedded iron-formations which were regionally metamorphosed at about 2700 and 2000 m.y. ago (Alexandrov, 1973; Plaksenko et al., 1973).

Despite these coincidences, the distribution of iron-rich regions in West Africa and northern South America can be only indirectly related to MAGSAT anomalies. It seems probable that both phenomena are present-day and surface manifestations of deep-seated and long-lived processes which have affected the geochemical differentiation of iron, and which may have produced other large scale inhomogeneities in the crust.

Long wavelength aeromagnetic surveys

We turn now briefly to examine regional aeromagnetic trends for information which could contribute to an understanding of

C-2

MAGSAT anomalies over the West African and Amazonian shield regions. Aeromagnetic coverage within the cratons is too sparse to allow compilation and upward continuation for comparison with MAGSAT anomalies, but analyses over the Liberian portion of the Man shield (Behrendt and Wotorson, 1974) and in Minas Gerais, Brazil (Gasparini et al., 1979; 1981), tend to confirm the suggestion by Strangway and Vogt (1970) that the longer wavelength (≥ 30 km) aeromagnetic anomalies over Precambrian shields in both continents are dominated by regional features which are related to the basement structure. Behrendt and Wotorson (1974), for example were just able to distinguish Proterozoic and Archean shield segments in their long wavelength aeromagnetic data. Green (1976) observed similar relationships in Project MAGNET data over central and southern Africa, and it is quite feasible that certain MAGSAT anomalies represent the integration and amalgamation of the same deep-seated basement contrasts in magnetic properties as are responsible for aeromagnetic anomalies.

This suggestion is supported by Wasilewski and Mayhew (1982) who summarized lower crustal intensities from a number of long wavelength aeromagnetic studies in different regions of the world as most frequently being in the range 1 - 10 $A.m.^{-1}$. The aeromagnetic study in the Superior province of the Canadian shield by Hall (1974) exemplifies this type of observation, although this particular area corresponds in the MAGSAT maps to a weak anomaly south of a strong positive anomaly which is associated with exposed high metamorphic grade rocks (Coles et al., 1982). Similarly, the lower crustal or upper mantle ≈ 5 $A.m.^{-1}$ sources below the Ukraine shield (Krutikhovskaya and Pashkevich, 1979; Krutikhovskaya et al., 1979) are swamped by the Kursk anomaly.

The implication is clearly that lower-crustal high magnetic intensity sources suggested by long wavelength aeromagnetic anomalies may be, but are not necessarily always, a cause of satellite-measured magnetic anomalies.

Geological and geophysical structural contrasts

In all probability it is contrasts in both chemistry and structure that are responsible for MAGSAT anomalies. What is known about the deep crustal structure of the two cratons, and what are the consequences for MAGSAT anomalies ?

Portions of the Man shield have surface heat flow and heat production values (Sass and Behrendt, 1980) typical of shield values throughout the world (c.f., Rao and Jessop, 1975), and there are magnetotelluric conductivity contrasts (Ritz, 1982; 1983) and teleseismic velocity contrasts (Briden et al., 1981; 1982) compatible with a shield crustal thickness of about 40 km. Otherwise, published heat flow or crustal thickness data for the West African and Amazonian cratons are very scarce, and it is not possible at the present time thoroughly to evaluate the MAGSAT anomalies in relation to structurally-based contrasts in magnetization due either to Moho or Curie isotherm topography.

However, considering the fundamental differences normally to be expected between oceanic and continental crust, some of the negative ΔX anomalies, for example the -4 nT anomaly over the Man shield, may partly be due to the continental-oceanic contrast in crustal thickness. But the Man shield shows contrasts to the marginal fold belt in conductivity and seismic velocity structure to depths of 200 km (Ritz, 1982; 1983; Briden et al., 1981; 1982), so that part of the MAGSAT anomaly probably also arises from structural contrasts within the continental lithosphere. If the deep crustal structure only were known in more detail there would

doubtless be other structural factors able to be invoked in explaining the MAGSAT anomalies.

Man shield gravity model of MAGSAT anomalies

The range of observations above widens rather than constrains the possible origins of West African and Amazonian craton MAGSAT anomalies, so that, although coincident gravity and magnetic anomalies need not necessarily be caused by the same source rocks, it is qualitatively useful further to examine gravity-magnetic relationships over the shield regions, and to ask whether the potential field anomalies jointly can be reconciled by a simple model.

As a basis for this there is a persistent and consistent mathematically inverse relationship between satellite-derived free air and ΔB magnetic anomalies over the United States, documented by von Frese et al. (1982a). Their models are for high magnetic inclinations, so that, because of the inclination dependence of magnetic anomalies, a mathematically direct relationship between free air and magnetic anomalies is implied for low magnetic inclinations. Neither of the Amazonian shields have definitive upward-continued ground-based free air anomalies (Hinze et al., 1982); in the GEM 8 and GEM 10 anomaly maps the Man shield corresponds to a positive free air and geoid anomaly, but this is opposite in sign to the ΔB and ΔX MAGSAT anomalies. The von Frese et al. (1982a) models clearly are not immediately applicable to the West African and Amazonian MAGSAT anomalies.

One way in which these observations may be partially reconciled depends on whether the resolution of density contrasts at depth is related to the different scales of the gravity surveys. Bronner et al. (1980) interpreted the positive isostatic anomalies of Louis (1970) as due to the combined effects of locally thinned upper crust and the relatively excess mass of iron-formations. The positive satellite-derived gravity anomaly which we have associated with the Man shield is from the high degree (> 12) maps, which are believed to represent diapiric sources between about 50 - 350 km depth (Kahn, 1971; Sclater et al., 1975; Marsh and Marsh, 1976).

The Bouguer anomalies in Figure 5 may originate almost anywhere, from the topographic surface on down, however the maximum uncertainty of even the predicted values in Africa is ± 20 mgal (Slettene et al., 1973), insufficient to change the sign of the Man shield anomaly, so that if any part is due to a feature other than topography the anomaly implies a density deficiency. In relation to the Brown and Girdler (1980) interpretation of African gravity, particularly the < -100 mgal Ahoggar uplift anomaly, sources for the ≈ -40 mgal Man shield anomaly are most reasonably at lower crustal or upper mantle depths. The combination of isostatic, free air and Bouguer anomalies suggests a crustal thickness of 37 ± 7 km according to relationships outlined by Woolard and Strange (1962), in general agreement with the ≈ 40 km thickness implied by magnetotelluric and teleseismic experiments of Briden et al. (1981; 1982) and Ritz (1982; 1983).

The simplest way in which the geology, gravity and magnetics can all be simultaneously reconciled is the following. Regional uplift, characteristic also of several other topographic swells in the African continent (Le Bas, 1971; Wilson, 1972; Burke and Wilson,

1972), and an upwelling mantle source are reflected in the positive geoid and free air anomalies; by the Woolard and Strange (1962) relationship the Bouguer anomaly reflects the density contrast at the seismic Moho; and the positive isostatic anomaly reflects a thinned and iron-rich upper crust (Bronner et al., 1980). Assuming after Wasilewski et al. (1979) that the mantle is non-magnetic, the seismic Moho is equivalent to the lower limit of magnetization in the low heat flow shield area. The negative MAGSAT anomaly thus represents the integration of 1) magnetization contrasts within upper crustal rocks, 2) magnetization contrasts in the lower crust (which was elevated closer to the topographic surface and into lower temperature regimes by uplift and consequent erosion), and 3) the magnetization contrast at the crust-mantle boundary.

Role of intrusions and serpentinization in the Man shield model

If the Moho is not a simple interface of constant and all-encompassing character then there may be other possible causes for the gravity and magnetic anomalies over the Man shield and elsewhere. For example, the lower crustal or upper mantle depth (≈40 km) density deficiency implied by the Man shield Bouguer anomaly, if real, may be further reconciled if alteration of the lithosphere due to intrusion and uplift is widespread.

The Man shield is a locus for Mesozoic and perhaps even earlier kimberlite volcanism (Figure 4; Haggerty, 1982) and basaltic volcanism also associated with continental rifting (Behrendt and Watorson, 1974). A myriad of very specific

tectonic events are generally invoked to assure upper mantle magmas an unimpeded path to the surface (e.g., Dawson, 1980), but in all probability many of these magmas may never reach the surface. The magnetic consequences of solidification at depth are twofold: the first is the crystallization of magnetite solid solutions in high modal proportions (Haggerty, 1975), and the second is metasomatism brought about by the release of dissolved volatiles, and their infiltration, laterally and vertically.

Oxides are sensitive to environmental temperature and oxygen fugacity, and the upper mantle is considered to be stratigraphically layered in oxidation-reduction potential (the lower crust and lithosphere are reduced whereas the upper crust and asthenosphere are relatively more oxidized (Haggerty and Tompkins, 1983)). Even though the process of serpentinization is one that involves extensive hydration, low oxidation states commonly exist (Moody, 1976), giving rise to magnetite and metal alloys (e.g., Haggerty, 1978 and references therein). Whether or not the alloys in serpentinites could contribute significantly to their magnetic properties (Haggerty, 1979; Wasilewski et al., 1979), the serpentinization of peridotites is frequently a process involving considerable volume expansion (Moody, 1976), and an increase in magnetic susceptibility due to the formation of magnetite, concommitant with a decrease in density (Hatherton, 1967; Saad, 1969; Henkel, 1976; Lienert and Wasilewski, 1979; Blakely and Page, 1980).

These factors could be related to the density and magnetic contrasts associated with the Man shield gravity and MAGSAT anomalies, but their significance has not been demonstrated on a shield-wide scale and is therefore relegated to being just another possible contribution to the overall lithologic contrast of the Man shield to its adjacent areas.

Significance of regional metamorphism

Perhaps the longest standing contrast related to the West African and Amazonian shields stems from their regional metamorphisms > 1500 m.y. ago. In multiply metamorphosed Precambrian shields, the magnetic oxide minerals of gneissic and granitic rocks have typically been subject to several episodes of reequilibration, and the long range magnetic characteristics of such metamorphic terrains are complex.

However, the crux of the magnetic anomaly - magnetic mineral interrelationship is that high Ti contents in mineral oxides decreases Curie points, magnetic susceptibility and coercivity, with high magnetic intensities becoming most readily possible upon oxidation, as reviewed by Hargraves and Bannerjee (1973). During regional metamorphism titanomagnetite in low grade (chlorite zone) rocks may be oxidized toward hematite, and Fe partitions into phyllosilicates at intermediate grades (Rumble, 1976). Titanium from surviving titanomagnetite is concentrated into "exsolved" and discrete ilmenite and partitioned into silicate phases at higher grades (Lidiak, 1974; Rumble, 1976; Hall et al., 1979). Very fine grained and magnetically stable iron oxides may "exsolve" from iron silicates (Haggerty, 1979), thus increasing magnetization intensity in high grade metamorphic rocks.

Magnetizations of granulite facies basic rocks are among the highest values measured from a variety of tectonic settings (Wasilewski and Mayhew, 1982), and Coles et al. (1982) note stronger MAGSAT and aeromagnetic anomalies over high metamorphic grade regions of the Canadian shield than exist over adjacent lower grade regions. The strongest negative MAGSAT anomalies over the West African and Amazonian cratons appear to correlate with the more ancient and higher metamorphic grade Archean cores of the shields. These complexes are dominated in the upper crust by granitic gneisses, granulites, migmatites and amphibolites, and their magnetic contrasts are not due to an exotic mineral-

ogy or to an intrinsic abundance of magnetic minerals, except locally where iron-formations are predominant.

In lower crustal metamorphic granulites from the Man shield, however, native iron has been identified, formed by reduction of ilmenite and as a decomposition product of almandine-pyrope garnet (Haggerty, 1983; Haggerty and Toft, 1984). As with metal alloys due to serpentinization, the magnetic significance of native iron in lower crustal or upper mantle rocks is possibly only local, but is certainly another factor contributing to magnetization contrasts associated with different degrees of metamorphism.

Numerical simulation of MAGSAT anomalies

We have suggested above that certain MAGSAT anomalies over West Africa and northern South America have sources which are reflected in the exposed geology and in gravity anomalies, but such a qualitative visually-based interpretation does not fully explain how the magnetic anomalies originate.

There are fundamental problems in seeking a more quantitative interpretation, however. Magnetic anomaly sources derived from inverse modelling are subject to a lack of unique solution, and, as reviewed in the introduction, these techniques sometimes give rise to solutions which are themselves anomalous in the magnetic intensities required. Forward modelling methods on the other hand, require at least some geologically-based geometrical constraints, but, as noted above in discussion, geological information on subsurface structure is almost completely lacking for the West African and Amazonian cratons. Furthermore, forward models require constraints on magnetization and magnetization contrasts, but the identification of native iron (Fe^{o}) in lower crustal rocks from the Man shield (Haggert , 1983; Haggerty and Toft, 1984)

contraindicates the usual modelling assumption that crustal magnetization depends significantly only on magnetite.

In view of these problems associated with traditional approaches to defining magnetic anomaly sources it is not possible at the present time to quantitatively and completely evaluate the sources of MAGSAT anomalies over the West African and Amazonian cratons. However, if there do exist geologically meaningful correlations between the MAGSAT anomalies and lithologic, metallogenic and gravity features then it should be possible to simulate the MAGSAT anomalies based on the hypothesized relationships.

To attempt this we made the following assumptions and rationalizations:

1) MAGSAT anomalies represent the integration of magnetization contrasts within the upper crust, the lower crust and the upper mantle;

2) magnetizations within these three gross structural levels contribute equally to the anomalous magnetic field at several hundred kilometers altitude;

3) upper crustal magnetization contrasts are due to lithological contrasts exposed at the Earth's surface;

4) gravity anomalies are lithologically related to coincident magnetic anomalies;

5) the most significant lower crustal magnetization contrasts are due to differences on crustal thickness and are reflected in the Bouguer anomaly field;

6) other lower crustal magnetization contrasts and contrasts within the upper mantle are reflected in free air anomalies; and

7) determining actual numerical values of magnetization contrasts is less significant than the identification of relatively stronger or weaker potential magnetic sources.

Following these assumptions, the six areally dominant types of exposed geological units of the cratons and their margins (Figures 2 and 4) were rank ordered in terms of more or less strongly magnetic according to observations adduced in the earlier stages of discussion and they were assigned small

dimensionless ranked numerical values; an allowance for rifts in tectonic settings other than a basin was inserted, and the continental shelf was assigned a small negative value. The total ranges of Bouguer and GEM 3 free air gravity anomalies within the cratons were then divided into six arbitrary but equal increment ranges and these were also assigned similar small dimensionless values (Table 1). For the geological units, it should be stressed that the assigned dimensionless numbers are not intended to be absolute values of magnetization or even magnetization contrasts, but simply represent a rationalized and empirically derived subjective rank ordering of apparent relative magnetic intensity. As regards the values assigned to the gravity ranges, these numbers are not intended to represent density contrasts directly equated to magnetization contrasts and are not meant to have a physical meaning other than to serve as a representation of the assumption that coincident gravity and magnetic anomalies are lithologically related.

To complete the simulation, the cratons and surrounding areas were gridded into 2° blocks ($\simeq$200 x 200 km, corresponding to the spatial resolution of MAGSAT) and each $2^{\circ} \times 2^{\circ}$ 'station' was assigned from Table 1 three values according to the dominant type of geology and the gravity anomalies within the block; the values at each station were then summed and the dimensionless results were contoured (Figure 10).

The simulated anomaly map bears a first order resemblance to the MAGSAT anomaly maps (Figures 6 and 7) in the general distribution of the most pronounced negative and positive peaks. Actual numerical values of the simulated anomalies are much less significant than the fact that the dominant simulated negative anomalies occur over the cratonic shield regions. But the positive MAGSAT anomalies are not so well reproduced by the simulation; for example,

in West Africa the Senegal Window and the Gourma aulacogen (Figures 2-4) appear as weak negative and positive simulated anomalies, respectively, in place of a single positive MAGSAT ΔB and ΔX anomaly over the Taoudeni basin. However, if the MAGSAT anomaly is caused primarily by an overlap of the positive cusps of negative anomalies over shields to the north and south, then the MAGSAT positive should not be expected to be reproduced by a simple simulation which takes no account of the effects of magnetic inclination.

To account for all features of the MAGSAT anomaly maps would require not only a full knowledge of the subsurface geology, and incorporation of the effects of magnetic inclination, but also would require a more precise definition throughout of crustal-anomaly versus core magnetic fields. Although not quantitative, the simulation has the merit that it is simple and it results in 'anomalies' which are reasonably close in character to the MAGSAT anomalies. Thus the simulation lends strong support to our qualitative interpretation of MAGSAT anomalies over the West African and Amazonian cratons as being due to a variety of superposed lithological and geophysical contrasts.

CONCLUSIONS

The basic geological relationships between and within the West African and Amazonian cratons have long been established and provide a coherent framework in which to evaluate recently available MAGSAT data. The two cratons have a similar geological structure, and the immediate conclusion is that the MGST (4/81) anomaly maps show similar features over both cratons.

The behaviour of the MAGSAT anomalies over these cratons is largely consistent

with the expected behaviour of induced magnetization. A qualitative combined analysis of ΔB and ΔX maps indicates that the dominant negative anomalies, which must be related at the present low geomagnetic inclinations to sources of positive magnetization contrast and normally-directed magnetization, are spatially associated with the Precambrian shield regions of both the West African and the Amazonian cratons.

Further comparison of ΔB, ΔX and RTP MAGSAT anomalies confirms the expectation that ΔX is less sensitive to inclination effects than is ΔB. The ΔX anomalies are more closely spatially related to the known upper crustal geology in that they more readily resolve the distinction between Archean and Proterozoic shield segments, particularly in West Africa, such that the older segments appear to be more strongly magnetized. A correlative example in support of the craton model is the São Luis craton, a small wedge of Proterozoic shield in northern South America with close affinities to the West African craton: it is apparent in the ΔX map as a minor relatively negative anomaly.

In relation to the pre-continental drift reconstruction employed to present the various data, profiles of ΔX constructed along the continental rejoin illustrate some of the problems involved in intercontinental comparisons of MAGSAT data, and suggest that, under circumstances where certain physical parameters of the anomaly sources are known, forcing similar profiles to agree with each other may help to establish a more realistic base level for the maps.

Concentrating on the Man shield of the West African craton, the superimposition of isostatic, Bouguer, free air and geoid anomalies indicates density contrasts within the upper crust, the lower crust and the upper mantle. These can be simply reconciled

with the positive magnetization-contrast source implied by the negative MAGSAT ΔX and ΔB anomalies if the lower crust is at least partially, and perhaps substantially, responsible both for the Bouguer anomalies and for the MAGSAT anomalies.

A simulation of MAGSAT anomalies based on the Man shield relationships and taking geological and gravity data as input generates 'anomalies' which are reasonably close in form to the MAGSAT anomalies over the West African and Amazonian cratons, particularly for the large negative anomalies indicative of regions of positive magnetization contrast. The simulation tends to confirm that the overriding causes of MAGSAT anomalies in these areas are crustal rocks, but the possible contribution of upper mantle sources in providing a background magnetization is also accounted as significant. The spatial coincidence of several negative MAGSAT anomalies with iron-rich regions of the upper crust may be more than just coincidence; in the simulation the iron-formations serve to localize the 'anomalies', but in reality both the magnetic anomalies and the iron ore deposits are most plausibly surficial manifestations of deep-seated geochemical differentiation and regional iron-enrichment.

This qualitative analysis of MAGSAT maps in relation to a synthesis of the geology and geophysics of the West African and Amazonian cratons has shown that these two large and now widely separated regions of the Earth are intimately portrayed in the MAGSAT vector anomaly maps. That the vector maps are amenable to such an interpretation confirms their overall accuracy, consistency and validity.

ACKNOWLEDGMENTS

This research was partially supported by NASA Contract NAS5-26414 (S.E.H. principal investigator) which is gratefully acknowledged. Constructive criticisms and thoughtful comments on an earlier version of the manuscript by five anonymous reviewers and by Dr. R. S. Carmichael, Dr. R. W. Girdler and Dr. D. A. Hastings substantially improved the paper. The continued support of Dr. Robert A. Langel, first as MAGSAT Chief Scientist and lately as guest associate editor for this issue of J.G.R.,was also instrumental. To all we express our sincere appreciation.

REFERENCES

Alexandrov, E.A., The Precambrian banded iron-formations of the Soviet Union, Econ. Geol., 68, 1035-1062, 1973.

Alldredge, L.R., Main field and recent secular variation, Rev. Geophys. and Space Phys., 21, 599-603, 1983a.

Alldredge, L.R., Core and crustal geomagnetic fields, J. Geophys. Res., 88, 1229-1234, 1983b.

Alldredge, L.R., Varying geomagnetic anomalies and secular variation, J. Geophys. Res., 88, 9443-9451, 1983c.

Almeida, F.F.M. de, and R. Black, Comparison structurale entre le N.E. du Bresil et l'Ouest African, Eos Trans. AGU, 53, 177, 1972.

Almeida, F.F.M. de, G. Amaral, U.G. Cordani, and K. Kawashita, The Precambrian evolution of the South American cratonic margin south of the Amazon River, in The Ocean Basins and Margins, vol. 1, The South Atlantic, edited by A.E.M. Nairn and F.G. Stehli, pp. 411-446, Plenum, New York, 1973.

Almeida, F.F.M. de, Y. Hasui, B.B. de Brito Neves, and R.A. Fuck, Brazilian structural provinces: an introduction, Earth Sci. Rev., 17, 1-30, 1981.

Alvarado, B., Iron ore deposits of South America, in Survey of World Iron Ore Resources, pp. 302-380, United Nations, New York, 1970.

Bardet, M.G., Géologie du diamant. Deuxième partie: Gisements de diamants d'Afrique, Memo. B.R.G.M., No. 83, Bureau de Recherche Géologique et Minières, Paris, 1974.

Basaltic Volcanism Study Project, Basaltic Volcanism on the Terrestrial Planets, 1286 pp., Plenum, New York, 1981.

Behrendt, J.C., and C.S. Wotorson, Geophysical surveys of Liberia with tectonic and geologic interpretations, U.S. Geol. Surv. Prof. Pap. 810, 1974.

Bessoles, B., Géologie de l'Afrique, vol. 1, Craton de l'Ouest Africain, Memo. B.R.G.M., No. 88, Bureau de Recherche Géologique et Minières, Paris, 1977.

Bessoles, B., Géologie de l'Afrique, vol. 2, La Chaine Panafricaine, Zone Mobile d'Afrique Centrale et Zone Mobile Soudanaise, Memo. B.R.G.M., No. 92, Bureau de Recherche Géologique et Minières, Paris, 1980.

Berbert, C.O., D.P. Svisero, A.N. Sial, and H.O.A. Meyer, Upper mantle material in the Brazilian Shield, Earth Sci. Rev., 17, 109-134, 1981.

Bigarella, J.J., Geology of the Amazon and Parnaiba basins, in The Ocean Basins and Margins, vol. 1, The South Atlantic, pp. 25-86, edited by A.E.M. Nairn and F.G. Stehli, Plenum, New York, 1973.

Black, R., Precambrian of West Africa, Episodes, 1980, 3-8, 1980.

Black, R., and M. Girod, Late Paleozoic to Recent igneous activity in West Africa and its relationship to basement structure, in African Magmatism and Tectonics, edited by T.N. Clifford and I.G. Gass, pp. 185-210, Oliver and Boyd, Edinburgh, 1970.

Black, R., R. Caby, A. Moussine-Pouchkine, R. Bayer, J.M. Bertrand, A.M. Boullier, J. Fabre, and A. Lesquer, Evidence for late Precambrian plate tectonics in West Africa, Nature, 278, 223-227, 1979.

Blakely, R.J., and N.J. Page, Interpretation of aeromagnetic data over the Josephine periodotite, Southwest Oregon, and implications for marine magnetic anomalies (abstract), Eos Trans. AGU, 61, 943, 1980.

Bosma, W., S.B. Kroonenberg, K. Maas, and E.W.F. de Roever, Igneous and metamorphic complexes of the Guiana shield in Suriname, Geol. en Mijnbouw, 62, 241-254, 1983.

Breville, G.L., C.W. Beierle, J.R. Sanders, J.T. Voss, and L.E. Wilcox, A Bouguer gravity anomaly map of South America, DMAAC Tech. Pap. No. 73-002, Defence Mapping Agency, St. Louis, 1973.

Briden, J.C., D.N. Whitcombe, G.W. Stuart, J.D. Fairhead, C. Dorbath, and L. Dorbath, Depth of geological contrast across the West African craton margin, Nature, 292, 123-128, 1981.

Briden, J.C., R.F. Mereu, and D.N. Whitcombe, A teleseismic study of the West African craton margin in Senegal: P-wave slowness and azimuth anomalies, Geophys. J. Roy. Astron. Soc., 71, 793-808, 1982.

Bronner, G., J. Roussel, R. Trompette, and N. Clauer, Genesis and geodynamic evolution of the Taoudeni cratonic basin (Upper Precambrian and Paleozoic), West Africa, in Geodynamics of Plate Interiors, Geodynamics Series, vol. 1, edited by A.W. Bally, P.L. Bender, T.R. McGetchin, and R.I. Walcott, pp. 81-90, AGU, Washington, D.C., 1980.

Brown, C., and R.W. Girdler, Interpretation of African gravity and its implication for the breakup of continents, J. Geophys. Res., 85, 6443-6455, 1980.

Brown, C., R.W. Girdler, and R.G.B. Renner, A gravity traverse across northern Africa, J. Geophys. Res., 85, 6436-6442, 1980.

Bullard, E.C., J.E. Everett, and A.G. Smith, The fit of the continents around the Atlantic, Philos. Trans. Roy. Soc. London, Ser. A, 258, 41-51, 1965.

Burke, K., Development of graben associated with the initial ruptures of the Atlantic Ocean, Tectonophysics, 36, 93-112, 1976.

Burke, K., and A.J. Whiteman, Uplift, rifting and the break-up of Africa, in Implications of Continental Drift to the Earth Sciences, vol. 2, edited by D.H. Tarling and S.K. Runcorn, pp. 735-755, Academic, New York, 1973.

Burke, K., and J.T. Wilson, Is the African plate stationary?, Nature, 239, 387-390, 1972.

Burke, K., J.F. Dewey, and W.S.F. Kidd, World distribution of sutures - the sites of former oceans, Tectonophysics, 40, 69-100, 1977.

Cain, J.C., D.R. Schmitz, and L. Muth, Small-scale features in the Earth's magnetic field observed by MAGSAT, J. Geophys. Res., 89, 1070-1076, 1984.

Carle, H.M., and C.G.A. Harrison, A problem in representing the core magnetic field of the Earth using spherical harmonics, Geophys. Res. Lett., 9, 265-268, 1982.

Chiron, J.C., Etude géologique de la chaine des Mauritanides entre le parallel de Moudjéria et le fleuve Senegal (Mauritanie), Memo. B.R.G.M., No. 84, Bureau de Recherches Géologique et Minières, Paris, 1974.

Choubert, B., Les Guyano-éburneides de l'Amerique du Sud et de l'Afrique occidentale (Essais de comparaison géologique), Bulletin du B.R.G.M. (ser. 2) Section 4, 4, Bureau de Recherches Géologique et Minières, Orleans, 1969.

Choubert, B., Le Precambrian des Guyanes, Memo. B.R.G.M., No. 81, Bureau de Recherches Géologique et Minières, Paris, 1974.

Choubert, G., and A. Faure-Muret, Chaînes plissees du precambrian superieur, in Tectonique de l'Afrique, pp. 295-349, UNESCO, Paris, 1971.

Choubert, G. A. Faure-Muret, and D.A. Andrews-Jones, Craton de l'Afrique occidentale, in Tectonique de l'Afrique, pp. 161-209, UNESCO, Paris, 1971.

Clifford, T.N., The structural framework of Africa, in African Magmatism and Tectonics, edited by T.N. Clifford and I.G. Gass, pp. 1-26, Oliver and Boyd, Edinburgh, 1970.

Coles, R.L., G.V. Haines, G. Jansen van Beek, A. Nandi, and J.K. Walker, Magnetic anomaly maps from 40°N to 83°N derived from MAGSAT satellite data, Geophys. Res. Lett., 9 281-284, 1982.

Dawson, J.B., Kimberlites and Their Xenoliths, 252 pp., Springer-Verlag, New York, 1980.

Dillon, W.P., and J.M.A. Soughy, Geology of West Africa and Canary and Cape

Verde islands, in The Ocean Basins and Margins, vol. 2, The North Atlantic, edited by A.E.M. Nairn and F.G. Stehli, pp. 315-390, Plenum, New York, 1974.

Dobrin, M., Introduction to Geophysical Prospecting, 3rd edition, 630 pp., McGraw-Hill, New York, 1976.

Dorr, J.V.N., II, Iron-formation in South America, Econ. Geol. 68, 1005-1022, 1973a.

Dorr, J.V.N., II, Iron-formation and associated manganese in Brazil, in Genesis of Precambrian Iron and Manganese Deposits, Proc. Kiev Symp., 1970, Earth Sci. Ser., vol. 9, pp. 105-114, UNESCO, Paris, 1973b.

Dorr, J.V.N., II, P.W. Guild, and A.L.M. Barbosa, Origin of the Brazilian iron ores, in Symp. Gisements Fer Monde, pp. 286-310, Internat. Geol. Congr., Algiers, 1952.

Fountain, D.M., and M.H. Salisbury, Exposed cross-sections through the continental crust: implications for crustal structure, petrology, and evolution, Earth Planet. Sci. Lett., 56, 263-277, 1981.

Frey, H.V., Tectonic boundaries: rift and suture maps, in A Geophysical Atlas for the Interpretation of Satellite-Derived Data, NASA Tech. Memo., 79722, edited by P.D. Lowman, Jnr. and H.V. Frey, pp. 31-34, NASA, Greenbelt, MD, 1979.

Frey, H.V., MAGSAT scalar anomaly distribution: the global perspective, Geophys. Res. Lett., 9, 277-280, 1982.

Frey, H.V., R.A. Langel, and W.M. Davis, Satellite-derived magnetic anomaly maps, in A Geophysical Atlas for the Interpretation of Satellite-Derived Data, NASA Tech. Memo., 79722, edited by P.D. Lowman, Jnr. and H.V. Frey, pp. 15-20, NASA, Greenbelt, MD, 1979.

Frey, H.V., R.A. Langel, G. Mead, and K. Brown, POGO and Pangaea, Tectonophysics, 95, 181-189, 1983.

Galdéano, A., Les mesures magnetiques du satellite MAGSAT et la dérive des

continents, C.R. Acad. Sciences Paris, Serie II, 293, 161-164, 1981.

Galdéano, A., Acquisition of long wavelength magnetic anomalies pre-dates continental drift, Phys. Earth Planet. Int., 32, 289-292, 1983.

Galliher, S.C., and M.A. Mayhew, On the possibility of detecting large-scale crustal remanent magnetization with MAGSAT vector magnetic anomaly data, Geophys. Res. Lett., 9, 325-328, 1983.

Gasparini, P., M.S.M. Mantovani, G. Corrado, and A. Rapolla, Depth of Curie temperature in continental shields: a compositional boundary?, Nature, 278, 845-846, 1979.

Gasparini, P., M.S.M. Mantovani, and W. Shukowski, Interpreation of long wavelength anomalies, in The Solution of the Inverse Geophysical Problem in Geophysical Interpretation, pp. 231-255, edited by R. Cassinis, Plenum, New York, 1981.

Gibbs, A.K., and C.N. Barron, The Guiana shield reviewed, Episodes, 1983, 7-14, 1983.

Goodwin, A.M., Plate tectonics and evolution of Precambrian crust, in Implications of Continental Drift to the Earth Sciences, vol. 2, edited by D.H. Tarling and S.K. Runcorn, pp. 1047-1069, Academic, New York, 1973.

Grant, N.K., Orogeny and reactivation of the west and southeast of the West African craton, in The Ocean Basins and Margins, vol. 1, The South Atlantic, edited by A.E.M. Nairn and F.G. Stehli, pp. 447-492, Plenum, New York, 1973.

Green, A.G., Interpretation of Project MAGNET aeromagnetic profiles across Africa, Geophys. J. Roy. Astron. Soc., 44, 203-228, 1976.

Gross, G.A., Geology of iron deposits, in Canada, vol. 1, General geology and evaluation of iron deposits, Geol. Surv. Canada, Econ. Geol. Report No. 22, 1965.

Gross, G.A., Nature and occurrence of iron ore deposits, in Survey of World

Iron Ore Resources, pp. 13-31, United Nations, New York, 1970.

Gross, G. A., The depositional environment of principal types of Precambrian iron-formations, in Genesis of Precambrian Iron and Manganese Deposits, Proc. Kiev Symp., 1970, Earth Sci. Ser., vol. 9, pp. 15-22, UNESCO, Paris, 1973.

Gruss, H., Itabirite iron ores of the Liberian and Guyana shields, in Genesis of Precambrian Iron and Manganese Deposits, Proc. Kiev Symp., 1970, Earth Sci. Ser., vol. 9, pp. 335-360, UNESCO, Paris, 1973.

Haggerty, S.E., The chemistry and genesis of opaque minerals in kimberlites, Phys. Chem. Earth, 9, 295-307, 1975.

Haggerty, S.E., Mineralogical constraints on Curie isotherms in deep crustal magnetic anomalies, Geophys. Res. Lett., 5, 105-108, 1978.

Haggerty, S.E., The aeromagnetic mineralogy of igneous rocks, Can. J. Earth Sci., 16, 1281-1293, 1979.

Haggerty, S.E., Kimberlites in western Liberia: an overview of the geological setting in a plate tectonic framework, J. Geophys. Res., 87, 10,811-10,826, 1982.

Haggerty, S.E., Oxide-silicate reactions in lower crustal granulites from Liberia, West Africa (abstract), G.S.A. Abstracts with programs, 15, #6, 589, 1983.

Haggerty, S.E., and P.B. Toft, Native iron in the lower continental crust: petrological and geophysical implications, submitted to Science, August, 1984.

Haggerty, S.E., and L. A. Tompkins, Redox state of the Earth's upper mantle from kimberlitic ilmenites, Nature, 303, 295-300, 1983.

Hall, D.H., Long-wavelength aeromagnetic anomalies and deep crustal magnetization in Manitoba and northwestern Ontario, Canada, J. Geophys., 40, 403-430, 1974.

Hall, D.H., R.L. Coles, and J.M. Hall, The distribution of surface magnetization in the English River and Kenora subprovinces of the Archean shield in Manitoba and Ontario, Can J. Earth Sci., 16, 1764-1777, 1979.

Hargraves, R.B., and S.K. Banerjee, Theory and nature of magnetism in rocks, Ann. Rev. Earth Planet Sci., vol. 1, edited by F.A. Donath, F.G. Stehli, and S.W. Weatherill, pp. 269-296, Ann. Rev. Inc., California, 1973.

Harrison, C.G.A., Magnetic anomalies, Rev. Geophys. and Space Phys., 21, 634-643, 1983.

Hastings, D.A., Preliminary correlations of MAGSAT anomalies with tectonic features of Africa, Geophys. Res. Lett., 9, 303-306, 1982.

Hastings, D.A., An updated Bouguer anomaly map of south-central West Africa, Geophysics, 48, 1120-1128, 1983.

Hatherton, T., A geophysical study of the Nelson-Cook Straight region, New Zealand, N. Z. J. Geol. and Geophys., 10, 1330-1347, 1967.

Henkel, H., Studies of density and magnetic properties of rocks from northern Sweden, Pure Appl. Geophys., 114, 235-249, 1976.

Herz, N., Timing of spreading in the South Atlantic: information from Brazilian alkalic rocks, Geol. Soc. Amer. Bull., 88, 101-112, 1977.

Hinze, W.J., R.R.B. von Frese, M.B. Longacre, L.W. Braile, E.G. Lidiak, and G.R. Keller, Regional magnetic and gravity anomalies of South America, Geophys. Res. Lett., 9, 314-317, 1982.

Hurley, P.M., On the origin of 450 ± 200 m.y. orogenic belts, in Implications of Continental Drift to the Earth Sciences, vol. 2, edited by D.H. Tarling and S.K. Runcorn, pp. 1083-1089, Academic, New York, 1973.

Hurley, P.M. and J.R. Rand, Outline of Precambrian chronology in lands bordering the South Atlantic, exclusive of Brazil, in The Ocean Basins

and Margins, vol. 1, The South Atlantic, edited by A.E.M. Nairn and F.G. Stehli, pp. 391-410, Plenum, New York, 1973.

Hurley, P.M., F.F.M. de Almeida, G.C. Melcher, U.G. Cordani, J.R. Rand, K. Kawashita, P. Vandoros, W.H. Pinson, Jr., and H.W. Fairbairn, Test of continental drift by comparison of radiometric ages, Science, 157, 495-500, 1967.

Kahn, M.A., Some geophysical implications of the satellite-determined geogravity field, Geophys. J. Roy. Astron. Soc., 23, 15-43, 1971.

Klumpar, D.M., and D.M. Greer, A technique for modelling the magnetic perturbations produced by field-aligned current systems, Geophys. Res. Lett., 9, 361-364, 1982.

Kröner, A., Precambrian mobile belts of southern and eastern Africa - ancient sutures or sites of ensialic mobility? A case for crustal evolution toward plate tectonics, Tectonophysics, 40, 101-136, 1977.

Kroonenberg, S.B., A Grenvillean granulite belt in the Columbian Andes and its relation to the Guiana shield, Geol. en Mijnbouw, 61, 325-333, 1982.

Krutikhovskaya, Z.A., and I.K. Pashkevich, Long-wavelength magnetic anomalies as a source of information about deep crustal structure, J. Geophys., 46, 301-317, 1979.

Krutikhovskaya, Z.A., I.M. Silina, N.M. Bondareva, and S.M. Podolyanko, Relation of magnetic properties of the rocks of the Ukranian Shield to their composition and metamorphism, Can. J. Earth Sci., 16, 984-991, 1979.

Langel, R.A., and R.H. Estes, A geomagnetic field spectrum, Geophys. Res. Lett., 9. 250-253, 1982.

Langel, R.A., and H. Frey, A reduced-to-pole satellite anomaly map of the world and its relationship to global tectonics (abstract), Eos Trans. AGU, 64, 214, 1983.

Langel, R.A., and L. Thorning, A satellite magnetic anomaly map of Greenland,

Geophys. J. Roy. Astron. Soc., 71, 599-612, 1982.

Langel, R.A., R.L. Coles, and M.A. Mayhew, Comparisons of magnetic anomalies of lithospheric origin measured by satellite and airborne magnetometers over western Canada, Can. J. Earth Sci., 17, 876-887, 1980a.

Langel, R.A., R.H. Estes, G.D. Mead, E.B. Fabiano, and E.R. Lancaster, Initial geomagnetic field model from MAGSAT vector data, Geophys. Res. Lett., 7, 793-796, 1980b.

Langel, R.A., G.D. Mead, and R.H. Estes, Spherical harmonic models of the cores field, in NASA Earth Survey Applications Div., Res. Report - 1979, NASA Tech. Memo., 80642, edited by L. Carpenter, pp. 2-4 - 2-23, NASA, Greenbelt, MD, 1980c.

Langel, R.A., G. Ousley, J. Berbert, J. Morphy, and M. Settle, The MAGSAT mission, Geophys. Res. Lett., 9, 243-245, 1982a.

Langel, R.A., J.D. Phillips, and R.J. Horner, Initial scalar magnetic anomaly map from MAGSAT, Geophys. Res. Lett., 9, 269-272, 1982b.

Langel, R.A., C.C. Schnetzler, J.D. Phillips, and R.J. Horner, Initial vector magnetic anomaly map from MAGSAT, Geophys. Res. Lett., 9, 273-276, 1982c.

Le Bas, M.J., Per-alkaline volcanism, crustal swelling and rifting, Nature Phys. Sci., 230, 85-86, 1971.

Leblanc, M., A Proterozoic ocean crust at Bou Azzer, Nature, 261, 34-35, 1976.

Lesquer, A., and A. Moussine-Pouchkine, Les anomalies gravimetrique de la boucle du Niger. Leur significance dans le cadre de l'orogenèse panafricaine, Can. J. Earth Sci., 17, 1538-1545, 1980.

Lidiak, E.G., Magnetic characteristics of some Precambrian basement rocks, J. Geophys., 40, 549-564, 1974.

Lienert, B.R., and P.J. Wasilewski, A magnetic study of the serpentinization process at Burro Mountain, California, Earth Planet. Sci. Lett., 43,

406-416, 1979.

Louis, P., Contribution géophysique à la connaissance géologique du bassin du Lac Tchad, Memo. ORSTOM, No. 42, ORSTOM, Paris, 1970.

Lowman, P.D., Jnr., Global tectonic and volcanic activity maps, in A Geophysical Atlas for the Interpretation of Satellite-Derived Data, NASA Tech. Memo., 79722, edited by P.D. Lowman, Jnr. and H.V. Frey, pp. 35-42, NASA, Greenbelt, MD, 1979.

Machens, E., The geological history of the marginal basins along the north shore of the Gulf of Guinea, in The Ocean Basins and Margins, vol. 1, The South Atlantic, edited by A.E.M. Nairn and F.G. Stehli, pp. 351-390, Plenum, New York, 1973.

Marelle, A., and M.A. Abdullah, Iron ore deposits of Africa, in Survey of World Iron Ore Resources, pp. 62-101, United Nations, New York, 1970.

Marsh, B.D., and J.G. Marsh, On global gravity anomalies and two-scale mantle convection, J. Geophys. Res., 81, 5267-5280, 1976.

Marsh, J.G., Satellite-derived gravity maps, in A Geophysical Atlas for the Interpretation of Satellite-Derived Data, NASA Tech. Memo., 79722, edited by P.D. Lowman, Jnr. and H.V. Frey, pp. 9-14, NASA, Greenbelt, MD, 1979.

Marsh, J.S., Relationships between transform directions and alkaline igneous rock lineaments in Africa and South America, Earth Planet. Sci. Lett., 18, 317-323, 1973.

Martin, A.K., C.J.H. Hartnady, and S.W. Goodlad, A revised fit of South America and south central Africa, Earth Planet. Sci. Lett., 54, 293-305, 1981.

Mayhew, M.A., Inversion of satellite magnetic anomaly data, J. Geophys., 45, 119-128, 1979.

Mayhew, M.A., An equivalent layer magnetization model for the United States derived from satellite altitude magnetic anomalies, J. Geophys. Res.,

87, 4837-4845, 1982a.

Mayhew, M.A., Application of satellite magnetic anomaly data to Curie isotherm mapping, J. Geophys. Res., 87, 4846-4854, 1982b.

Mayhew, M.A., and S.C. Galliher, An equivalent layer magnetization model for the United States derived from MAGSAT data, Geophys. Res. Lett., 9, 311-313, 1982.

Mayhew, M.A., B.D. Johnson, and R.A. Langel, An equivalent source model of the satellite-altitude magnetic anomaly field over Australia, Earth Planet. Sci. Lett., 51, 189-198, 1980.

McElhinny, M.W., and M.O. McWilliams, Precambrian geodynamics - a paleomagnetic view, Tectonophysics, 40, 137-160, 1977.

McLeod, M.G., Crustal geomagnetic field: two-dimensional intermediate - wavelength spatial power spectra, Phys. Earth Planet. Inter., 31, 132-144, 1983.

McWilliams, M.O., and A. Krőner, Paleomagnetism and tectonic evolution of the Pan-African Damara Belt, Southern Africa, J. Geophys. Res, 86, 5147-5162, 1981.

Moody, J.B., Serpentinization: a review, Lithos, 9, 125-138, 1976.

Moore, A.E., Controls of post-Gondwanaland alkaline volcanism in southern Africa, Earth Planet. Sci. Lett., 31, 291-296, 1976.

Nairn, A.E.M., and F.G. Stehli, A model for the South Atlantic, in The Ocean Basins and Margins, vol. 1, The South Atlantic, pp. 1-24, edited by A.E.M. Nairn and F.G. Stehli, Plenum, New York, 1973.

Olivier, R., W.J. Hinze, and R.R.B. von Frese, Reduced to pole long-wavelength magnetic anomalies of Africa and Europe (abstract), Eos Trans. AGU, 64, 214, 1983.

Orlin, H. (ed.), Gravity Anomalies: Unsurveyed Areas, Geophys. Mono. Ser., vol. 9, 142 pp., AGU, Washington, D.C., 1966.

Park, C.F., A magnetite "flow" in northern Chile, Econ. Geol., 56, 431-441, 1961.

Plaksenko, N.A., I.K. Koval, and I.N. Shchogolev, Precambrian ferruginous-siliceous formations associated with the Kursk magnetic anomaly, in Genesis of Precambrian Iron and Manganese Deposits, Proc. Kiev Symp., 1970, Earth Sci. Ser., vol. 9, pp. 84-94, UNESCO, Paris, 1973.

Priem, H.N.A., P.A.M. Andriessen, N.A.I.M. Boelrijk, H. de Boorder, H.E. Hebeda, A. Huguett, E.A. Th. Verdurmen, and R.H. Verschure, Geochronology of the Precambrian in the Amazonas Region of southeastern Columbia (western Guiana Shield), Geol. Mijnbouw., 61, 229-242, 1982.

Rabinowitz, P.D., and J. LaBrecque, The Mesozoic South Atlantic Ocean and evolution of its continental margins, J. Geophys. Res., 84, 5973-6002, 1979.

Rao, R.U.M., and A.M. Jessop, A comparison of the thermal character of shields, Can. J. Earth Sci., 12, 347-360, 1975.

Regan, R.D., and B.D. Marsh, The Bangui magnetic anomaly: its geological origin, J. Geophys. Res., 87, 1107-1120, 1982.

Regan, R.D., J.C. Cain, and W.M. Davis, A global magnetic anomaly map, J. Geophys. Res., 80 794-802, 1975.

Ritz, M., Etude régionale magnéto-tellurique des structures de la conductivité électrique sur la bordure occidentale de craton ouest African en Republique du Sénégal, Can. J. Earth Sci., 19, 1408-1416, 1982.

Ritz, M., Use of the magnetotelluric method for a better understanding of the West African shield, J. Geophys. Res., 88, 10,625-10,634, 1983.

Rumble, D., Oxide minerals in metamorphic rocks, in Oxide Minerals, Min. Soc. Amer. short course notes vol. 3, edited by D. Rumble, pp. R1-R24, Min. Soc. Amer., Washington, D.C., 1976.

Saad, A.H., Magnetic properties of ultramafic rocks taken from Red Mountain, California, Geophysics, 34, 974-987, 1969.

Sailor, R.V., A.R. Lazarewicz and R.F. Brammer, Spatial resolution and repeatability of MAGSAT crustal anomaly data over the Indian Ocean, Geophys. Res. Lett., 9, 289-292, 1982.

Sass, J.H., and J.C. Behrendt, Heat flow from the Liberian Precambrian shield J. Geophys. Res., 85, 3159-3162, 1980.

Schnetzler, C.C., and R.J. Allenby, Estimation of lower crustal magnetization from satellite derived anomaly field, Tectonophysics, 93, 33-45, 1983.

Sclater, J.G., L.A. Lawver, and B. Parsons, Comparison of long wavelength residual elevation and free air gravity anomalies in the North Atlantic and possible implications for the thickness of the lithospheric plate, J. Geophys. Res., 80, 1031-1052, 1975.

Sclater, J.G., S. Hellinger, and C. Tapscott, The paleobathymetry of the Atlantic Ocean from the Jurassic to the Present, J. Geol., 85, 509-552, 1977.

Sclater, J.G., B. Parsons, and C. Jaupart, Oceans and continents: similarities and differences in the mechanisms of heat loss, J. Geophys. Res., 86, 11,535-11,552, 1981.

Slettene, R.L., L.E. Wilcox, R.S. Blouse, and J.R. Sanders, A Bouguer gravity anomaly map of Africa, DMAAC Tech. Pap. No. 73-3, Defence Mapping Agency, St. Louis, MO, 1973.

Smith, A.G., and A. Hallam, The fit of the Southern continents, Nature, 225, 139-144, 1970.

Sokolov, G.A., Iron ore deposits of the Union of Soviet Socialist Republics, in Survey of World Iron Ore Resources, pp. 381-410, United Nations, New York, 1970.

Strangway, D.W., and P.R. Vogt, Aeromagnetic tests for continental drift in Africa and South America, Earth Planet. Sci. Lett., 7, 429-435, 1970.

Taylor, P.T., A.F. Schanzle, T.L. Jones, R.A. Langel, and W.D. Kahn, Influence of gravity field uncertainties on the results from POGO and MAGSAT geomagnetic surveys, Geophys. Res. Lett., 8, 1246-1248, 1981.

Taylor, P.T., T. Keating, W.D. Kahn, R.A. Langel, D.E. Smith, and C.C. Schnetzler, GRM: Observing the terrestrial gravity and magnetic fields in the 1990's, Eos Trans. AGU, 64, 609-611, 1983.

Tolbert, G.E., J.W. Tremaine, G.C. Melcher, and G.B. Gomes, Geology and iron-ore deposits of Serra dos Carajas, Para, Brésil, in Genesis of Precambrian Iron and Manganese Deposits, Proc. Kiev Symp., 1970, Earth Sci. Ser., vol. 9, pp. 271-280, UNESCO, Paris. 1973.

Torquato, J.R., and U.G. Cordani, Brazil-Africa geological links, Earth Sci. Rev., 17, 155-176, 1981.

Trombka, A.P., and P.D. Lowman, Jnr., Recent volcanic activity map, in A Geophysical Atlas for the Interpretation of Satellite-Derived Data, NASA Tech. Memo., 79722, edited by P.D. Lowman, Jnr. and H.V. Frey, pp. 27-30, NASA, Greenbelt, MD, 1979.

United Nations, Survey of World Iron Ore Resources, U.N. Publ. No. E.69. II. C.4, United Nations, New York 1970.

von Frese, R.R.B., W.J. Hinze, and L.W. Braile, Spherical Earth gravity and magnetic analysis by equivalent point source inversion, Earth Planet. Sci. Lett., 53, 69-83, 1981a.

von Frese, R.R.B., W.J. Hinze, L.W. Braile, and A.J. Luca, Spherical-Earth gravity and magnetic anomaly modeling by Gauss-Legendre quadrature integration, J. Geophys., 49, 234-242, 1981b.

von Frese, R.R.B., W.J. Hinze, L.W. Braile, Regional North American gravity and magnetic anomaly correlations, Geophys. J. Roy. Astron. Soc., 69, 745-761, 1982a.

von Frese, R.R.B., W.J. Hinze, J.L. Sexton and L.W. Braile, Verification of the crustal component in satellite magnetic data, Geophys. Res. Lett.,

9, 293-295, 1982b.

Wagner, C.A., F.J. Lerch, J.E. Brownd, and J.A. Richardson, Improvement in the geopotential derived from satellite and surface data (GEM 7 and 8), J. Geophys. Res., 82, 901-914, 1977.

Wasilewski, P., and M.A. Mayhew, Crustal xenolith magnetic properties and long wavelength anomaly source requirements, Geophys. Res. Lett., 9, 325-328, 1982.

Wasilewski, P., H.H. Thomas, and M.A. Mayhew, The Moho as a magnetic boundary, Geophys. Res. Let., 6, 541-544, 1979.

Wernick, E., The Archean of Brazil, Earth Sci. Rev., 17, 31-48, 1981.

Wilcox, L., Automated library system and services of DMA (Regional gravity and elevation maps of South America), in Geophysics in the Americas, Earth Physics Branch Publication, vol. 46, #3, edited by J.G. Tanner and M.R. Dence, pp. 114-117 (maps in sleeve), Energy, Mines and Resources, Ottawa, 1977.

Wilson, J.T., New insights into old shields, Tectonomphysics, 13, 73-94, 1972.

Won, I.J., and K.H. Son, A preliminary comparison of the MAGSAT data and aeromagnetic data in the continental U.S., Geophys. Res. Lett., 9, 296-298, 1982.

Woolard, G.P., and W.E. Strange, Gravity anomalies and the crust of the Earth in the Pacific Basin, in The Crust of the Pacific Basin, Geophys. Monogr. Ser., vol. 6, edited by G.A. MacDonald and K. Kuno, pp. 60-80 AGU, Washington, D.C., 1962.

FIGURE CAPTIONS

Figure 1. The location map identifies the West African (1) and the Amazonian (2) cratons, and outlines the areas enlarged in subsequent Figures. The other cratons are: 3 = São Luis, 4 = São Fransisco, 5 = Zaire.

Figure 2. Generalized regional geology (based on de Almeida and Black (1972) and Torquato and Cordani (1981) and other references in the text) assembled on the Bullard et al. (1965) reconstruction. The 500 fathom isobath is omitted in areas of overlap. Two generations of shield rocks are identified, along with fold belts and basins.

Figure 3. The location map identifies the Man and Reguibat shields of the West African craton and the Guyana and Guapore shields of the Amazonian craton, along with other locations referred to in the text (M.F.B. = Mauritanide fold belt; G.A. = Gourma aulacogen; S.W. = Senegal window; ROR. = Roraima sediments) and the two major basins, the Taoudeni and the Amazon.

Figure 4. The tectono-metallogenic map indicates the major graben and sutures (Burke and Whiteman, 1973; Burke, 1976; Burke et al., 1977; Frey, 1979), the Gourma aulacogen (Lesquer and Moussine-Pouchkine, 1980), thrust faults (Lowman, 1979), recently active (<1 m.y.) volcanic structures (Trombka and Lowman, 1979), kimberlites as both dikes and pipes (Bardet, 1973; Dawson, 1980), and iron ore resources known in 1970 (Marelle and Abdullah, 1970; Alvorado, 1970).

Figure 5. Bouguer gravity anomalies for West Africa (Slettene et al., 1973) and South America (Wilcox, 1976), from ground based observations supplemented by predicted values. Shield areas of the two major cratons show predominantly strong negative anomalies.

Figure 6. Scalar, or total field, (ΔB) MAGSAT (MGST 4/81) anomalies at about 400 km altitude (Langel et al., 1982b), and magnetic inclination contours. At inclinations $\leq 35^{\circ}$ dominantly negative anomalies are induced by positive magnetization contrast sources. Shield areas of both West African and Amazonian cratons underlie predominantly negative anomalies. The Bangui anomaly ($\leq$ -12 nT) is in Africa at about 15° south inclination.

Figure 7. North-south horizontal vector (ΔX) MAGSAT (MGST 4/81) anomalies (Langel et al., 1982c), which are similar in form to the ΔB anomalies but more closely spatially related to the outcropping shield geology.

Figure 8. MAGSAT anomaly profiles across northern South America, taken roughly perpendicular to inclination contours and through equivalent peaks of the ΔB and ΔX maps (Figures 6 and 7) and the reduced-to-pole (RTP) ΔB map by Hinze et al. (1982). Relative to the RTP profile, ΔX is less sensitive to magnetic inclination than is ΔB. (reversed scale on RTP profile)

Figure 9. MAGSAT ΔX profiles of Africa and South America taken along the Bullard et al. (1965) continental rejoin. Arrows

at each station are proportional in length to the (1980) main field strength, and indicate apparent inclinations in the profiled planes.

Figure 10. Simulated MAGSAT anomalies. Contour values are dimensionless.

TABLE CAPTION

Table 1. Input values for numerical simulation of MAGSAT anomalies.

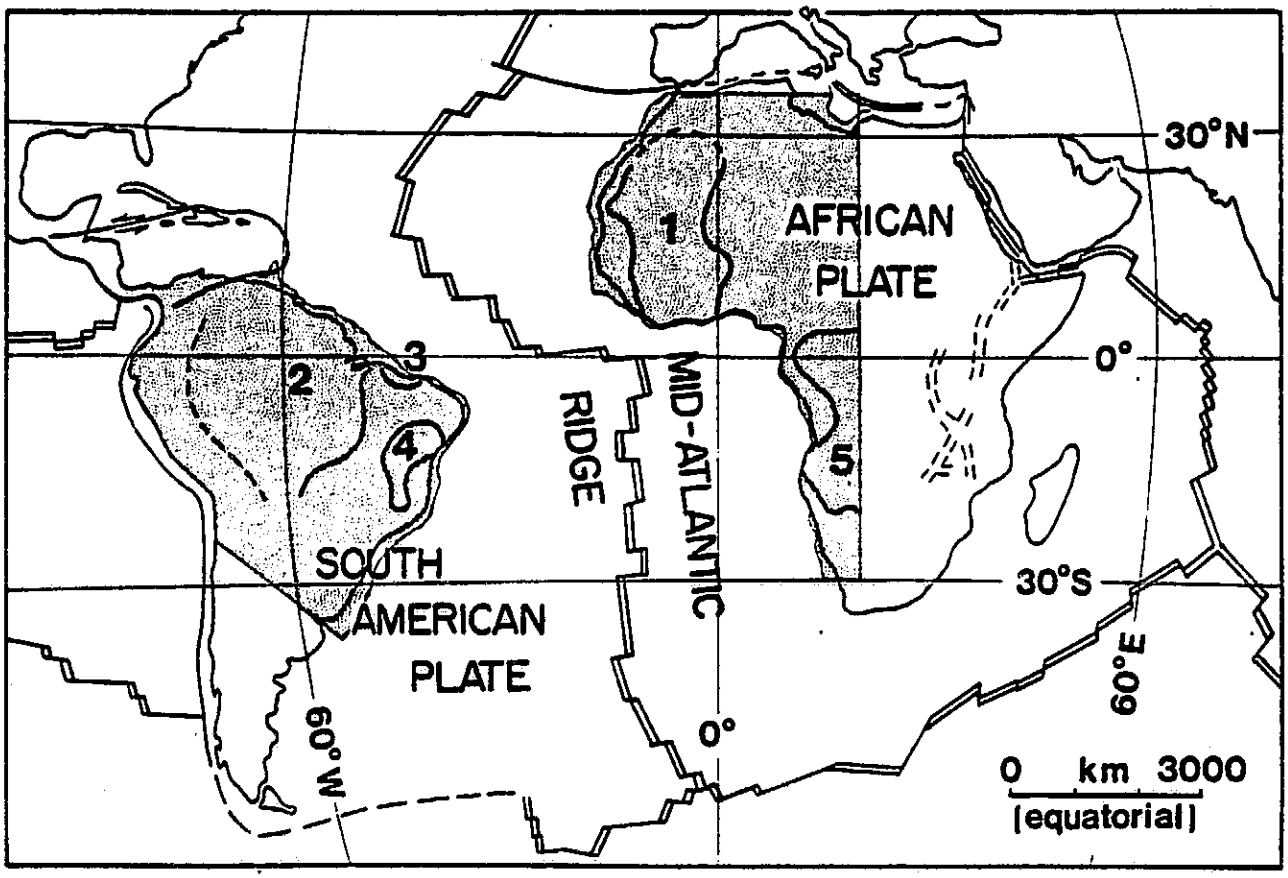

FIG. 1

ORIGINAL PAGE IS
OF POOR QUALITY

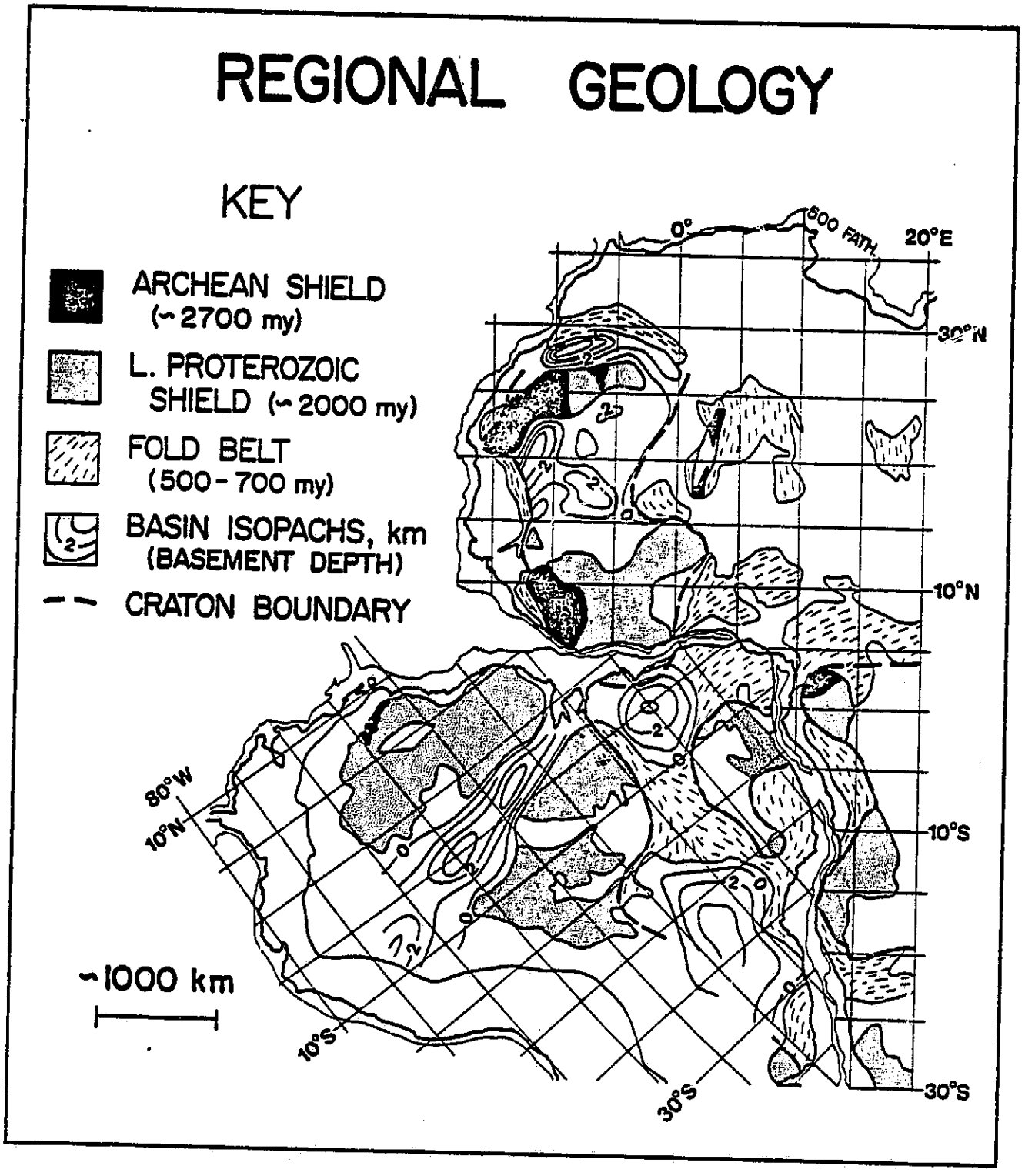

FIG. 2

ORIGINAL PAGE IS
OE POOR QUALITY

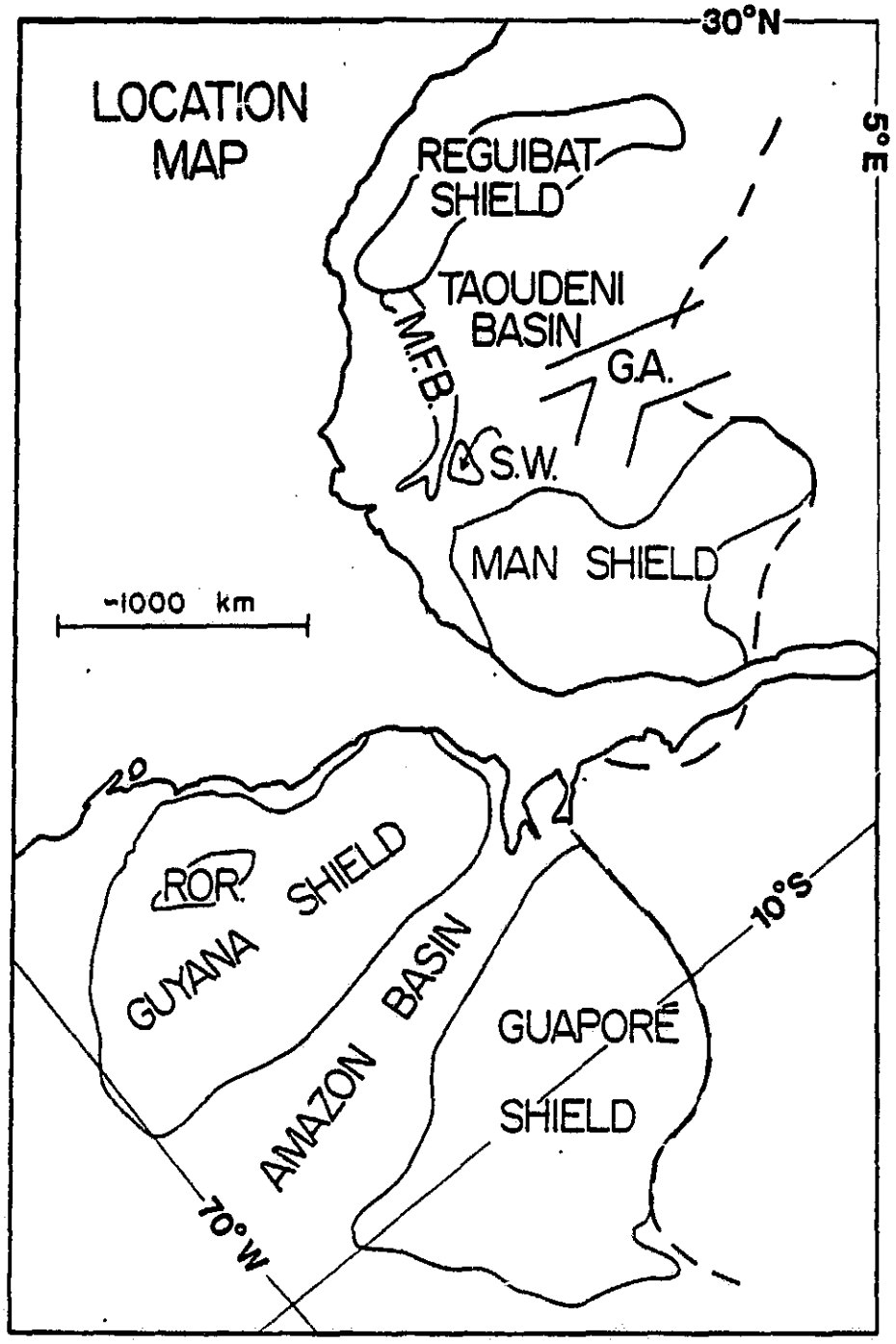
LOCATION MAP
30°N
5°E
REGUIBAT SHIELD
TAOUDENI BASIN
M.F.B.
G.A.
S.W.
MAN SHIELD
~1000 km
20
ROR
GUYANA SHIELD
AMAZON BASIN
GUAPORÉ SHIELD
10°S
70°W

FIG. 3

TECTONO-METALLOGENIC MAP

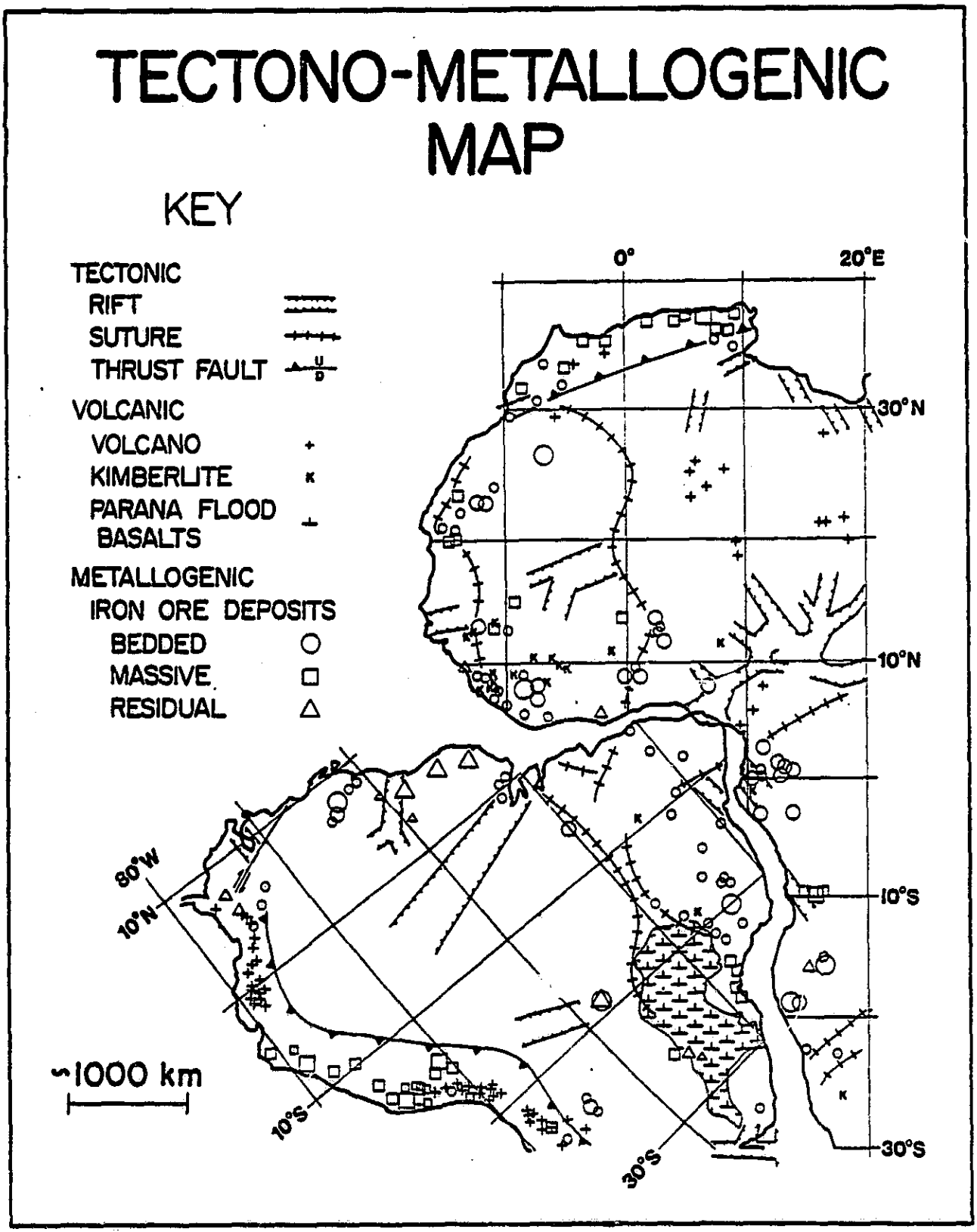

FIG. 4

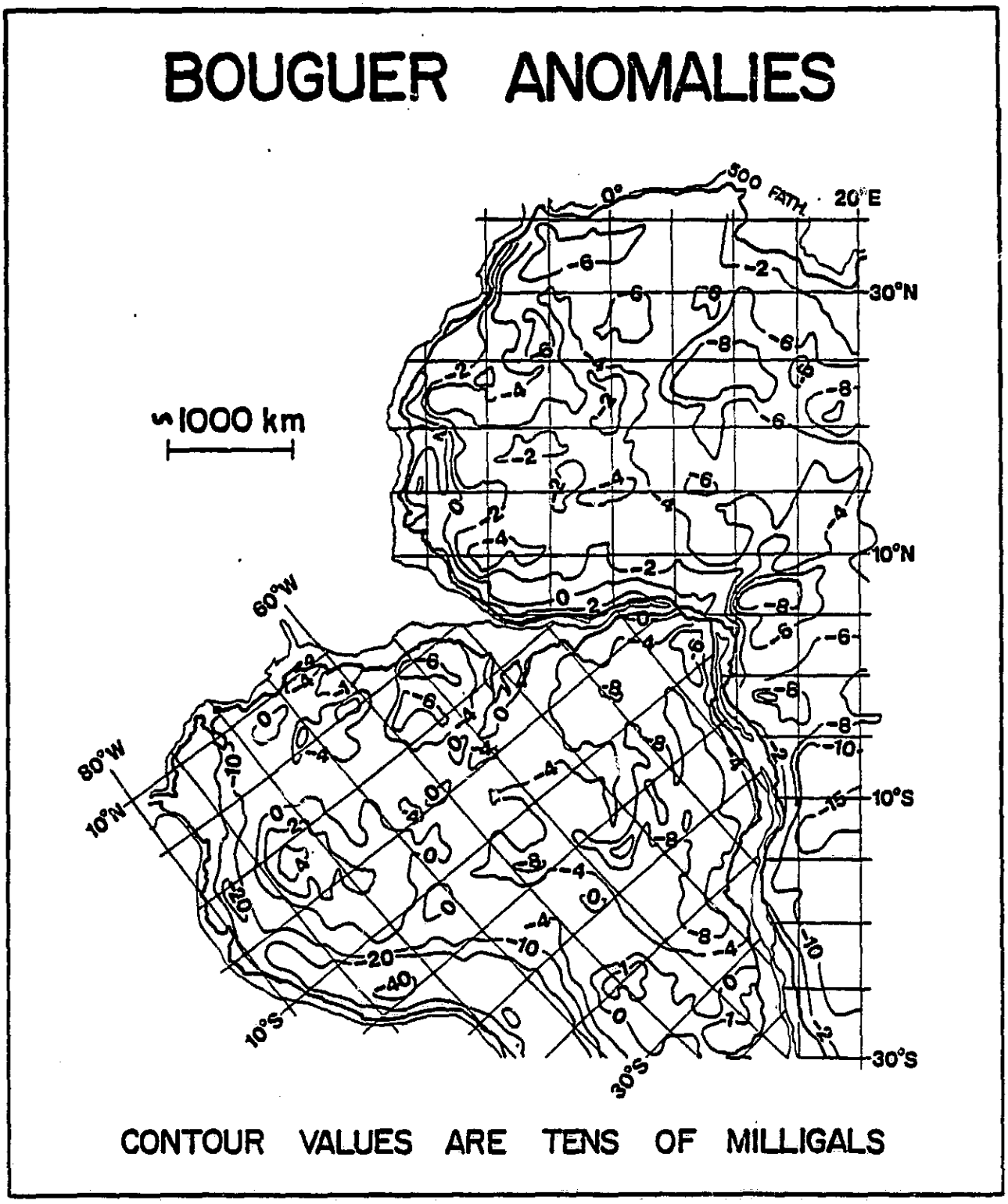
BOUGUER ANOMALIES
500 FATH.
20°E
30°N
10°N
10°S
30°S
60°W
80°W
1000 km
CONTOUR VALUES ARE TENS OF MILLIGALS

FIG. 5

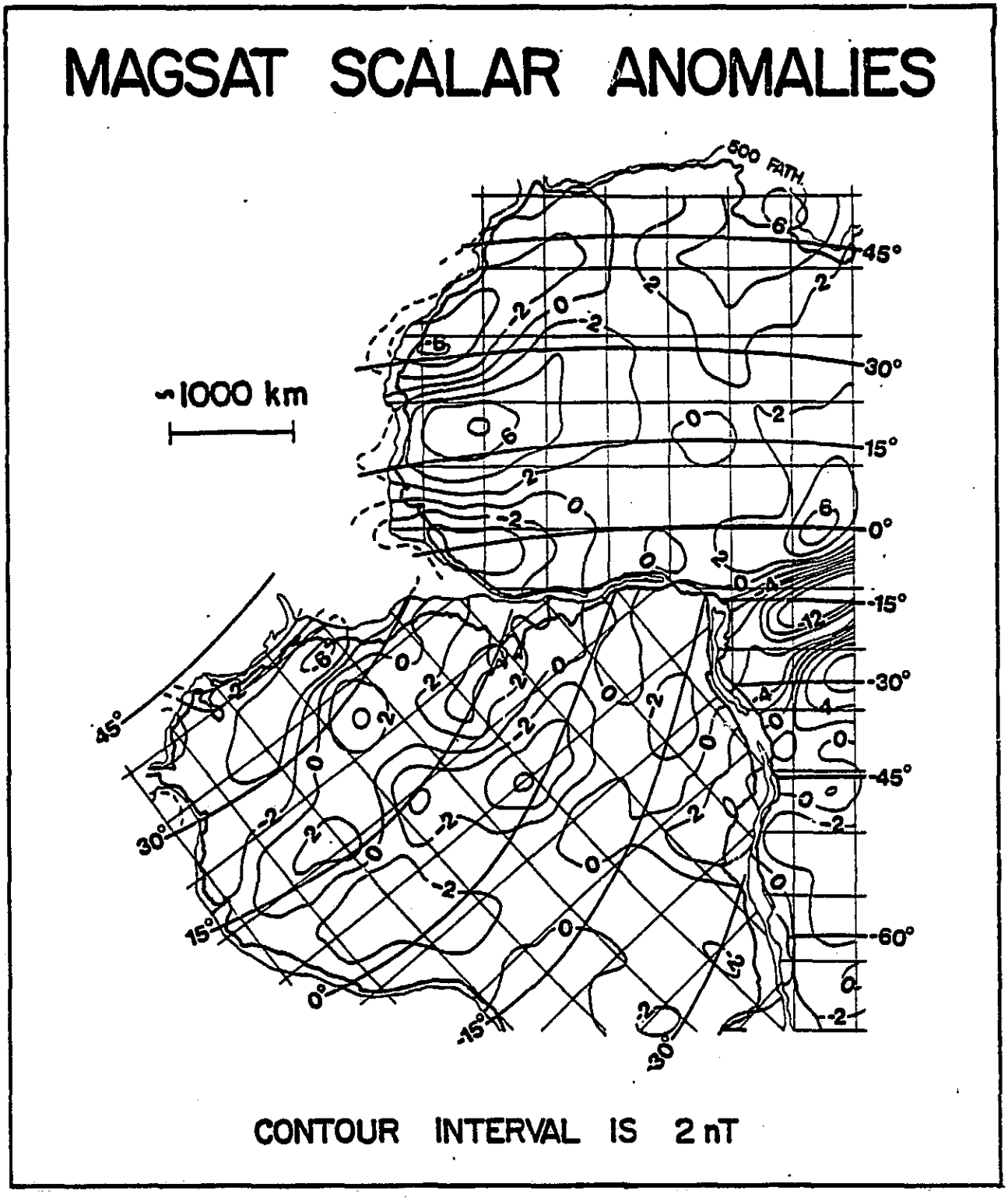

FIG. 6

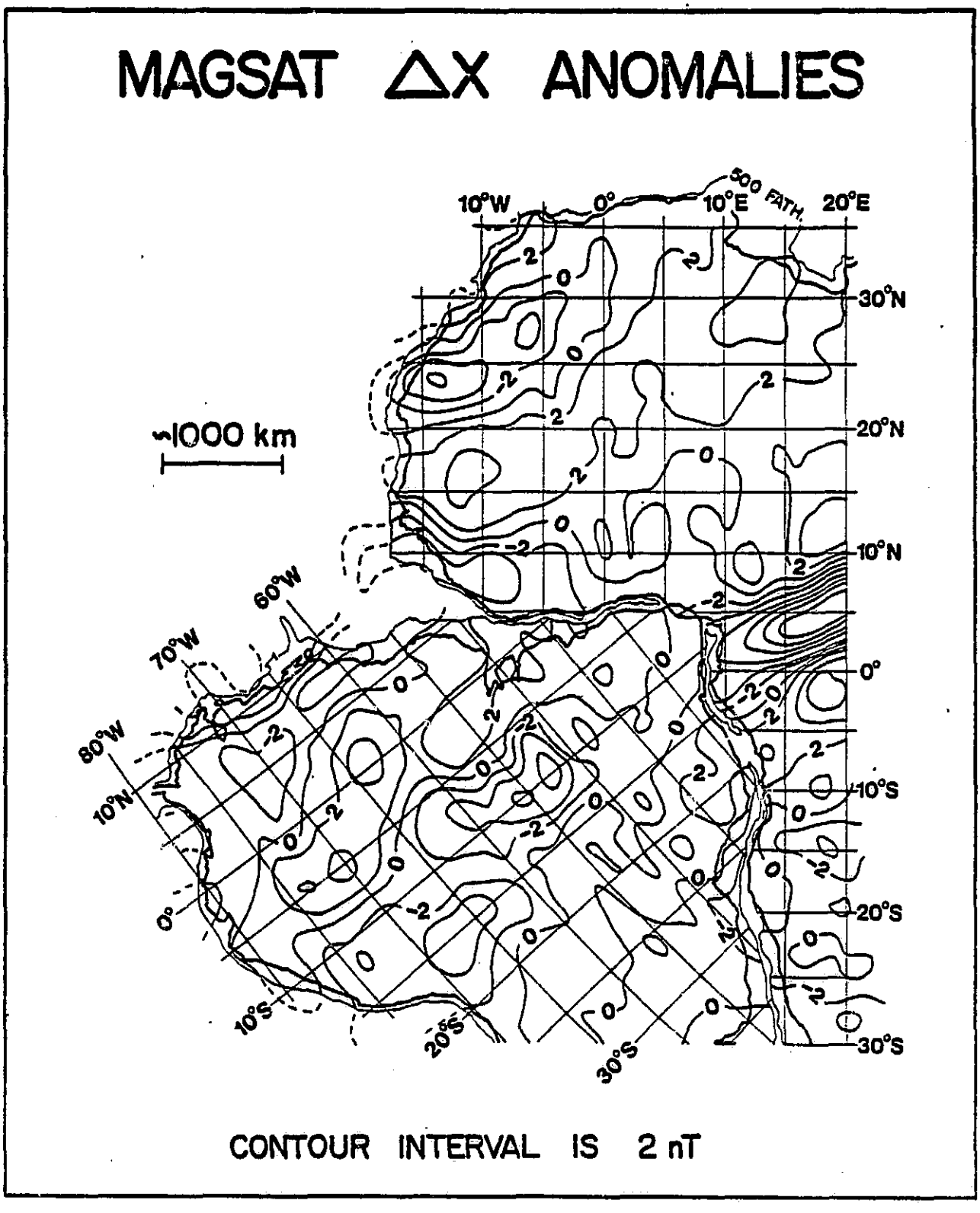
MAGSAT ΔX ANOMALIES
10°W
0°
10°E
20°E
500 KM PATH
30°N
20°N
10°N
0°
10°S
20°S
30°S
60°W
70°W
80°W
10°N
0°
10°S
20°S
30°S
~1000 km
CONTOUR INTERVAL IS 2 nT

FIG. 7

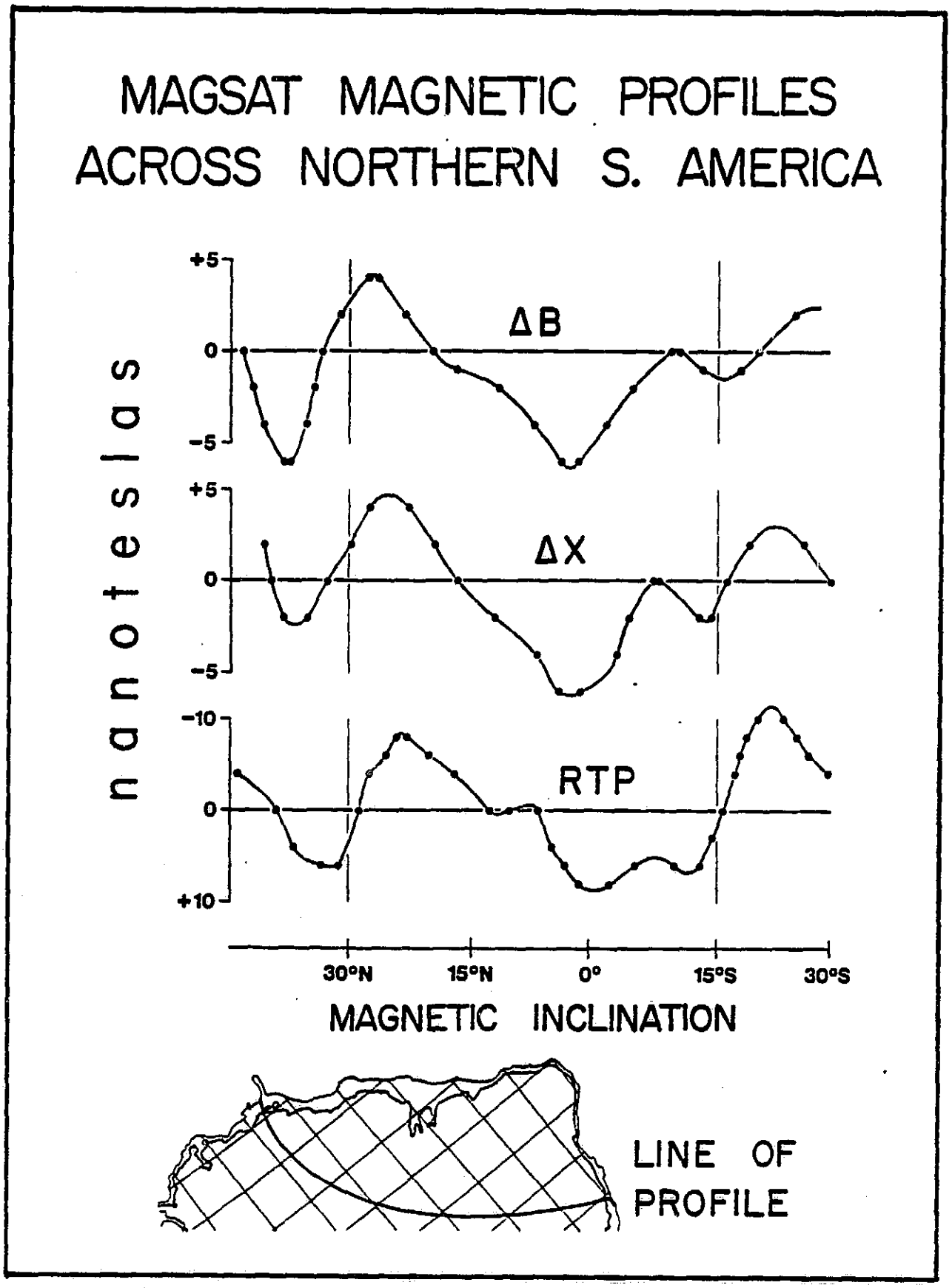
MAGSAT MAGNETIC PROFILES
ACROSS NORTHERN S. AMERICA
nanoteslas
+5
0
-5
ΔB
+5
0
-5
ΔX
-10
0
+10
RTP
30°N
15°N
0°
15°S
30°S
MAGNETIC INCLINATION
LINE OF
PROFILE

FIG. 8

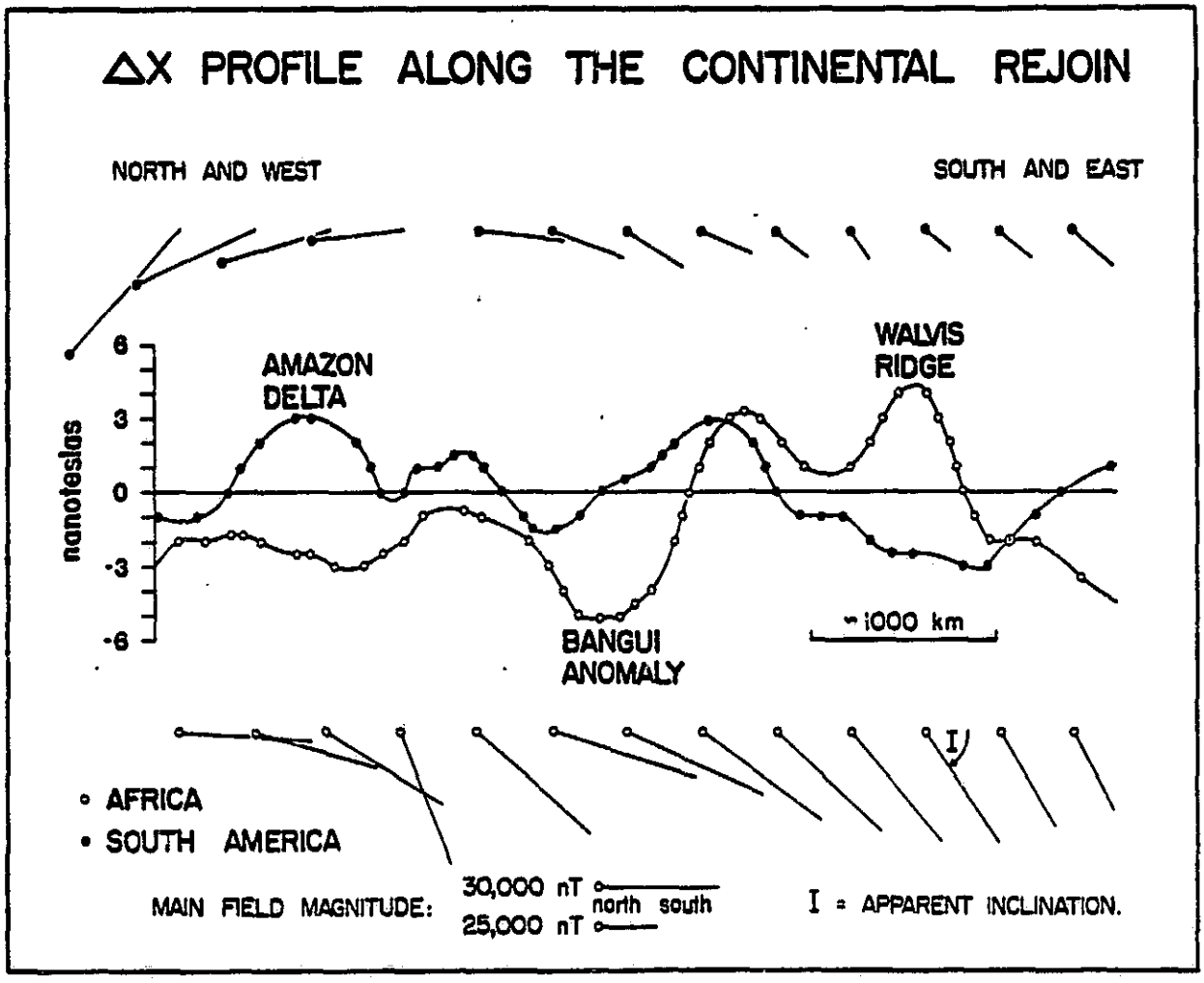
ΔX PROFILE ALONG THE CONTINENTAL REJOIN
NORTH AND WEST
SOUTH AND EAST
6
3
0
-3
-6
nanoteslas
AMAZON DELTA
WALVIS RIDGE
BANGUI ANOMALY
≈ 1000 km
I
AFRICA
SOUTH AMERICA
MAIN FIELD MAGNITUDE:
30,000 nT
25,000 nT
north south
I = APPARENT INCLINATION.

FIG. 9

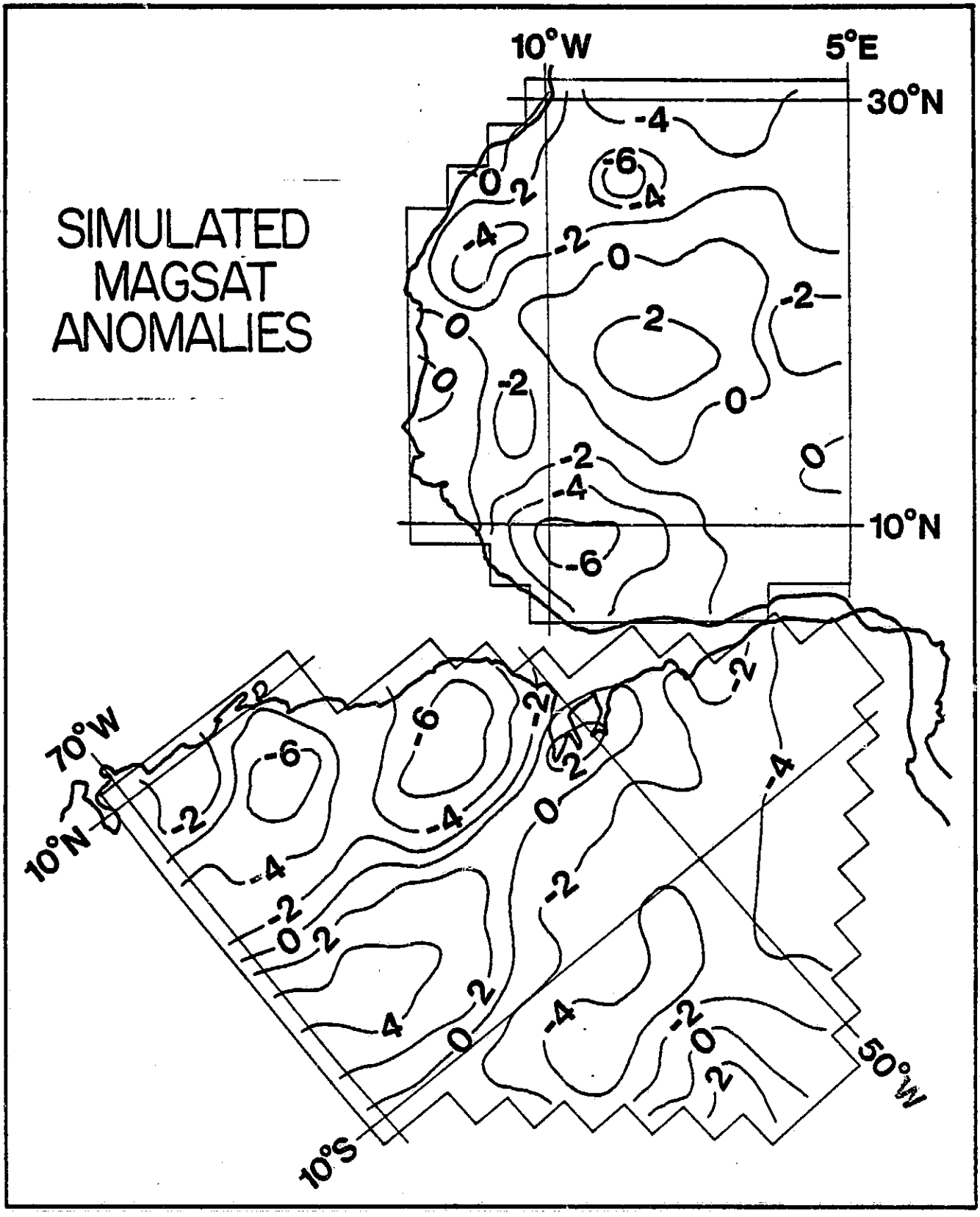

FIG. 10

TABLE 1

GEOLOGICAL INPUT	
Bedded iron formation,	
in Archean shield	-3
Archean shield	-2
Proterozoic shield	-1
Continental shelf	-0.5
Fold belt	0
Sedimentary basin	+1
Rift or aulacogen,	
in basin	+2
Rift or aulacogen,	
in other setting	add +4

BOUGUER INPUT	
≤ -60 mgal	-3
-60 to -40	-2
-40 to -20	-1
-20 to 0	0
0 to + 20	+1
≥ +20	+2

FREE AIR INPUT	
≤ +8 mgal	-3
+8 to +2	-2
+2 to -4	-1
-4 to -10	0
-10 to -16	+1
≥ -16	+2

APPENDIX 4

NATIVE IRON IN THE CONTINENTAL LOWER CRUST: PETROLOGICAL AND GEOPHYSICAL IMPLICATIONS

Abstract. Lower crustal granulite xenoliths recovered from a kimberlite pipe in west Africa contain native iron (Fe^{o}) as a decomposition product of both garnet and ilmenite. Magnetic measurements show that less than 0.1 volume per cent of iron metal is present. Geothermometry and oxygen geobarometry indicates that the oxide and metal phases equilibrated between iron-wüstite and magnetite-wüstite buffers which may represent the oxidation state of the continental lower crust, and the depleted lithospheric upper mantle. Ferromagnetic Fe^{o} could be stable to a depth of ≈95 km, and should be considered in the interpretation of long wavelength static magnetic anomalies.

Knowledge of the mineralogy of the deep continental crust is extremely limited (1), and the redox state of the lower crust has never been fully addressed. Although the Earth's core is probably dominated by metallic iron, surface terrestrial conditions are generally oxidized and naturally occurring iron metal, native iron, is rarely formed except in coal beds, low temperature (<500°C) serpentinites, lavas which have or may have incorporated carbonaceous sediments (2) and, at one locality, in a quartz garnet glaucophane lawsonite assemblage (3).

We report the recognition of native iron in lower crustal granulites from the Man Shield in Liberia, west Africa. The rocks (2-25 cm diameter) were recovered from a diamond-bearing kimberlite pipe (10°41'W 7°33'N) that erupted in the Mid-Cretaceous, 90-120 my ago, following the breakup of Gondwanaland (4). Granulites and other xenoliths were incorporated from the volcanic conduit walls into the kimberlite on its upward passage from the mantle. Although high temperatures were attained, rapid adiabatic cooling has prevented thermal metamorphism of the xenoliths or chemical interaction with the kimberlite.

The granulites, composed of 1-5 mm size garnet, clinopyroxene and plagioclase with accessory ilmenite and rutile, are similar to granulites described from

elsewhere in Africa (5) and other parts of the world (6). Garnet-pyroxene geothermometry (7) yields equilibration temperatures of 700-780°C assuming a 10 kb lower crustal pressure, commensurate with temperatures and pressures of granulite facies metamorphism. Partial melting in some granulites has produced second generation pyroxene with kyanite and scapolite, and these rocks record temperatures well above 800°C. Rutile is overgrown by Fe^{2+}-freudenbergite ($Na_2FeTi_7O_{16}$) which is sodium-metasomatic in origin (8) from reaction with a fluid phase also enriched in Ca, S and CO_2 (and possibly CO and CH_4) that crystallized interstitial scapolite (9) and pervasive sulfides (troilite, pentlandite, chalcopyrite); rare graphite formed along cracks and mineral grain boundaries.

Garnets are Fe^{2+}-rich with 51-56 mole % almandine ($Fe_3Al_2Si_3O_{12}$), 27-32 % pyrope ($Mg_3Al_2Si_3O_{12}$) and 14-17 % grossular ($Ca_3Al_2Si_3O_{12}$). Incipient to advanced decomposition has produced iron metal particles (<2 μm to ≈10 μm), partially or completely enveloped in magnetite. Metal-oxide assemblages are concentrated along crystal edges and in irregular fracture patterns throughout garnets (Fig. 1a). Metal compositions, determined by electron microbeam analyses, show 98-99 wt % Fe, with minor Ni (≈0.15 wt %), Co (≈0.35 wt %), Cu (≈0.30 wt %), and Zn (≈0.2 wt %). The matrix to native iron is a spongy, fine grained, white and translucent phase identified in some cases as scapolite, but in other samples it remains unidentified. A highly aluminous (18-21 wt % Al_2O_3) tschermakitic amphibole, of assumed high pressure origin (10), is also present. Experiments (11) indicate that almandine garnet is unstable at oxygen fugacities (fO_2's) above the FMQ (fayalite = magnetite + quartz) buffer at 2 kb and at temperatures above approximately 850°C. Higher pressures increase the thermal stability, however there are no experimental data on garnets of the present compositions.

Native iron also resulted from the decomposition of ilmenite (Fig. 1b). The assemblage is ilmenite ($FeTi_2O_5$) + ulvöspinel (Fe_2TiO_4) ± iron (Fe^0), with

troilite (FeS) an accessory phase. The iron has similar grain sizes to, but lower Ni, Co, Cu and Zn (total of <0.5 wt %) than, particles in garnet. Very low values of ferric iron in both the ulvöspinels (0.2-0.3 wt % Fe_2O_3) and ilmenites (0.1-2.4 wt %) are consistent with experimental data (12) for Fe-Ti oxides in equilibrium with metallic iron, suggesting that ilmenite decomposition took place at ≈1000°C at low fO_2 (<IW, iron-wüstite) and that the ulvöspinel may be cation-deficient and Ti-rich. Applying the solution parameter model for metal-free coexisting Fe-Ti oxides (13) temperatures of 996° to 830°C at fO_2's between $10^{-12.2}$ to $10^{-16.2}$ atms are obtained. These data lie just above the MW (magnetite-wüstite) buffer at 1 bar and lie between MW and IW if the buffers are corrected to 10 kb total pressure.

From iron metal textural relations in garnet and in ilmenite, and based on the differences in temperature obtained from garnet-clinoxpyroxene and ilmenite-ulvospinel mineral thermometers, we suggest that native iron formed in the solid state at higher temperatures than those implied from Fe-Mg and Ca exchange in the silicates. If pressures greater than the assumed 10 kb pertained, then higher temperatures would result from the calculation. We conclude that decomposition was initiated below IW and equilibrated to IW-MW. Native iron was formed at high temperatures (≈800-1000°C) and decomposition was induced at high pressures (≈10 kb), based on the assemblage scapolite, tschermakitic amphibole and Fe^{2+}-freudenbergite.

With respect to broad scale geophysical surveys of the Earth's crust, selected physical properties of the larger specimens of granulites are in Table 1. Apparent specific gravities range from 2.75 to 3.25 but are mostly between 2.95 and 3.25. Equating specific gravity to density, by Birch's relationship for granulites (14) as modified by temperature (15) compressional seismic wave velocities (V_p) of 6.3 to 7.2 km. sec^{-1} are estimated

Curie balance thermomagnetic analyses of several specimens confirmed the presence of iron metal and magnetite. Each analysis (≈10 mg chips from samples

3, 4, 9, 25) showed reversible magnetic transitions at 580° and 770°C (±25°C), the Curie temperatures of pure magnetite and pure iron, respectively.

Magnetic susceptibility (X_v) of the granulites at room temperature and pressure is 0.5-3 x 10^{-3} (S.I.), natural remanent magnetization (NRM) intensities range from about 10^{-3} to 10 $A.m^{-1}$, and the Königsberger ratio is usually >1 (Table 1). Figure 2 suggests a proportional relationship between the restricted values of susceptibility and the wide range of NRM intensity.

Long wavelength (50-500 km) aeromagnetic and POGO and MAGSAT satellite-derived magnetic anomalies frequently appear to require lower crustal magnetic sources with magnetization intensity contrasts in excess of 1 $A.m^{-1}$ (17), a range of induced magnetization rarely attained on a large areal scale by dominant crustal materials exposed at the Earth's surface (18). Magnetite-bearing granulites are considered as the most probable source rocks (19), particularly if thermally-promoted viscous magnetic remanence (20) or the Hopkinson effect of thermally-enhanced (≈x2) susceptibility (21) of magnetite are considered, but metal alloys in the upper mantle have also been suggested as possible mineral magnetic sources (22).

Native iron observed in the Liberian lower crustal granulites (Fig. 1) is in the multidomain (MD) size range (23), allowing an estimate, based on magnetic susceptibility (24), of <0.1 vol % Fe^{o}, assuming that only MD Fe^{o} contributes to susceptibility. Even with this same assumption, in accounting for the very large Hopkinson effect observed with pure iron (25) the granulites' average induced magnetization cannot be enhanced to 1 $A.m^{-1}$ or greater until depths equivalent to temperatures of 580° to 620°C. Contrasts in total magnetization intensity between granulites, however, range from 0.01 to 10 $A.m^{-1}$ at 25°C, and the highest intensities are due largely to NRM (Table 1).

Pure MD iron does not maintain a directionally stable magnetic remanence because the coercive force is ≈80 $A.m^{-1}$, close to the magnitude of the Earth's main field. Furthermore, the critical temperature of stable remanence

(blocking temperature) in heating is usually a spectrum extending below the Curie point in MD materials. Also, magnetic minerals can acquire a viscous remanent magnetization (VRM) parallel to an external field, particularly if exposed for long periods of time, even at temperatures below the blocking temperature. Thus, MD Fe^{o} remanent magnetization in the lower continental crust could be largely aligned with the Earth's field, and would then be indistinguishable from induced magnetization as far as high altitude magnetic surveys are concerned.

We conclude that these native iron-bearing granulites are examples of the types of rocks which may be responsible for a significant part of the magnetization measured by POGO and MAGSAT satellite magnetometers, and that the lower continental crust may be characterized by oxidation states equivalent to IW-MW. Unless there is an intermediate relatively oxidized horizon, these oxidation states probably persist into the upper mantle and down through the depleted lithosphere (26), suggesting that native iron may also exist below the Moho. If so, then temperature and the αFe-γFe phase boundary rather than the α-$\alpha'Fe$ Curie transition are the significant controls on the lower depth limit for iron ferromagnetism in the lithosphere. The α-γ boundary (27) intersects the typical continental shield geothermal gradient at 75 to 80 km, but the deepest limit may be defined by the very low gradient Sierra Nevada geotherm which intersects the α-γFe phase boundary at 90 to 95 km.

The granulites described here contain metallic iron, which, along with the sulfides and graphite but mitigated by grain contact and temperature, could contribute to the supposed lower crustal or upper mantle high electrical conductivities previously explained (28) as due to hydrous minerals or partial melting. The mafic granulite character, specific gravities, and the T, P and V_p estimates for the granulites correspond to model parameters (29) of the lower continental crust, but the extent to which native iron is present requires to

be established as does the precise mechanism that induced decomposition of iron-rich almandine garnet and ilmenite. Decomposition is not due to the kimberlite event because these gas-charged CO_2-rich eruptives are moderately oxidizing, and because mantle metasomatism is typically potassic (30), whereas the native iron-bearing granulite xenoliths are highly reduced and are sodium-enriched.

References and Notes

1. R. W. Kay and S. M. Kay, Rev. Geophys. Space Phys. 19, 271 (1981); R. A. Kerr, Science 225, 492 (1984); ibid., 224, 1418 (1984).
2. E. R. Deutsch, K. V. Rao, R. Laurent, M. K. Seguin, Nature (London) 269, 684 (1977); A. K. Pedersen, Contrib. Mineral. Petrol. 69, 397 (1979); P. Ramdohr, in The Ore Minerals and Their Intergrowths, vol. 1 (Pergamon, New York, ed. 2, 1980), pp. 353-356.
3. F. M. Quodling, J. and Proc., Roy. Soc. New South Wales 97, 81 (1964).
4. S. E. Haggerty, J. Geophys. Res. 87, 10,811 (1982).
5. N. W. Rogers, Nature (London) 270, 681 (1977).
6. H. R. Rollinson, Lithos 14, 225 (1981).
7. D. J. Ellis and D. H. Green, Contrib. Mineral. Petrol. 71, 13 (1979).
8. Freudenbergite is $Na_2Fe_2Ti_6O_{16}$ (G. Frenzel, Neues Jahr. Mineral Mh. 1, 12 (1961)). The ferrous iron analog is reported by S. E. Haggerty, ibid. 8, 375 (1983) in Liberian granulites, and by S. E. Haggerty and J. J. Gurney, EOS: Trans. Am. Geophys. Union 65, 305 (1984) in high pressure zircon-bearing nodules from kimberlites in South Africa.
9. Compositions are similar to scapolites described A. P. Jones et al., J. Geol. 91, 143 (1983). From their conclusions and experimental data (J. R. Goldsmith, Geol. Soc. Am. Bull. 87, 161 (1976)) the Liberian granulites' scapolites probably are stable only at relatively high pressures (12-20 kb) at about 1000°C.
10. T. W. Bloxam and J. B. Allen, Trans. Roy. Soc. Edinburgh 64, 1 (1960); B. E. Leake, Mineral. Mag. 38, 389 (1971); B. L. Doolan, E. Zen, A. E. Bence, Am. Mineral. 63, 1088 (1978).
11. L. C. Hsu, J. Petrol. 9, 40 (1968); I. Keesman, S. Matthes, W. Schreyer, F. Seifert, Contrib. Mineral. Petrol. 31, 132, (1971).
12. B. Simons and E. Woermann, Contrib. Mineral. Petrol. 66, 81 (1978).
13. K. L. Spencer and D. H. Lindsley, Am. Mineral. 66, 1189 (1981).

14. M. H. Manghnani, R. Ramananantoandro, S. P. Clark, Jr., J. Geophys. Res. 79, 5427 (1974).

15. N. I. Christensen, J. Geophys. Res. 84, 6849 (1979).

16. Analyses at ≈5°C.min^{-1} in 1-100 mT under Ar atmosphere were temperature-calibrated after S. D. Norem et al., Thermochim. Acta 1, 29 (1970), utilizing the Curie point definition of M. Prévot et al., J. Geophys. Res. 88, 2316 (1983).

17. P. Wasilewski and M. A. Mayhew, Geophys. Res. Lett. 9, 325 (1982).

18. R. S. Carmichael, in CRC Handbook of Physical Properties of Rocks, vol. II, R. S. Carmichael, Ed. (CRC Press, Boca Raton, Fla., 1982), chap. 2.

19. Ref. 17; P. Wasilewski, H. H. Thomas, M. A. Mayhew, ibid. 6, 541 (1979); P. Wasilewski and D. M. Fountain, ibid. 9, 333 (1982).

20. G. Pullaiah, E. Irving, K. L. Buchan, D. J. Dunlop, Earth Planet. Sci. Lett. 28, 133 (1975).

21. D. J. Dunlop, J. Geophys, 40, 439 (1974).

22. S. E. Haggerty, Can. J. Earth Sci. 16, 1281 (1979).

23. R. F. Butler and S. K. Bannerjee, J. Geophys. Res. 80, 252 (1975).

24. L. J. Srnka and M. H. Mendenhall, J. Geophys. Res. 84, 4667 (1979); Ref. 18.

25. R. M. Bozorth, in Ferromagnetism (Van Nostrand, New York, 1951), p. 714.

26. S. E. Haggerty and L. A. Tompkins, Nature (London) 303, 295 (1983).

27. P. W. Mirwald and G. C. Kennedy, J. Geophys. Res. 84, 656 (1979).

28. T. J. Shankland and M. E. Ander, J. Geophys. Res. 88, 9475 (1983).

29. D. M. Fountain and M. H. Salisbury, Earth Planet. Sci. Lett. 56, 263 (1981); A. G. Jones, J. Geophys. 49, 226 (1981).

30. A. J. Erlank, H. L. Allsopp, C. J. Hawkesworth, M. A. Menzies, Terra Cognita 2, 261 (1982).

31. Field work was supported by the Weasua Mining and Development Corporation. Invaluable logistical support was provided by the Ministry of Lands, Mines an and Energy, Liberia, and the US and UK Embassies. NSF grant EAR83-08297 and NASA contract NAS5-26414 supported the analytical study.

Table 1. Magnetic properties and specific gravities of lower crustal granulites.

Sample # (a)	SG (b)	X_v (c) (S.I. $\times 10^{-4}$)	NRM (d) ($A.m^{-1}$)	J (e) ($A.m^{-1} \times 10^{-2}$)	Q (f)	M (g) ($A.m^{-1}$)
1	3.12	26	0.21	6.5	3.2	0.28
3	2.75	7.4	0.0062	1.8	0.34	0.024
4	3.21	13 (±3)	1.6	3.2	50	1.6
7	3.02	8.2	0.009 (±0.001)	2.0	0.45	0.029
8	3.01	8.6	0.19	2.1	9.0	0.21
9	3.18	18 (±2)	9.1 (±0.5)	4.5	200	9.1
12	3.06	15	0.96	3.7	26	1.0
13	2.87	5.3 (±1)	0.073 (±0.004)	1.3	5.6	0.086
14	2.97	8.4	0.14	2.1	6.7	0.16
17	3.25	11	0.085	2.7	3.1	0.11
26	3.08	5.7	0.0043	1.4	0.31	0.018

(a) Series SC-C; 2.54 x 2.54 cm cylindrical cores; measured at room temperature and pressure. (b) SG = apparent specific gravity. (c) X_v = apparent magnetic susceptibility per unit volume; error is $\pm 5 \times 10^{-5}$ except where noted. (d) NRM = natural remanent magnetization; error is ±2 in L.S.D. except where noted. (e) J = induced magnetization, calculated as $J = X_v.H_{ext}$, where H_{ext} for Liberia = 24.9 $A.m^{-1}$. (f) Q = Königsberger ratio = $NRM.J^{-1}$. (g) M = total magnetization = NRM + J.

Figure Captions

Fig. 1. Reflected light photomicrographs of native iron-bearing assemblages using a x20 oil-immersion objective: (a) shows garnet decomposition along cracks to metallic iron (bright, white spheres) in association with scapolite + tschermakitic amphibole; (b) is an ilmenite grain, set in clinopyroxene, that has undergone subsolidus reduction to lamellar ulvöspinel (dark gray laths) + iron metal (bright, white), with the black laths being plucked areas from sample preparation.

Fig. 2. Relation of natural remanent magnetization (NRM) to apparent magnetic susceptibility per unit volume (X_v) for lower crustal granulites (from Table 1).

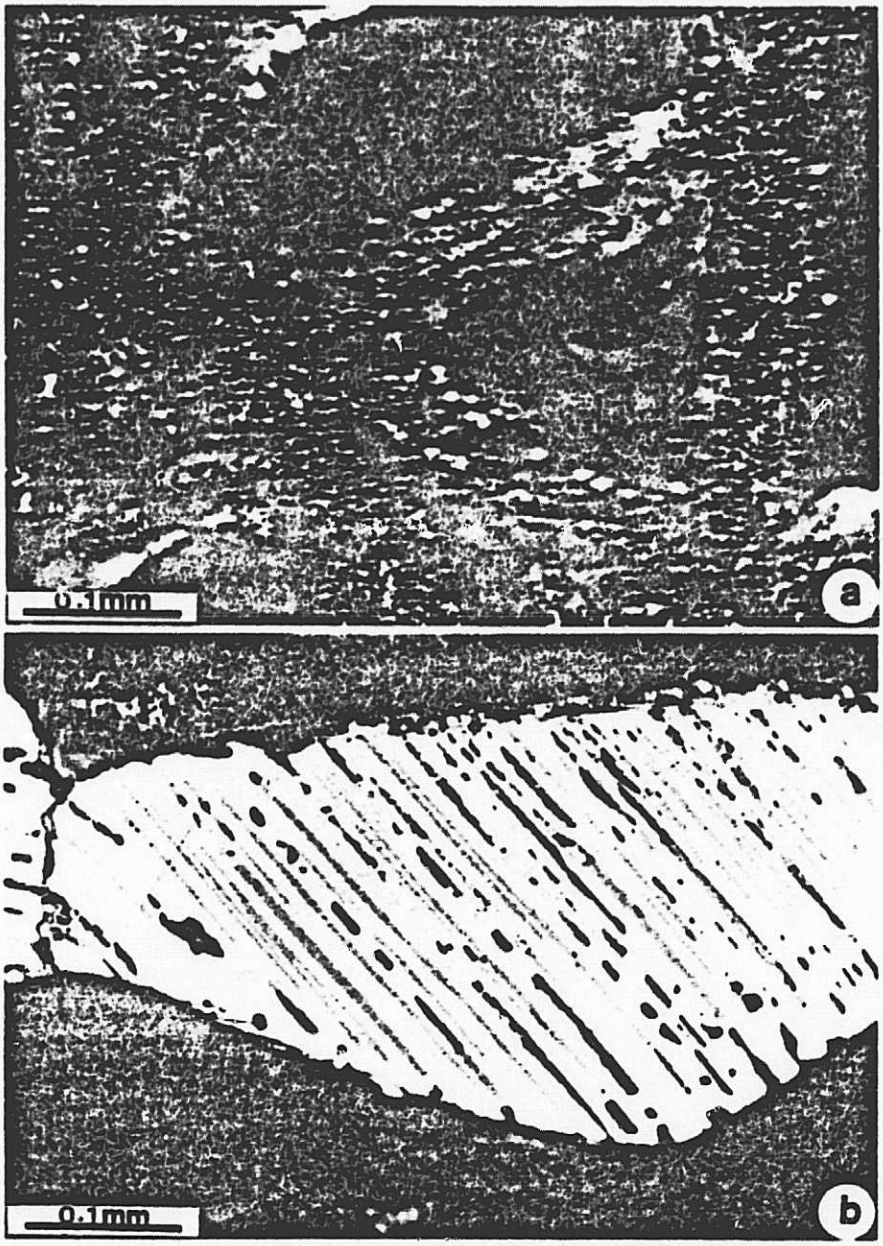

Fig. 1

ORIGINAL PAGE
BLACK AND WHITE PHOTOGRAPH

OF POOR QUALITY

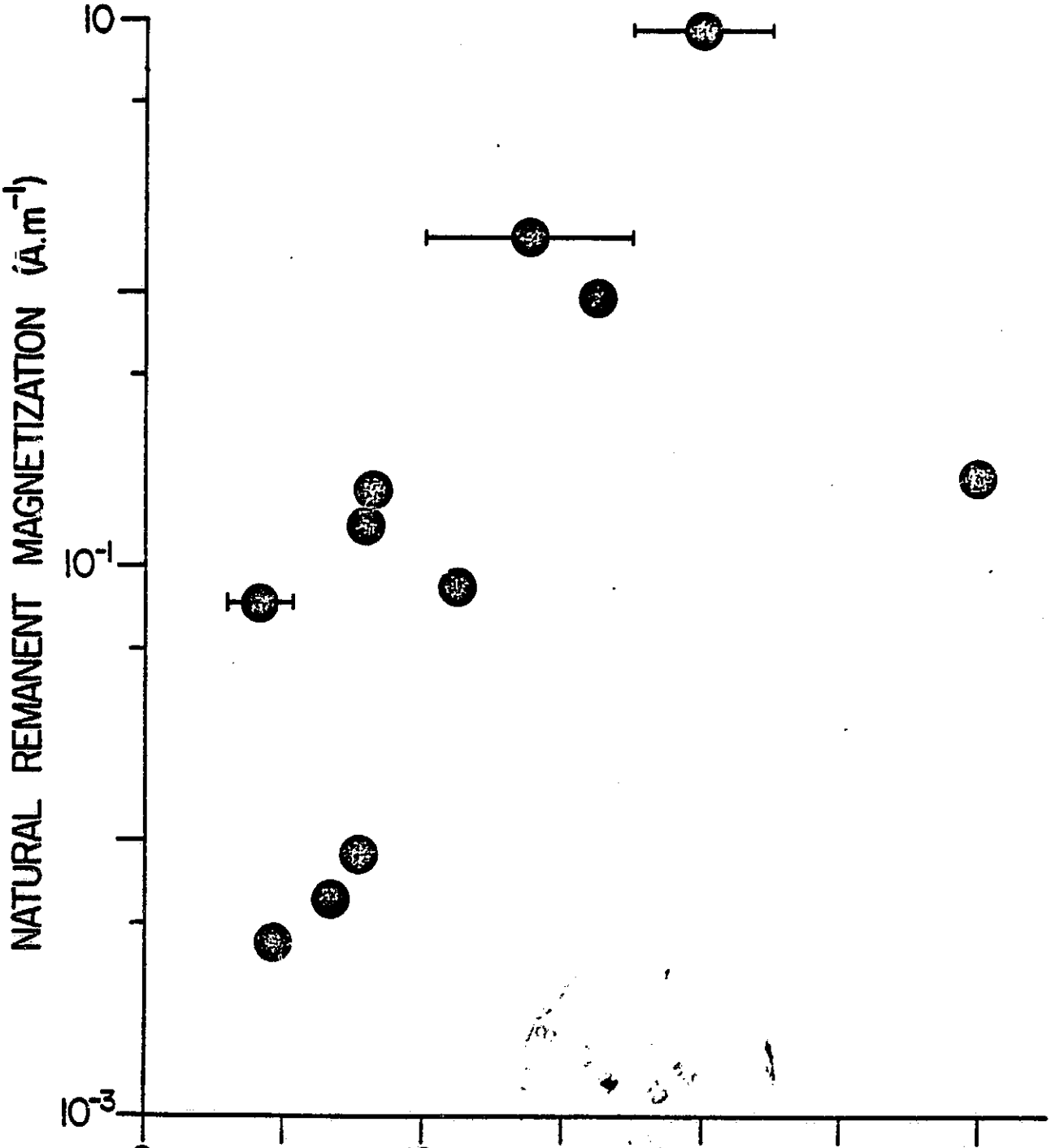

Fig. 2